2005

# Development of a porous silicon flow-through field effect sensing system for chemical and biological detection

Jeffrey Clarkson

## Recommended Citation

Clarkson, Jeffrey, "Development of a porous silicon flow-through field effect sensing system for chemical and biological detection" (2005). Thesis. Rochester Institute of Technology. Accessed from

# Development of a Porous Silicon Flow-Through Field Effect Sensing System for Chemical and Biological Detection

A thesis submitted in
partial fulfillment of the requirements for the degree of
Masters of Science in
Microelectronic Engineering

By

Jeffrey P. Clarkson
Microelectronic Engineering Department
Kate Gleason College of Engineering

Supervised by

Dr. Karl D. Hirschman
Microelectronic Engineering Department
Kate Gleason College of Engineering

Rochester Institute of Technology
Rochester, NY

August 12th, 2005

DEPARTMENT OF MICROELECTRONIC ENGINEERING
KATE GLEASON COLLEGE OF ENGINEERING
ROCHESTER INSTITUTE OF TECHNOLOGY
ROCHESTER, NEW YORK

---

## CERTIFICATE OF APPROVAL
## MASTER OF SCIENCE DEGREE THESIS

---

A thesis entitled

# Development of a Porous Silicon Flow-Through Field Effect Sensing System for Chemical and Biological Detection

by

Jeffrey P. Clarkson

The Masters of Science Degree Thesis of Jeffrey P. Clarkson
has been examined and approved by the thesis committee
as satisfactory for the thesis requirement of a
Master of Science degree.

We the undersigned have had the opportunity to attend, question, and discuss the candidate's presentation of research results upon which this thesis is based. We believe this work constitutes satisfactory completion of the requirements for a Master of Science degree.

Dr. Karl Hirschman ________________________ Date:______________
(Thesis Advisor)

Dr. James Moon ________________________ Date:______________
(Committee Member)

Dr. Alan Raisanen ________________________ Date:______________
(Committee Member)

# Development of a Porous Silicon Flow-Through Field Effect Sensing System for Chemical and Biological Detection

by

Jeffrey P. Clarkson

Jeffrey P. Clarkson ________________________ Date:______________
(Author)

# Curriculum Vitae

Jeffrey P. Clarkson was born in Middletown, NY on January 4th, 1980. He attended the Rochester Institute of Technology in Rochester, NY in 1998 and graduated with a Bachelor of Science degree in Microelectronic Engineering in 2003. Deciding to continue his studies at the Rochester Institute of Technology as a Masters of Science candidate, he pursued research in porous silicon based sensing for chemical and biological detection under the direction of Dr. Karl D. Hirschman and received a Masters of Science degree in Microelectronic Engineering in 2005.

# Acknowledgements

The author would like to acknowledge the Department of Microelectronic Engineering at the Rochester Institute of Technology for the opportunity to explore the world of semiconductors.

To Dr. Karl D. Hirschman, a man whose actions speak stronger than his words, a special thank you for unconditional support and guidance throughout the course of this work.

To Dr. James Moon, perhaps the most brilliant lecturer at the Rochester Institute of Technology, thank you for teaching me the value of academics without politics.

To Dr. Alan Raisanen, thank you for finding truth in research experimentally.

A special thanks to Vimalan Rajalingam, Rickey Persaud, Tiffany Hoover, and fellow graduate students, for contributions in all forms towards this work.

Thank you Dr. Phillipe Fauchet, Marie Archer, Wei Sun, Huimin Ouyang, and Mikhail Haurylau for collaborative efforts dedicated to the material that continues to fascinate us all; porous silicon.

To Nate Wescott and Dave Hathaway, who made significant contributions to this work, thank you.

My family, to whom I am most grateful for, thank you for support, encouragement, and belief in all that I do.

This work was supported in part by the Infotonics Technology Center and the National Science Foundation.

# Abstract

With an increasing need for homeland security, and breakthrough advancements in sensing applications, the demand for highly sensitive, compact, biological and chemical sensing devices is evident. Macroporous silicon (MPS) is an ideal material for meeting these demands because it exhibits a large degree of internal surface area and is fully compatible with silicon technologies. Since the surface is sensitive to charged molecules, localized field effects from analytes interfaced with MPS will cause modulation of a space charge region in the semiconductor. In this work, a porous silicon based sensing system is designed, fabricated, and characterized. The unique properties of porous silicon and its promising qualities which facilitate the means for interfacing fluidic and electrical systems are investigated. A flow-though structure is used to deliver analytes to a MPS sensing membrane region and integrated electrodes contacting the MPS can be used to take electrical measurements. Fabricated sensors are enhanced by packaging them in a fluidic system which enables the future possibility of arrayed sensing platforms.

To date this sensing system has successfully performed many sensing tasks applicable to the fields of science and technology. Unique measured capacitive responses of sensor to liquid phase acetone, ethanol, isopropyl alcohol, methanol, and toluene demonstrate detection and discrimination capabilities. The sensor has proven to be useful in monitoring the quality of air by detecting solvent vapor phase concentrations of < 1 ppm. Packaged devices were used to monitor the quality of a water supply and were able to detect the presence of contaminants such as isopropyl alcohol. Application to the field of biology was demonstrated by observing a repeatable trend in measured capacitance during binding events between biotin and streptavidin proteins located in the MPS sensing membrane. The work presented herein shows that this sensing platform has a high degree of potential for repeatable and day-to-day reproducible detection in the areas of chemical and biological sensing.

# Table of Contents

# Table of Abbreviations

| Abbreviation | Stands for |
|---|---|
| AC | Alternating current |
| cDNA | Complementary deoxyribonucleic acid |
| CDs | Critical dimensions |
| ChemFET | Chemical field effect transistor |
| DC | Direct current |
| DI | Deionized |
| DMF | Dimethylformamide |
| DNA | Deoxyribonucleic acid |
| DRIE | Deep reactive ion etching |
| GEN-1 | First generation |
| GUI | Graphical user interface |
| HF | Hydrofluoric acid |
| IC | Integrated circuit |
| IEEE | Institute of Electrical and Electronic Engineers |
| IPA | Isopropyl alcohol |
| IUPAC | International Union of Pure Applied Chemistry |
| KOH | Potassium Hydroxide |
| LCR | Inductance capacitance resistance |
| LPCVD | Low pressure chemical vapor deposition |
| MEMS | Microelectromechanical system |
| MOSFET | Metal-oxide-semiconductor field effect transistor |
| MOS | Metal-oxide-semiconductor |
| MPS | Macroporous silicon |
| MRS | Materials Research Society |
| ncDNA | Noncomplementary deoxyribonucleic acid |
| pDNA | Probe deoxyribonucleic acid |

| | |
|---|---|
| PECVD | Plasma enhanced chemical vapor deposition |
| ppm | Part per million |
| PS | Porous silicon |
| RCA | Radio Corporation of America |
| RF | Radio frequency |
| SEM | Scanning electron microscope |
| SOC | System-on-chip |
| SPIE | International Society of Optical Engineering |
| TEOS | Tetraethylorthosilicate |

# List of Figures

# List of Tables

## Chapter 1

# Introduction

### 1.1 History and Motivation

Modern day society has given rise to an era of information technology where real-time information of remote events is highly desirable. In 1609, when an Earth-centered universe was scientifically accepted, Galileo used the telescope to discover moons orbiting Jupiter. This is one of the first documented forms of sensing applications ever used in human history [1]. The first semiconductor based sensors were developed during the 1950s at Bell Laboratories. When Phann, Thurston, and Smith derived the physics of piezoresistance in silicon and germanium it was thought that it could be used for sensing technologies. Phann stated "Now that we've studied the transduction effects in semiconductors for the purpose of getting rid of them, maybe they're useful." Then, in the early 1960s, Art Zias, who had gotten word of this from Phann, left Bell Laboratories to lead a research group at Honeywell to develop piezoresistive accelerometers and pressure sensors for the United States Air Force [2].

Today, a vast spectrum of semiconductor based sensing technologies exists. This is in large part due to the rise of microelectromechanical system (MEMS) technology, which has provided the means to design and fabricate devices that perform sensing tasks that were previously not possible. When combined with on-chip electronics for system on chip operation, very powerful sensing objectives can be met. The rate of development in sensing technology is great and this is exhibited at conferences held by the Institute of Electrical and Electronics Engineers (IEEE), the International Society for Optical Engineering (SPIE), and the Material Research Society (MRS) world-wide.

Today's sensors impact society in a positive way by monitoring water quality, enhancing medical practice and informing individuals of harmful environments. For these reasons, society has established a demand for increasingly advanced sensing capabilities.

The semiconductor industry has called upon integrated circuit (IC) and MEMS technologies to satisfy these demands and continue to provide smaller, better, and low-cost sensing devices.

## 1.2 Porous silicon in chemical and biological sensing

Traditionally, chemical field effect transistors (ChemFETs), a technology not based on porous silicon (PS), have been used for chemical and biological sensing applications. This type of device operates similarly to a metal oxide semiconductor field effect transistor (MOSFET) and is able to detect a sample under investigation through a work function difference which exists at the gate region. Primary limitations of this type of device are its dependence on an appropriate gate material, requirement of large gate areas, and complexities of integrating fluidic systems [3].

Porous silicon based sensing is an alternative way to perform chemical and biological detection. This newer form of technology involves modification of bulk silicon by means of electrochemical etching with an anodization process. Perhaps the most common form of PS based sensing is optically based which makes use of microporous silicon material. An analyte is placed in the PS region and measurements of optical properties such as effective index of refraction, effective optical path length, reflectance, and transmission are used for sample detection [4-7].

Macroporous silicon (MPS), the material used for the sensor in this work, is another form of PS which, through evidence of this thesis, proves to be a viable material for electrically based sensing of chemical and biological materials [8-10, 13]. MPS has an exceptionally large amount of surface area per unit volume and because of this, the use of this material is highly advantageous for field effect sensing. Compared to an equivalent ChemFET sensing region, MPS yields a greater amount of surface area and this can ultimately lead to more sensitive, smaller sensors which are conducive for integrating fluidic systems.

## 1.3 Goal of study

The goal of this study is to integrate electrical and fluidic systems for the design and fabrication of a system on chip (SOC) capable of performing chemical and biological sensing. A monolithic integration strategy makes use of MPS as a gateway to interface the electrical and fluidic domains. In doing this, the MPS material, acting as a sensing membrane, is used in a flow-through structure to transport a fluidic sample under investigation from fluidic channels on one side of the chip to sensing electrodes on the other. Once an analyte is present in the MPS sensing membrane, a fluid/oxide/semiconductor interface is present and a modulation of the space charge region in the silicon occurs [11-12]. It is the space charge modulation from localized field effects at the fluid semiconductor interface that is the fundamental sensing mechanism of this device.

The primary goal of this research is to develop a sensing platform which incorporates electrical and fluidic systems for chemical and biological detection. To meet this goal a series of objectives have been set:

1. Development of a MPS flow-through sensing membrane structure
2. Monolithic integration of fluidic and electronic systems
3. Assembly of sensing arrays
4. Detection of chemical or biological materials

A complete understanding of MPS is critical for the development of a MPS flow-through structure. To establish thorough comprehension of MPS, investigation into mechanisms of anodic pore formation, propagation, and porosity are paramount. Analysis of literature together with fabrication experience will be used to develop an awareness of design considerations specific to this work. It is hypothesized that a combination of MPS formation and KOH etching can achieve a flow-through structure. Experimental feasibility studies will be conducted to realize a fabrication scheme appropriate for this device. A stipulation of this work requires the sensing device to have a fluidic delivery system that has the capability of receiving a sample and delivering it into the sensing membrane region. It is therefore a necessary design consideration to allow integration of such fluidic systems into the device. The fabrication of devices designed with such an integration scheme will be based on robust and conventional processing technologies. Special consideration will be necessary for biological sensing applications where the device materials must demonstrate low cytotoxicity levels, and acceptable levels of *in vitro* biocompatibility.

A first generation device has already been developed and there is room for improvements [13]. One improvement could be a design that supports an array of preprogrammed sensors. A programmed sensor may have a specific material that dictates sample binding within the sensing area, or demonstrates a unique electrical response of its own. Preprogramming will be conducted through a fluidic system capable of introducing a precursor or probe material into MPS sensing membranes in an array.

Bonding of additional Si wafers or glass cover-slides will be considered for creating an addressing system capable of providing fluidic access to individual sensing membranes across an entire array. It is ideal to find a bonding scheme which is compatible to the overall fabrication scheme and analyte materials that will be passing through the device. For these reasons MicroChem SU-8 2100 epoxy based photoresist is investigated.

The final objective of this study is to conduct electrical testing and demonstrate device operation. In order to handle probe and analyte materials, a fluidic test fixture will be built. Capability of dispensing microliter size samples into the fluidic system of the device is desired. Measured device metrics include AC conductance, AC capacitance, sensitivity to various biological and chemical samples, specificity, hysteresis, and recognition of biological events.

## 1.4 Organization of thesis

The following chapters will explain the development of a MPS based sensor integrated with fluidics to perform sensing operations to identify chemicals, in the form of solvents, and biological events, such as protein binding. Chapter 2 will introduce MPS to the reader in overview and provide details on the relevance of this material to this work. Discussion of theory in Chapter 3 explains the sensing mechanism in detail. It provides a theoretical understanding of electrokinetic behavior at fluid-semiconductor interfaces and their subsequent localized electric fields which give rise to modulation of a space charge region. Following this, Chapter 4 explains device operation and application during chemical sensing of both liquid and vapor phase solvents, biological based sensing, and a polymer infiltration technique. Chapters 5 and 6 discuss realization of the MPS flow-thorough sensing membrane and integration of electrodes. Several experimental investigations/designs will be reviewed and remarks on what was learned will be presented with specific regard towards design and fabrication of the final sensing platform. Electrical characterization of the sensor will be discussed in Chapter 7. Specifics on this system's ability to perform chemical detection of liquid phase solvents and low level vapor phase (< 1ppm) solvent detection will be discussed and demonstrated. Studies characterizing the sensor's ability to produce repeatable and reproducible responses to analytes will be conducted. A unique sensor response to protein binding will be discussed. Finally, in Chapter 8, application of the packaged sensing system to monitoring water quality will be assessed. Practicality of the MPS flow-though sensing system is established by successfully demonstrating measurements of solvent contaminants in water.

## Chapter 2

# Macroporous Silicon as a Material

## 2.1 Technology overview

### 2.1.1 Porous silicon classifications

The International Union of Pure and Applied Chemistry (IUPAC) provides a classification system of pore size that can be seen in Table 2.1[14].

| Pore Width (nm) | Type of pore |
|---|---|
| ≤ 2 | micro |
| 2 - 50 | meso |
| > 50 | macro |

Table 2.1. IUPAC classification of various pore sizes [14].

PS in the form of meso- and/or micropores is commonly used in optical and luminescent technologies [15]. Pores within this range take on an entanglement-like structure with little to no order and exhibit high levels of porosity. MPS, a less porous material, has ordered pores which are smooth and straight. Figure 2.1 shows cross-sectional images of both micro- and macroporous silicon.

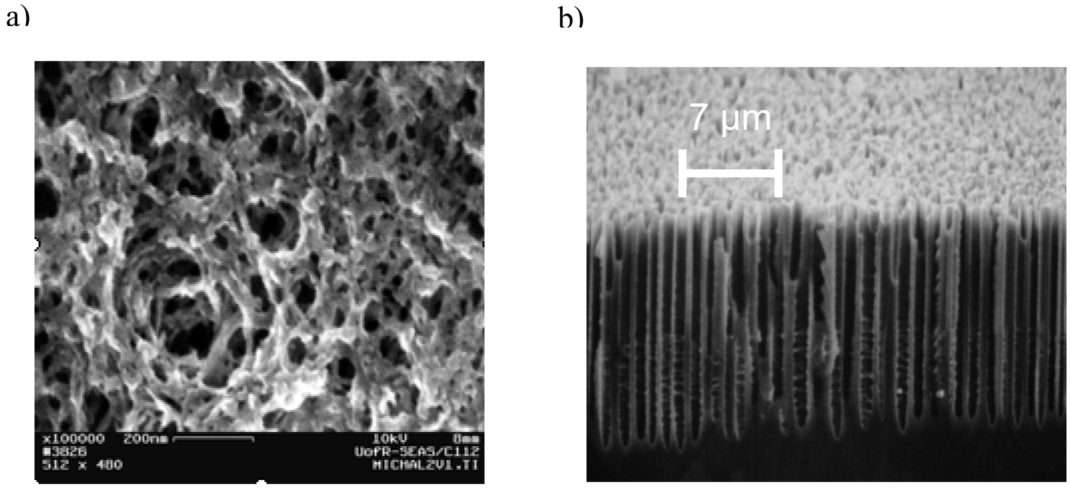

Figure 2.1. a) SEM image of microporous silicon where entangled pores are less than 2 nm in diameter. b) SEM cross-sectional view of macroporous silicon. Pore dimensions can be up to 100 µm deep and 1-2 µm in diameter.

Quantifying porosity is another important way to characterize PS films. Porosity is given as a percentage and is defined in Equation 2.1 [16].

$$P(\%) = \frac{m_1 - m_2}{m_1 - m_3} \tag{2.1}$$

where $m_1$ is the substrate weight prior to anodization, $m_2$ is the substrate weight just after anodization, and $m_3$ is the final weight after dissolution of the entire PS layer.

### 2.1.2 Fabrication techniques

Silicon with various levels of porosity can be made through many different process technologies such as thin-film deposition, deep reactive ion etching (DRIE), stain etching, and chemical processes. For the research proposed herein, MPS is created with an electrochemical etch process which anodizes Si. Often referred to as electrochemical etching of Si, this technique involves the application of a potential to a Si substrate that is in contact with an aqueous based hydrofluoric acid (HF) solution. Most commonly, meso- and micro- PS is formed with HF in solution with a solvent such as ethanol. For MPS formation in this work, a solution of dimethylformamide (DMF), an organic solvent, and HF is used. Ethanoic and DMF based solutions overcome wettability and capillary phenomena that commonly hinder PS formation [17-18]

### 2.1.3 Relevance of formation by anodization

In addition to electrochemical etching of Si, deep reactive ion etching (DRIE) is another common method used to create PS. DRIE systems are costly, mandating large laboratory footprints, complex wafer handling and chamber systems, plumbing for toxic gases, and radio frequency (RF) power supplies. Typically the cost of a DRIE system can range between \$500,000 and \$1,000,000. For bulk micromachining of Si, DRIE systems can achieve aspect ratios up to 1:80.

A more simplistic approach to micromachining bulk Si is electrochemical etching. These techniques require a conventional power supply, an etching cell, and access to HF and solvent chemistries; all of which are readily available for a considerably smaller cost. Electrochemically etched pores formed through means of chemical anodization exhibit smooth, straight sidewalls and have been reported to propagate through the entire thickness of a Si substrate. Table 2.2 summarizes porous silicon formation through means of electrochemical etching and DRIE technologies.

| | **System Cost** | **System Complexity** | **Throughput** | **Aspect Ratio** |
|---|---|---|---|---|
| **Anodization** | Low | Low | Low | Highest |
| **DRIE** | High | High | High | High |

Table 2.2. Comparison of anodization and DRIE techniques for the formation of MPS.

## 2.2 Theory of porous silicon formation

### 2.2.1 Proposed anodization chemistry

PS formation is not completely understood by the scientific community dedicated to it. Several reports, all of which are based on similar dissolution chemistries, by various groups have tried to explain the mechanisms of PS [19-29]. Of the many proposed dissolution chemistries, a more popular one is presented by Turner, Memming and Schwandt and is seen in Chemical Equation 2.2 [30-31].

$$\begin{aligned} &Si + 2HF + \lambda h^{+} \rightarrow SiF2 + 2H^{+} + (2- \lambda)e^{-} \\ &SiF2 + 2HF \rightarrow SiF4 + H2 \\ &SiF4 + 2HF \rightarrow H2SiF6 \end{aligned} \tag{2.2}$$

where $h^{+}$ and $e^{-}$ are exchanged hole and electron carriers, and $\lambda$ is the number of charges exchanged during the elementary step.

### 2.2.2 Engineering properties of porous silicon

Various characteristics such as pore diameter, shape, layer thickness, and porosity can be controlled during the electrochemical etching process. Table 2.3 summarizes the general characteristics of PS for given process conditions. It is stressed that PS formation is contingent upon the combination of various anodization conditions and adjusting only one specific parameter during formation may not directly result in a desired pore characteristic. Table 2.3 is not to be taken as a process key for engineering a specific PS layer. Rather, the table is to be taken as a general guideline for PS formation. The formation process must consider all process parameters including process chemistries [32].

| | Current density | HF:Solvent | Time | Substrate resistivity |
|---|---|---|---|---|
| **Pore diameter** | direct | indirect | little change | indirect |
| **Pore length** | direct | nonlinear | direct | linear |
| **Porosity** | direct | indirect | direct | nonlinear |

Table 2.3. Summary of general relationship between process parameters and resulting PS characteristics.

## 2.3 Overview of porous silicon formation

Theory from an incomplete understanding of PS can not provide all solutions for the fabrication of complex PS membrane sensing devices. Due to intense fabrication demands within the scope of this work, experimental fabrication will incorporate theory of PS but not rely on it explicitly. In addition to PS theory, fabrication will call upon experience and knowledge of IC and MEMS processing, and the ability to develop creative engineering solutions therein.

Prior experimental research has been conducted to identify and understand specific process considerations inherent to MPS. Similar to IC process technologies where every fabrication step mandates compatibility of subsequent processes, MPS enables unique process capabilities which are inherent in special process considerations.

### 2.3.1 Apparatus setup

Currently, a machined Teflon etching cell is used for the electrochemical etching process. The cell, as seen in Figure 2.2, has three main parts; two lids and a main body, all of which are fastened together with a series of three wing-nut bolts.

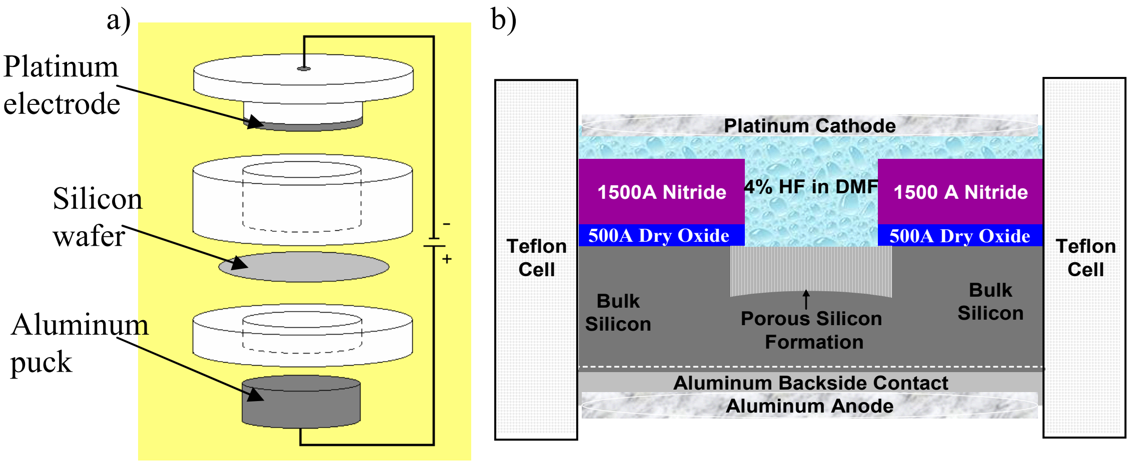

Figure 2.2. a) Schematic of electrochemical etch cell. b) Diagram of wafer in etch cell during electrochemical etching.

The lid of the etching cell has a piece of platinum film fixed to the bottom such that when it is covering the main cell's body, the platinum is submerged in the HF solution. The bottom lid houses a 4-inch diameter substrate with a liquid tight seal that is made possible with a rubber O-ring. Electrical contacts are made to the Pt film and wafer where a potential is applied with an Instek DC power supply, model PS-1850D.

### 2.3.2 Chemistries

A common problem associated with the chemical reaction necessary to form PS is the byproduct of hydrogen gas, which is released and sometimes accumulates, forming bubbles in the pores during the dissolution of Si. As hydrogen bubbles accumulate in a pore, electrolytes are blocked from penetrating pores and traveling to the propagation interface at the bottom. This in turn hinders pore propagation and can greatly affect etch rates and uniformity [33]. To overcome this problem, surfactants or wetting agents are used with HF. Common surfactants include Mirasol, absolute ethanol, acetonitrile, acetic acid, and DMF. For this work, DMF has been selected as the wetting agent. DMF, when used to form MPS, produces smoother and straighter sidewalls compared to that of $H_2O$

and acetonitrile based solutions. Figure 2.4 shows cross sectional SEM images of pore morphology for different chemical compositions [34].

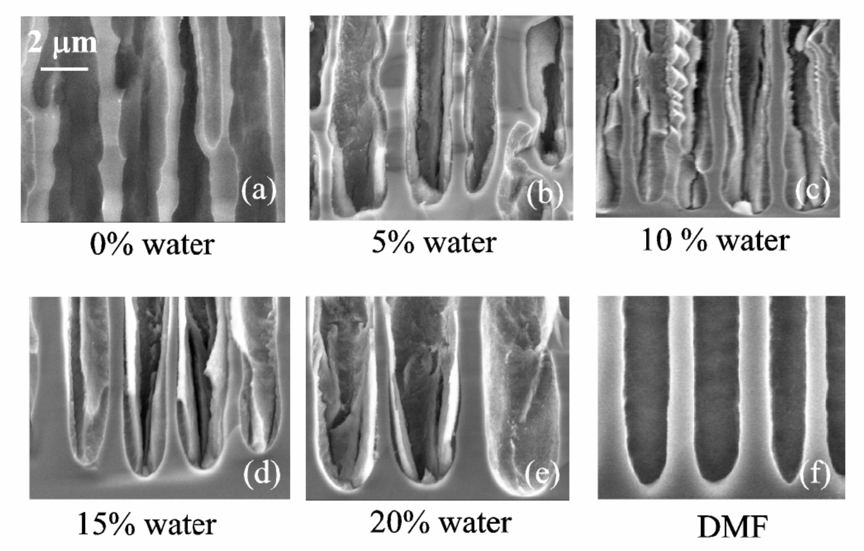

Figure 2.3. a) Cross sectional SEM images of MPS samples for various amounts of water by weight in acetonitrile based electrolyte (a to e) and DMF based electrolyte solution (f) [34].

Typical pore formation within this work utilizes a chemistry of 4% by volume of 49% concentrate HF acid in DMF. This concentration was previously found to be optimal for smooth, straight pores that propagate deep into the bulk of the substrate. [26, 35-37]

### 2.3.3 Current density

Typical current densities used to create micro and meso- porous silicon are on the order of 2 to 300 mA/cm$^2$ [38]. These current values are high compared to that used for MPS formation. To determine the appropriate current density, the desired pore morphology, chemistry being used, and pore propagation rate must all be taken into account. For a 4% by volume of 49% concentrate HF acid in DMF, it was found that the optimal current density is 4 mA/cm$^2$. This combination of chemistry and current density provides pores that extend about 60 μm deep and have smooth straight sidewalls with a diameter around 1.2 μm.

### 2.3.4 Unique fabrication schemes

A study investigating the effects of current density, time, refresh rates, and reverse biasing was conducted to further understand the MPS formation process. All experiments were run with a solution of 4% by volume of 49% concentrate HF acid in DMF. Table 2.4 presents a summary of the conditions used and results obtained.

| Run | Current Density (mA/cm^2) | Constant Current (mA) | Time (hrs) | Refresh @ | Pore Width | Center Pore Depth | Outer Pore Depth | Reverse Bias |
|---|---|---|---|---|---|---|---|---|
| 1 | 4 | 8 | 4 | none | 1um-1.2um | 48.96um | 68.12um | 0 |
| 2 | 4 | 8 | 4 | 2 hrs | 1um-1.2um | 50.56um | 73.26um | 0 |
| 3 | 6 | 12 | 4 | 2 hrs | 1.5um-1.6um | 34.90um | 48.41um | 0 |
| 4 | 2 | 4 | 4 | none | 2.2um-2.6um | 12.03um | 21.43um | 0 |
| 5 | 4 | 8 | 8 | 4 hrs | 1.61um | 66.63um | 102.4um | 0 |
| 6 | 4 | 8 | 6 | 3hrs, 2hrs, 1hr | 1.7um-2um | 45.88um | 68um | 0 |
| 7 | 4 | 8 | 6 | 3hrs, 2hrs, 1hr | processed | -- | -- | 0 |
| 8 | 4 | 8 | 6 | 3hrs, 2hrs, 1hr | processed | -- | -- | 0 |
| 9 | 4 | 8 | 6 | 3hrs, 2hrs, 1hr | 1.889um-1.986um | 59.00um | 78.52um | 1mA @ 3hrs/5hrs for 10 mins |
| 10 | 4 | 8 | 6 | 3hrs, 2hrs, 1hr | 1.350um-1.575um | 44.25um | 64.80um | 0.8mA @ 3hrs/5hrs for 18mins/12mins |

Table 2.4. Summary or pore characteristics for various processing conditions.

The diameter of pores achieved in this investigation ranged between 1 and 2.6 µm. A pore diameter of 1.1 µm is targeted during PS formation of sensing devices in this work. Figure 2.4 a) and b) shows SEM cross sectional images of runs 3 and 4.

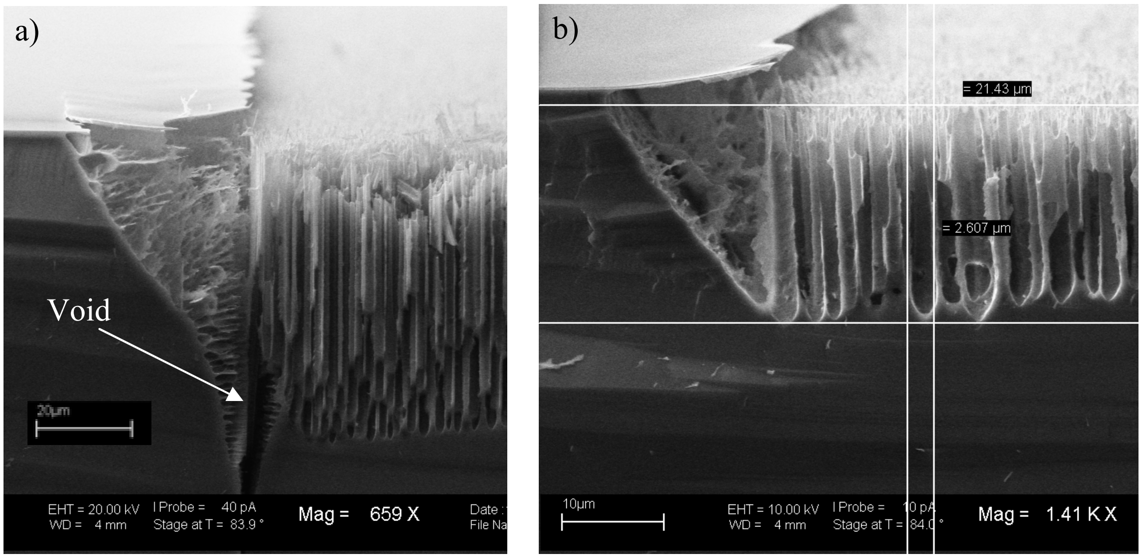

Figure 2.4. SEM cross-sectional views of MPS formed during runs 3 and 4. a) A current density of 6 mA/cm$^2$ for 4 hours and one chemical refresh. Trench formation occurs along the MPS region as seen as large dark void. b) Current density of 2 mA/cm$^2$ for 4 hours with no chemical refresh.

As seen in Figure 2.4 a), MPS formation with a current density of 6 mA/cm$^2$ causes trench formation along the parameter of the MPS region. This is a feature that could compromise the structural integrality of the MPS region when released as a free standing membrane. The shortest length and largest diameter pores achieved in this study are seen in Figure 2.4 b) and were created during experimental run 4 with a current density of 2 mA/cm$^2$. MPS made during this run is undesirable for field effect sensing because the larger diameter and shorter length pores do not exhibit large amounts of surface area which yield more sensitive devices. In addition to pore diameter, current density also influences pore depth. This can be concluded by looking at experimental runs 2, 3, and 4. Each run was conducted for a duration of 4 hours with a different current density. The deepest pores were created during experimental run 2 which used a current density of 4 mA/cm$^2$.

The pore depth is of primary concern because a thicker region of PS provides more surface area for localized field effects to modulate a space charge region in the semiconductor. The center pore depth ranged from 34.90 to 66.63 µm. Figure 2.5

displays the deepest pores which were achieved during run 5 utilizing one chemical refresh over the course of 8 hours at 4 mA/cm$^2$.

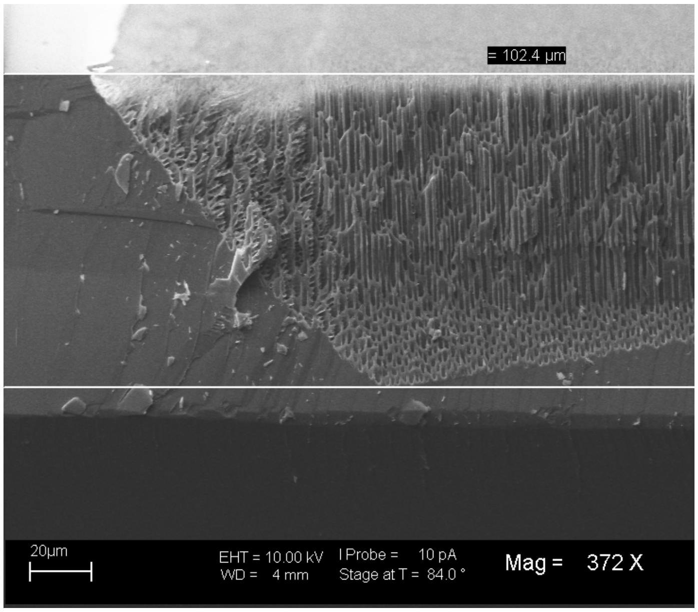

Figure 2.5. Cross-sectional SEM of the deepest pores achieved using a current density of 4 mA/cm$^2$ for 8 hours with one chemical refresh halfway through the run.

This run used the same process parameters as run 2 except for etch time, which lasted 8 instead of 4 hours. The increased etch time resulted in an inner and outer pore length 32 and 40%, respectively, longer than that of pores created during run 2.

It was postulated that fluorine ions in the solution were consumed at a rate which depleted the solution of ions prior to the completion of electrochemical etching. During experimental runs 2, 3, 5, 6, 7, 8, and 9 the chemistry in the etching cell was removed with a pipette and then replaced with fresh chemicals. Overall the replenishing of chemicals during the anodization process had little effect on pore formation. By comparing run 1 and 2 it is seen that chemical refreshing only slightly effects pore depth and has no effect on pore diameter. With a current density of 4 mA/cm$^2$, enough fluorine ions are present in the solution to support the dissolution reaction for 4 hours. If achieving maximum pore depth is a priority, chemical refreshing should be used for etching times greater than 4 hours.

### 2.3.5 Typical fabrication scheme

Electrochemical etching of Si in this work was most commonly performed on p-type, 5-15 ohm cm, (100) oriented, 4 inch Si substrates. During the anodization process, electrical contact must be made to the backside of the Si wafer. To achieve this, a $P^+$ backside region is created by doping the backside of the wafer with Emulsitone Borofilm 100, boron spin-on dopant. This results in a backside resistivity of approximately 2 Ωcm. Following this, 3000 Å of Al is sputtered over the $P^+$ backside forming an ohmic contact to the substrate.

Materials such as polysilicon, photoresist, nitride, and oxide can be used as a masking material during PS formation. For this work, an oxide nitride stack is used for the masking material. A typical masking scheme consists of growing a 500 Å thermal oxide followed by a low pressure chemical vapor deposition (LPCVD) of 1500 Å $Si_3N_4$. Figure 2.6 shows a cross-sectional schematic of a substrate following the MPS formation process.

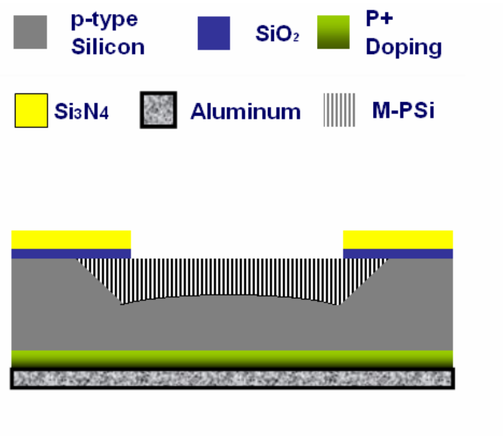

Figure 2.6. Cross-sectional schematic of a substrate showing oxide/nitride masking layers, backside ohmic contact, and MPS region after electrochemical etching.

The nitride film, serving as the primary masking material, has a very slow etch rate in HF. The underlying oxide film, which is easily etched in HF, reduces the oxide/nitride bi-layer film stress across the wafer and enhances nitride adhesion to the Si substrate. Although the use of an oxide film is advantageous for nitride film integrity, an undesirable undercut of the nitride film occurs when HF etches the oxide film from under it. Similar undercutting has been reported by H. Foll *et al*. [26]. Figure 2.7 shows the lateral undercutting resulting from this.

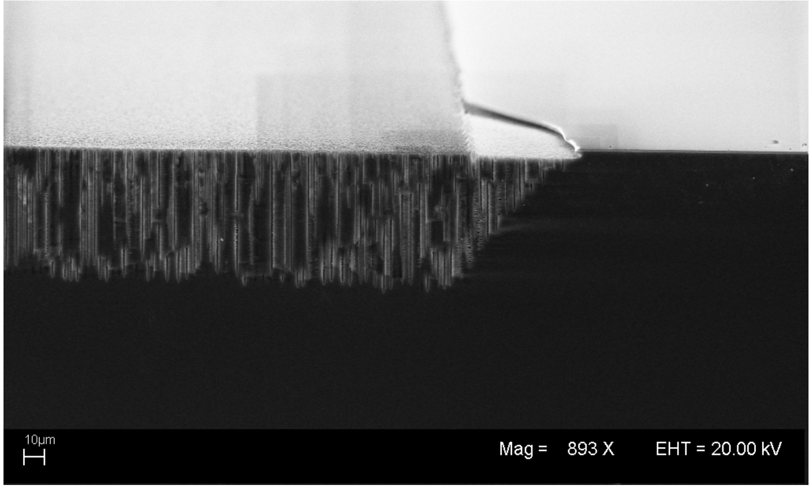

Figure 2.7. SEM cross sectional image of a substrate immediately following electrochemical etching. The MPS region, as seen in light and dark striations, was able to undercut the masking region due to oxide undercutting the nitride film, as evident in the suspended nitride film.

The undercut nitride film is suspended and can easily fracture. Therefore it is necessary to carefully consider this region when depositing and/or patterning metal contact electrodes across this region.

## 2.4 Summary

PS is a material that vastly ranges in pore depth, diameter, and orientation. Of the many techniques available for MPS formation, this work has chosen an electrochemical etching process which anodizes Si through a dissolution reaction involving HF and DMF.

Physical characteristics of MPS such as porosity, pore diameter, and pore depth are dependent on processing parameters such as current density, time, refresh rates, and chemical composition. It is important to realize that process parameters are dependent on one another and that adjusting one parameter might necessitate the adjustment of other parameters as well. Through experimentation, it was found that with an HF/DMF chemistry, time and current density had the largest effect on pore depth. During the electrochemical etching process a masking scheme consisting of an oxide/nitride bi-layer is used. Undesirable undercutting of the oxide film results in a larger MPS region than defined by the mask and the subsequent free standing nitride film must be considered during subsequent processes.

## Chapter 3

# Electrokinetic Theory of Fluid-Semiconductor Interfaces

### 3.1 Silicon as a semiconductor

The unique properties of semiconductor materials gave rise to the invention of the IC which has today evolved into complex microchips consisting of millions of electrical components. Through application of various technologies to semiconducting materials, scaled design and fabrication of complex circuits and systems has been achieved. The miniaturization of electronic circuits enhances their performance by reducing energy consumption and increasing device speed.

MEMS, a more recent evolution in the semiconductor industry, incorporates similar design and fabrication rules to produce greatly scaled mechanical structures which often make use of electrical circuits. IC fabrication utilizes many different semiconductor compositions such as Si, Ge, GaAs, and InP. MEMS technology most commonly makes uses Si substrates for device fabrication. The inherent nature of MEMS technology which utilizes semiconducting material to create mechanical structures requires theoretical understanding of both semiconductors and mechanics together.

In the case of this work, fluids are interfaced with Si and it is therefore the focus of this chapter to develop a theoretical understanding of such interactions. Semiconductor device physics and electrokinetics will be used to understand the behavior of the semiconductor material and fluid, respectively.

## 3.2 Metal-semiconductor contacts

The Fermi level, $E_F$ defines an energy level below which all available states are occupied at 0 °K. The position of the Fermi level is highly dependent on the concentration of impurities present in the silicon and can shift from the intrinsic position, $E_i$, towards the conduction or valance bands. In p-type silicon the Fermi level is at the bottom of the gap allowing valance electrons to jump into the acceptor levels leaving mobile holes in the valance band. When electrons leave the valance band and create a vacancy the remaining "hole" is positively charged. Figure 3.1 shows energy band diagrams for metal and a p-type semiconductor.

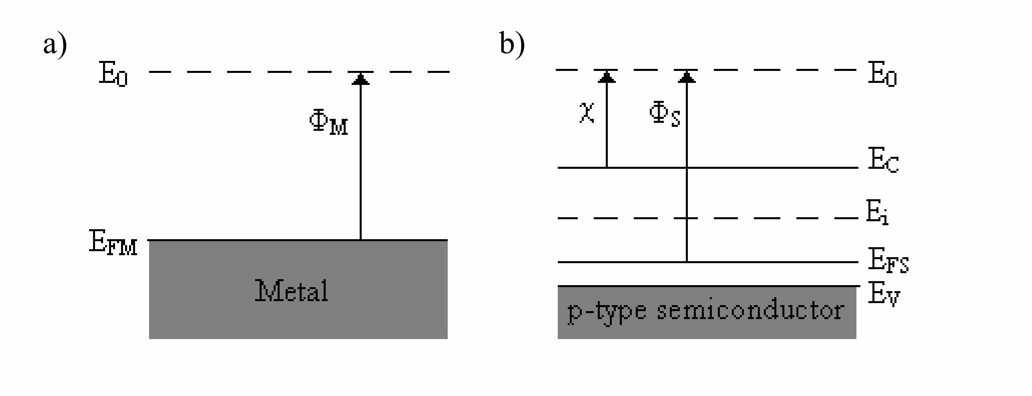

Figure 3.1. Energy band diagrams for a) metal and b) p-type semiconductor.

Under thermal equilibrium conditions, when two materials consisting of different band structures are brought into intimate contact, the Fermi energy level must remain constant as seen in Figure 3.2.

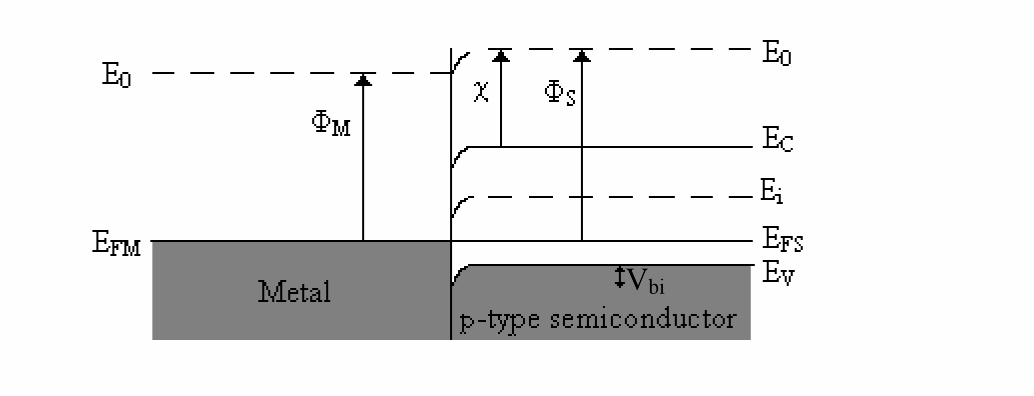

Figure 3.2. Energy band diagram for metal in intimate contact with a p-type semiconductor. The resulting $\Phi_M < \Phi_S$ contact is rectifying in nature.

For the case of a p-type semiconductor, a rectifying contact exists when $\Phi_M < \Phi_S$ and this can be seen in Figure 3.2. When $\Phi_M < \Phi_S$ in a p-type semiconductor, electrons flow from the metal to the semiconductor, which results in a negatively charged space charge region within the semiconductor. If $\Phi_M > \Phi_S$, for the case of a p-type semiconductor, the contact is considered to be ohmic in nature and charge transfer can be controlled in either direction by applying a bias to the junction. Figure 3.3 shows the energy band structure for an ohmic contact to a p-type semiconductor.

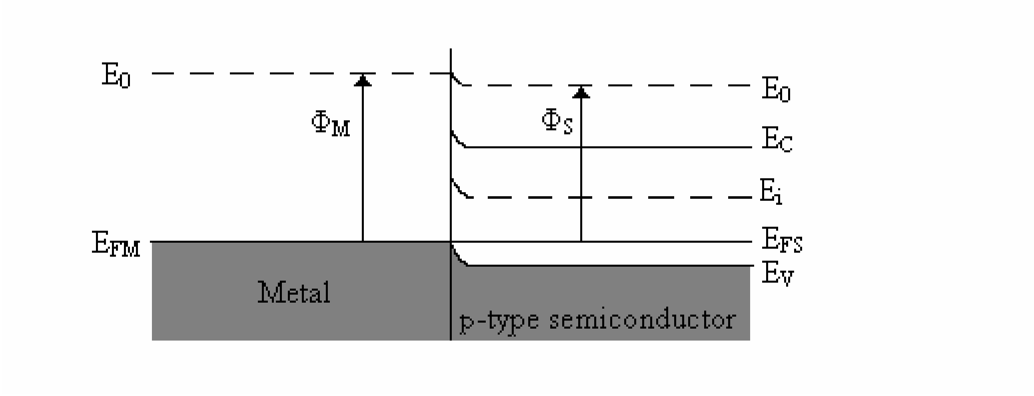

Figure 3.3. Energy band diagram for metal in intimate contact with a p-type semiconductor. The resulting $\Phi_M > \Phi_S$ contact is ohmic in nature.

Similarities can be drawn between metal-semiconductor contacts and fluid-semiconductor interfaces. Perhaps the most important consideration is the built-in potential, $V_{bi}$, where an internal potential barrier exists as a result of energy band bending.

$$V_{bi} = \frac{1}{q}\left[\phi_B - \left(E_C - E_F\right)_{FB}\right] \tag{3.1}$$

where

$$\phi_B = \phi_M - \chi \tag{3.2}$$

$\chi$ is the semiconductor electron affinity equal to 4.03 eV for silicon, $\Phi_M$ is the metal workfunction and is an invariant fundamental property of the specified metal, and $(E_C - E_F)_{FB}$ is the difference between the conduction and Fermi energy levels under zero field conditions.

## 3.3 Electrokinetic effects at fluid-semiconductor interfaces

Study of metal-semiconductor contacts can be used to understand the fluid-semiconductor interface. Much like the metal-semiconductor interface, the fluid-semiconductor interface exhibits unique electrokinetic effects that have a $V_{bi}$ associated with them. The following section will explain how a fluid-semiconductor interface leads to such a built in potential and develop a basis for quantifying it.

Consider Figure 3.4 where a fluid containing charged molecules or dipoles is brought into contact with a solid, p-type semiconductor surface.

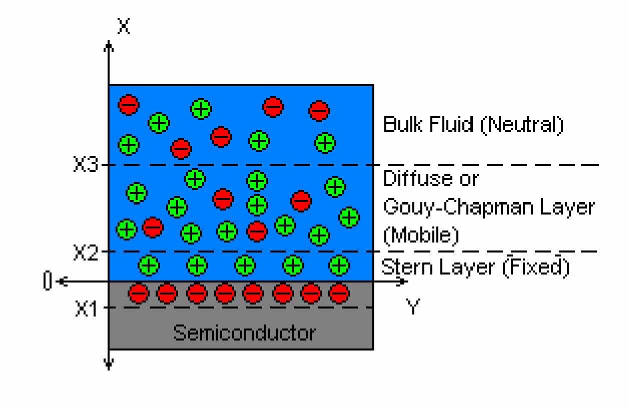

Figure 3.4. A p-type semiconductor interfaced with a fluid containing charged molecules.

Commonly the surface of semiconductor substrates are deprotonated or negatively charged. For the case of this work, substrates have been subject to mechanical polishing, chemical etching, and exposure to plasma based process tools, all of which create deprotonated surfaces [39]. Surfaces such as these attract charged molecules and dipoles in the fluid to the fluid-semiconductor interface. Migration of these dipoles and charged molecules occur in such a way that there is a net negative charge in the semiconductor region of X1 < X < 0 and a net positive charge in the fluid for 0 < X < X3. Applying the depletion approximation model to the semiconductor region and assuming a Boltzmann distribution of charge in the liquid at the interface, the spatial charge density can be graphically represented and seen in Figure 3.5.

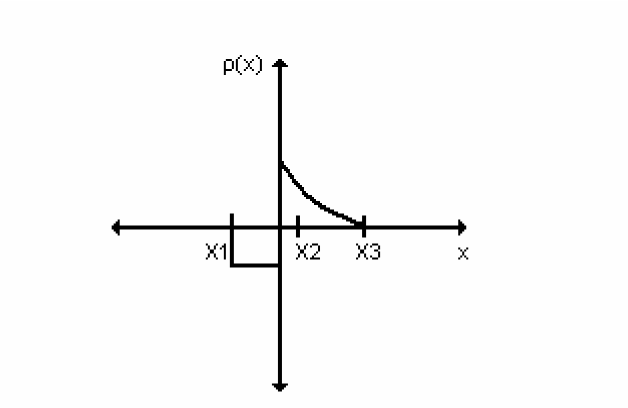

Figure 3.5. Graphical representation of charge density along the semiconductor-fluid interface.

Given the following relations:

$$\frac{d\varepsilon}{dx} = \frac{\rho(x)}{\in} \tag{3.3}$$

and

$$\frac{d\psi}{dx} = -\varepsilon(x) \tag{3.4}$$

where $\varepsilon$ (x) is the electric field, ρ(x) is the spatial charge density, ∈ is the permittivity of the material, and ψ is the potential, we combine them to form Poisson's equation:

$$\frac{d^2\psi}{dx^2} = \frac{-\rho(x)}{\in} \tag{3.5}$$

Assuming a constant permittivity throughout each material, Equation (3.3) can be used to solve for the electric field at the fluid-semiconductor interface and can be seen graphically in Figure 3.6.

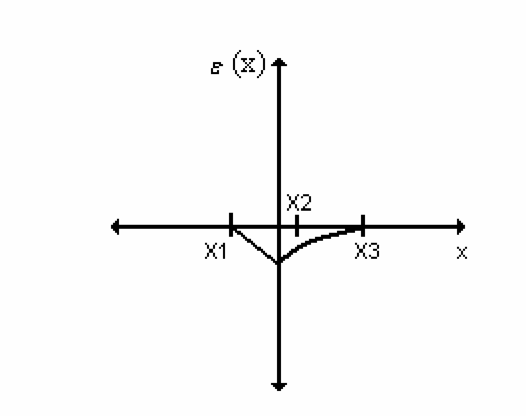

Figure 3.6. Graphical representation of electrical field along the semiconductor-fluid interface.

Placing Equation (3.4) into integral form and then solving for $\psi(X)$:

$$\psi(X) = \psi(0) - \int_0^X \varepsilon(x)dx \tag{3.6}$$

The potential at the fluid-semiconductor interface, $\Psi_S$ can now be solved and the potential across the interface is seen graphically in Figure 3.7.

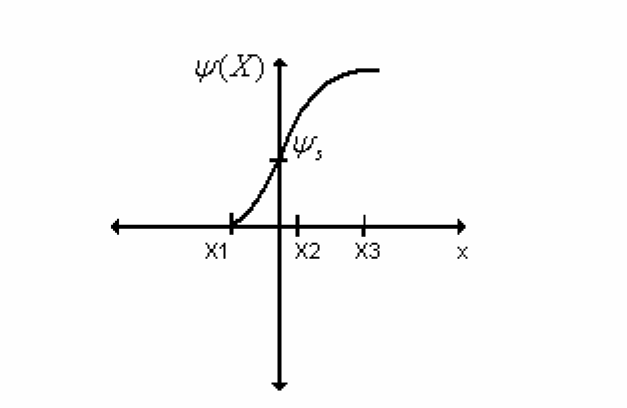

Figure 3.7. Graphical representation of potential along the semiconductor-fluid interface.

## 3.4 Capacitive modulation of the semiconductor

The depletion width into the semiconductor is defined as:

$$d_B = \sqrt{\frac{2 \in_s}{qN_A}}\sqrt{\psi_s} \tag{3.7}$$

The dependence on $\psi_s$ is key because various analyte materials migrate to the semiconductor surface with different molecular arrangements causing different potential values at the interface. In the semiconductor, the localized field effects at the interface clearly modulate the depletion region and this in turn modulates the charge per unit area in the depletion region, $Q^{'}_B$. The relation of $\psi_s$ to charge per unit area is:

$$Q_B^{'} = \sqrt{2q \in_s N_A}\sqrt{\psi_s} \tag{3.8}$$

As $Q^{'}_B$ is modulated, the capacitance, $C_B$, of the depletion region also changes as defined by:

$$C^{'}_B = \left| \frac{dQ_B^{'}}{dV} \right| \tag{3.9}$$

where $Q'_B$ is charge in the depletion region, and V is the potential drop across the depletion region. The capacitance in the depletion region per unit area, $C_B'$, is then:

$$C_B^{'} = \sqrt{\frac{\in_s qN_A}{2V_{bi}}} \tag{3.10}$$

$V_{bi}$ is the built-in potential as a result of the fluid-semiconductor interface and is defined as:

$$V_{bi} = \frac{kT}{q}\ln\left(\frac{N_A N_{L+}}{n_i^2}\right) \tag{3.11}$$

where k is Boltzmann's constant equal to $8.617X10^{-5}$ eV/K, T is temperature, q is the magnitude of electronic charge equal to $1.602X10^{-19}$ C, $N_A$ is the number of acceptor atoms per $cm^3$, $N_{L+}$ is the equivalent number of positively charged atoms with a magnitude of electronic charge q taken at X3 as seen in Figure 3.7, and $n_i$ is the intrinsic carrier concentration.

Figure 3.8 depicts the potential previously solved for in Equation 3.6 in conjunction with Figure 3.4.

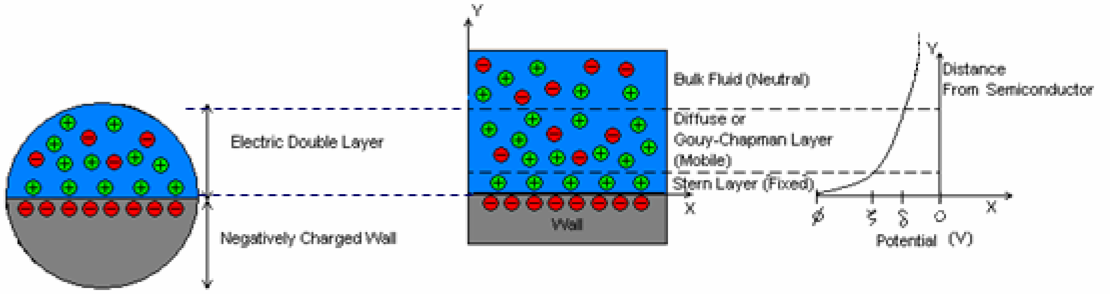

Figure 3.8. Graphical representation of potential within fluid containing charged molecules.

The Stern layer has the highest potential in the fluid and is found between the wall potential, Φ, and the zeta potential, ζ. The charged molecules and dipoles comprising this layer are electrostatically fixed to the surface of the semiconductor by a localized electric field as seen in Figure 3.8. Traveling further from the semiconductor surface, the fluid contains less net positive charge resulting in a lower potential, between ζ and δ, until the bulk of the fluid is reached where no net charge is present.

Another way to investigate capacitive modulations in the semiconductor is to assume a Boltzmann distribution of charge in the electric double layer and relate the charge density and potential in the electric double layer with the Poisson relationship in Equation 3.5. This is referred to as the Boltzmann's equation of state charge density:

$$\rho = 2FzC_{\infty} \sinh\left(\frac{qz\psi}{kT}\right) \qquad (3.12)$$

where ρ is the state charge density, F is Faraday's constant equal to 9.65 X $10^4$ C $\text{mol}^{-1}$, z is the valance number of each ion, and $C_\infty$ is the concentration of ions far from the interface.

Substituting this into Poisson's equation, Equation 3.5:

$$\frac{d^2\psi}{dx^2} = \frac{2FzC_\infty \sinh\left(\frac{qz\psi}{kT}\right)}{\in} \tag{3.13}$$

This equation is non-linear and must be solved by assuming Debye-Huckel's limit of a thin electric double layer. This assumes that the electric double layer is very small compared to the bulk of the fluid. Then, by approximating the hyperbolic sine term with the first term of its Taylor series expansion:

$$\frac{d^2\psi}{dx^2} = \frac{\psi}{\lambda_D^2} \tag{3.14}$$

where $\lambda_D$ is the Debye length of the electrolyte in the fluid and is related as:

$$\lambda_D^2 = \sqrt{\frac{\in \frac{kT}{q}}{2z^2FC_\infty}} \tag{3.15}$$

The Debye length defines the mobile Diffuse or Gouy-Chapman layer and can be seen graphically:

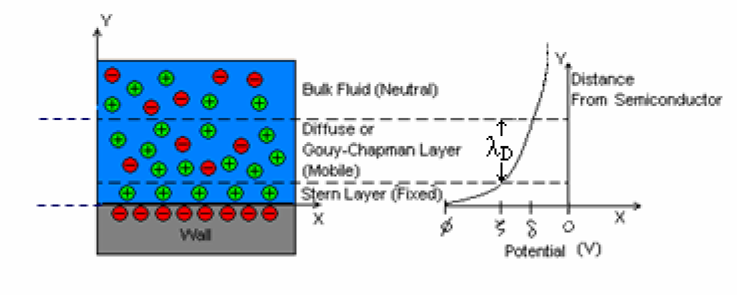

Figure 3.9. Graphical representation of a Boltzmann distribution of charge in the electric double layer and the decaying relationship of the Debye length in the electrolyte.

Solving the differential Equation 3.14:

$$\psi = \psi_s \exp\left(\frac{-x}{\lambda_D}\right) \tag{3.16}$$

Equation 3.16 shows the exponential relationship of the potential as a function of distance from the semiconductor-fluid interface as seen in Figures 3.8 and 3.9.

### 3.5 Influence of an interfacial oxide

In some cases a thermally grown or thin native layer of oxide may be present over the semiconducting surface. The presence of this provides electrical isolation between the liquid and semiconductor, and interaction between the two is achieved through a coupling mechanism. Figure 3.10 is a flat band diagram for a metal-oxide-semiconductor (MOS).

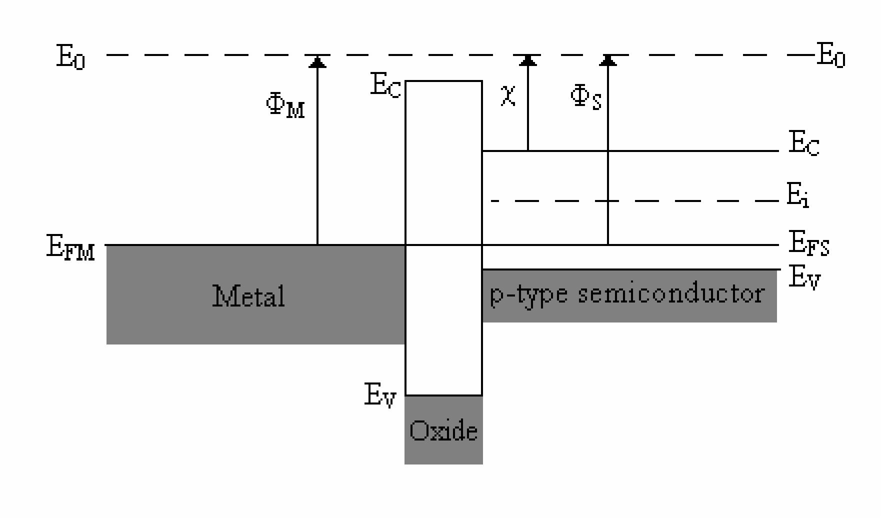

Figure 3.10. Flat band energy band diagram for a MOS structure.

Application of a potential upon the metal surface causes a localized field in the semiconductor much like that described in Section 3.4. In this case, the localized field is between the metal surface and the semiconductor. Under these conditions a potential drop across the oxide is experienced as seen in Figure 3.11.

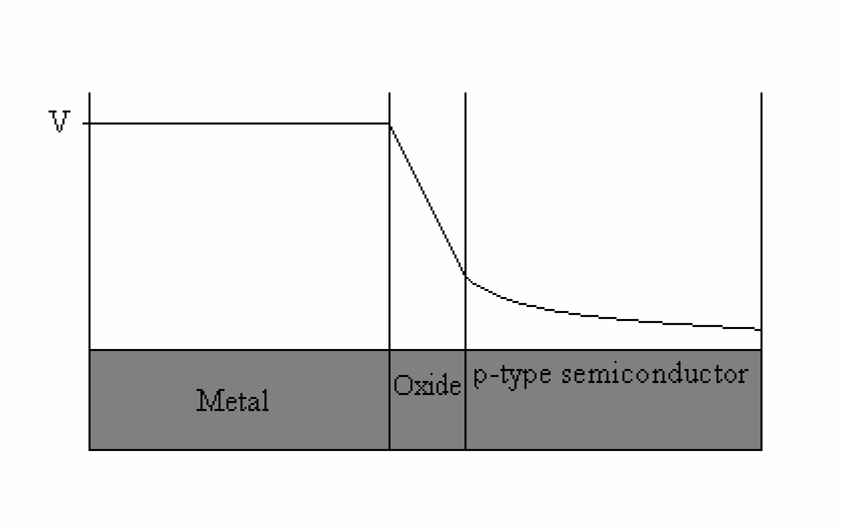

Figure 3.11. Potential drop across a MOS structure.

The application of potential to the MOS structure is similar to that of having charged molecules in contact with an oxide over a semiconductor surface. A localized field is established through oxide and modulation of a space charge region in the semiconductor occurs.

## 3.6 Summary

With regard to electrical sensing models, a number of reports have been published, most of which are based on charge distribution of polar analyte molecules and field effects which modulate space charge regions in semiconductors [40-45]. Theoretical development of physical behavior of fluid-semiconductor interfaces is critical for understanding the sensing mechanism of the device presented in this work. The deprotonated surface of a semiconductor attracts charged molecules in a fluid resulting in a net charge density on each side of the interface. The charge density can be related to an electric field present in both the fluid and semiconductor. From Poisson's equation it is shown that a potential is present at the interface and exhibits an exponential decay as one travels from the fluid-semiconductor interface into the bulk of the fluid. The presence of a potential, which is strongest at the interface, results in the modulation of the space charge region in the semiconductor. The capacitance of the semiconductor, being related to the space charge region, is also modulated and measurements of this can be related to levels and composition of charged particles in the fluid.

## Chapter 4

# Device Operation

### 4.1 Liquid phase operation

A linear array of four sensors along an elongated flow-through structure is mounted to a fluidic system as seen in Figure 4.1.

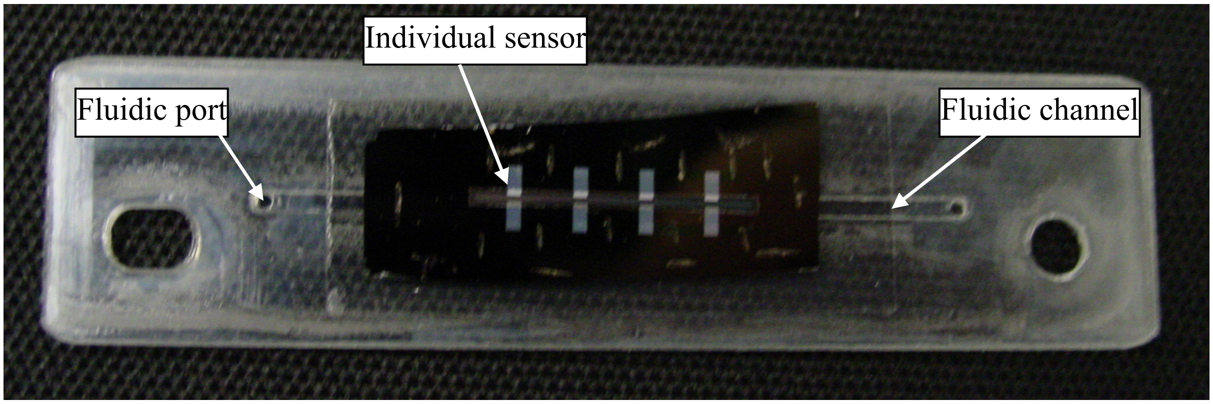

Figure 4.1. A packaged sensing device.

Liquid can be pumped into the input port of the fluidic card and distributed in accordance to the design of the fluidic system. In some areas, the liquid will travel along a channel in the card and be transported to the backside of the sensor containing a MPS membrane. With the presence of liquid next to the membrane, capillary action draws a tiny portion of this into the MPS sensing membrane resulting in a measurable electrical response.

An extraordinary amount of liquid-semiconductor interface is present within a liquid filled MPS membrane. Recalling theory from Chapter 3, it is clear that a localized field at the liquid-semiconductor interface is established and the semiconductor experiences a modulation of the space charge region. This can be measured with AC conductivity measurements which are related to the capacitance seen across the liquid filled MPS membrane.

Properties such as dielectric constant, dipole moment, and vapor pressure make each liquid interface with the sensor different and unique capacitive signatures can be seen over a period of time. Typically, an 8 μl sample fills the backside channel of the flow-through structure and capacitive measurements are taken until the liquid is completely evaporated. This results in characteristic signatures for various liquid phase solvents as seen in Figure 4.2.

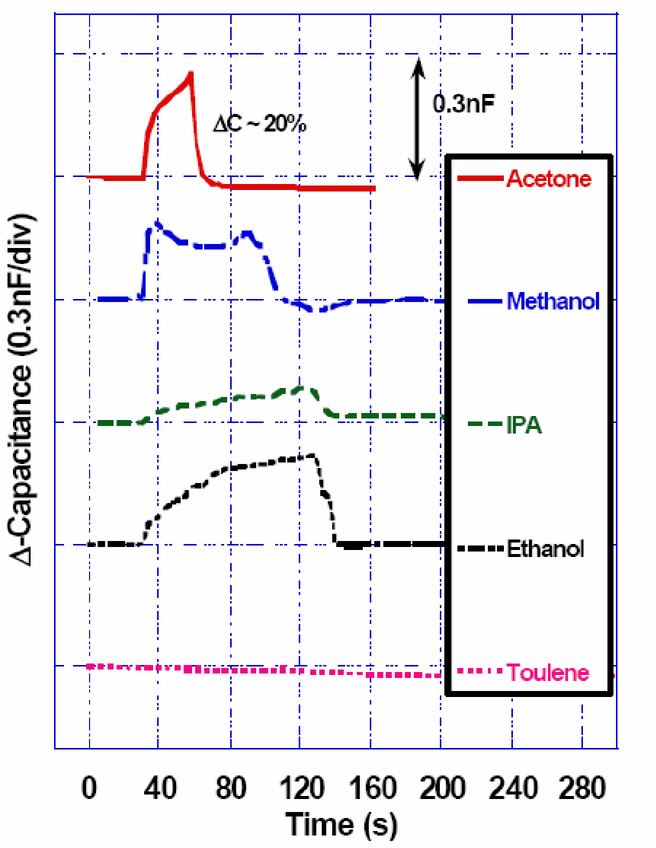

Figure 4.2. Unique capacitive signatures for various solvents detected in their liquid phase.

During liquid phase sensing with this device, the typical maximum change in capacitance is on the order of tenths of nanofarads with a baseline capacitance in the nanofarad range. The duration of the signatures are dependent on the rate of evaporation because this dictates the period of time the semiconductor is experiencing space charge modulation. As seen in Chapter 8, solvents typically exhibit short spike-like signatures lasting only seconds, whereas water exhibits a signature similar to that of a square wave lasting several minutes. If the signatures of analyte targets are known ahead of time, discrimination between various targets can be achieved as seen in Figure 4.2.

## 4.2 Vapor phase operation

Vapor phase sensing with this device does not require the addition of a fluidic system. Sensors placed in the vicinity of solvent in vapor form are capable of detecting concentrations < 1 ppm. Discrimination between various chemical vapors or identification of a specific chemical vapor is more difficult to achieve under vapor phase sensing conditions. Current work suggests that this sensor system is most applicable for determining concentration levels of a known chemical vapor.

The sensing mechanism for vapor phase operation of MPS material is adsorption. It is hypothesized that for vapor phase sensing, a localized field effect similar to that of liquid phase operation is experienced. Furthermore, it is believed that the only difference between liquid and vapor phase sensing is that a much smaller level of solvent-semiconductor interface exists during vapor phase sensing.

A MPS membrane in the presence of solvent vapor typically experiences an increase in capacitance as the concentration of solvent in its vapor phase increases. The maximum capacitive change measured for solvent vapors is on the order of picofarads. This is three orders of magnitude smaller than that of liquid phase detection. Figure 4.3 shows capacitance values measured across a sensing membrane as a pool of acetone evaporates inside a chamber with a monitoring device.

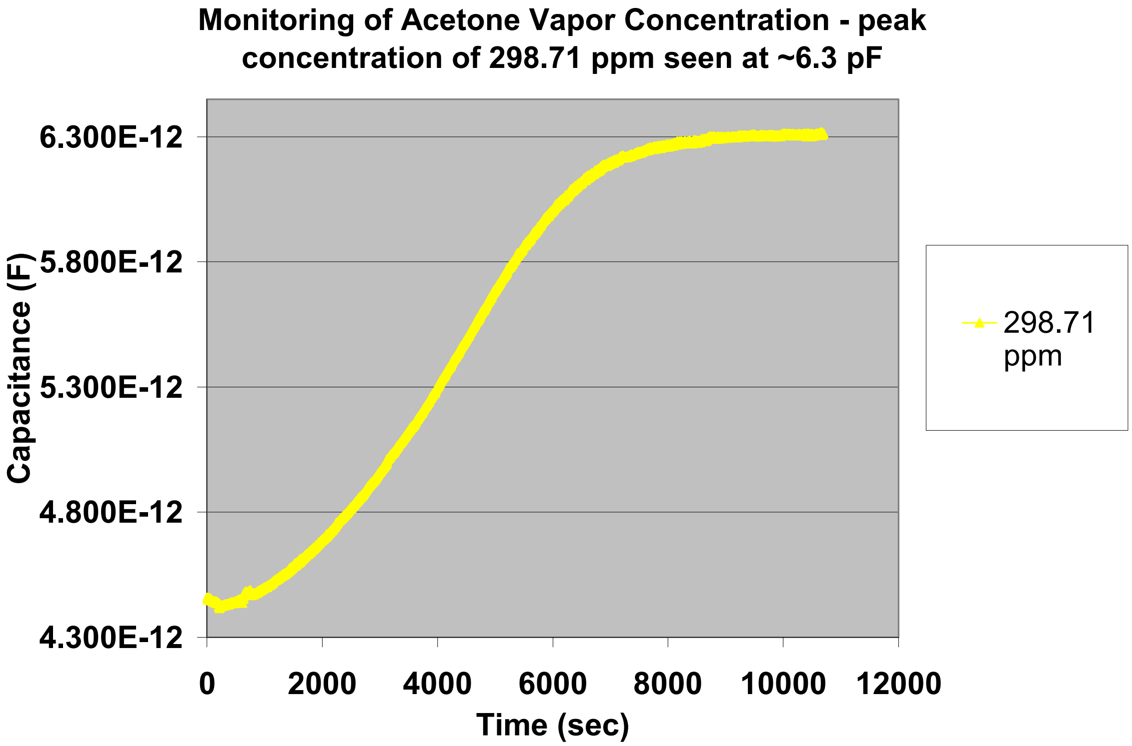

Figure 4.3. A pool of acetone is monitored as it evaporates and its vapor fills an enclosed chamber. In this case, the maximum concentration of vapor phase acetone is 298.71 ppm. This occurs when the pool of acetone has completely evaporated and a maximum capacitance of ~ 6.3 nF is measured.

A solvent in vapor phase consists of many small liquid droplets that have become airborne. It is possible that the MPS membrane is interacting with these small droplets which are suspended in air, very close to the semiconductor surface. As the concentration of solvent vapor increases, more droplets are adsorbed in the membrane region. This can leads to additional interaction with the semiconductor surface and an increase in capacitance.

Compared to liquid phase operation, where the MPS membrane is saturated with a given solvent and the solvent-semiconductor interface is high, vapor phase operation doesn't experience such high levels of solvent-semiconductor interface. This could explain why the measured capacitance during vapor phase sensing is several orders of magnitude lower than that of liquid phase detection.

## 4.3 Operation for biological sensing

This device is capable of detecting biological events such as hybridization of complementary DNA (cDNA) [13, 34]. Potential for applications in the fields of biological and medical science are extremely high and much room for research still remains in this area. Figure 4.4 shows detection of cDNA using MPS material.

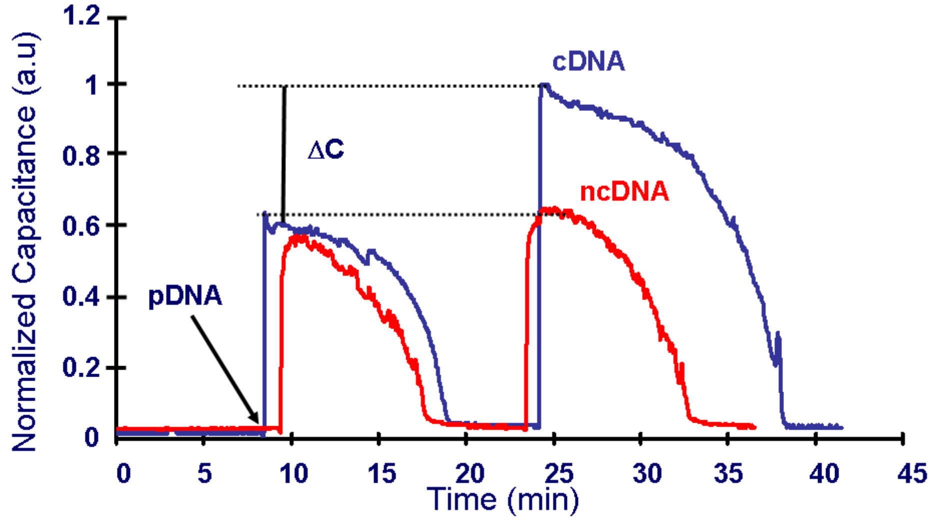

Figure 4.4. When cDNA hybridizes with pDNA it exhibits a 40% higher capacitive signal than that of ncDNA [13].

DNA sensing is done by functionalizing a semiconductor surface in such a way that strands of probe DNA (pDNA) are affixed to it. Ideally, pDNA will attach only to specific strands of cDNA. Such complementary matching of base pairs between probe and complementary DNA strands is known as hybridization. A measurable difference in capacitance is seen between a MPS region filled with solely pDNA and a MPS region filled with pDNA attached to cDNA. In some cases, strands of pDNA will bind to other noncomplementary DNA (ncDNA) strands. This undesirable situation is referred to as nonspecific binding and can lead to complications in quantifying the number of actual hybridized cDNA strands.

The device in this work was used to detect binding events of protein. Figure 4.5 a) and b) are schematics of an amine-biotin-streptavidin chain attached to a semiconductor surface and a representation of the binding between biotin and streptavidin protein.

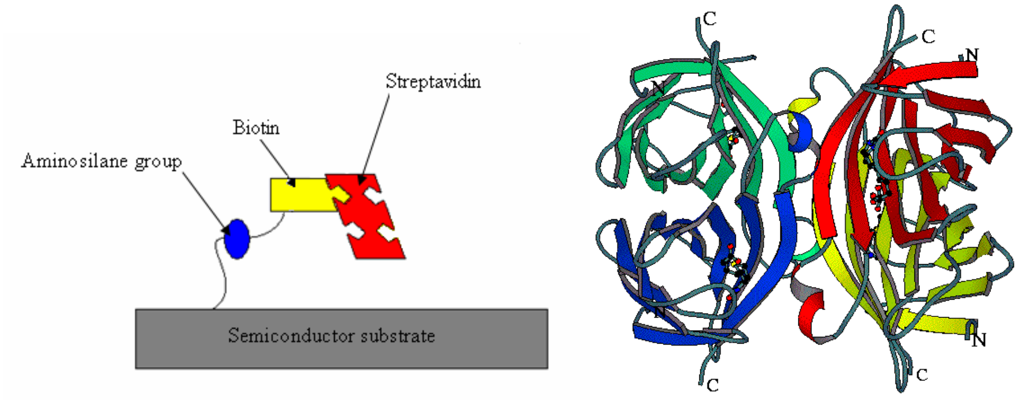

Figure 4.5. a) Schematic view of amine-biotin-streptavidin chain attached to a semiconductor surface. b) Secondary protein structure of streptavidin with each monomer bonded to a biotin protein.

A detailed procedure for this can be found in part A of the appendix. Similar to DNA biochemistries, protein sensing is done by functionalizing the semiconductor surface within the MPS sensing region with an amine group [46-47]. Biotin, a protein found in vitamin B complex, is flushed through the functionalized MPS membrane and readily binds to amine groups [48-49]. Baseline capacitive measurements are taken across the membrane with the amine-biotin chain linked to the semiconductor surface. Streptavidin, a protein that has a high affinity to biotin, is then flushed through the MPS membrane [50-52]. Binding events between biotin and streptavidin occur and a change in capacitance is seen across the sensing membrane. The addition of streptavidin to the fixed chains in the sensing membrane provides additional modulation of localized fields at the semiconductor surface which results in a change in capacitance measured in the MPS membrane.

## 4.4 Operation with pore infiltration

Another potential way to utilize this device is to infiltrate the MPS sensing membrane with a specific material that demonstrates a unique electrical response of its own. By using a material that is only sensitive to a specific gas, such as palladium is to hydrogen, the sensing membrane could demonstrate specificity between various gases it encounters [53-54]. This could lead to discrimination between analytes, or even provide an amplified electrical response. Polymers containing carbon nanotubes have demonstrated an electrical response to various solvents [55]. Figure 4.6 shows a MPS flow-through sensing membrane infiltrated with polyvinyl acetate containing single walled carbon nanotubes.

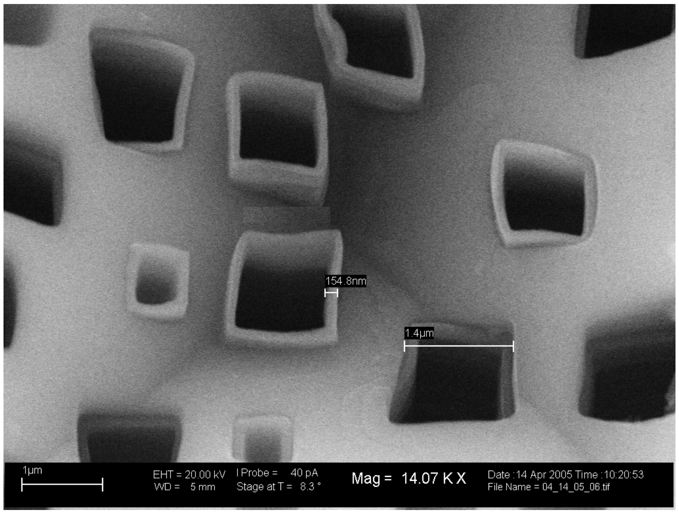

Figure 4.6. SEM image of individual pores as seen as black square regions are infiltrated with a polymer seen as light colored liners.

It is probable that an increase in sensitivity to very small analyte concentrations can be achieved with the use of such materials if the reaction of the infiltrated material to the analyte provides more space charge modulation in the semiconductor than the analyte would itself.

## 4.5 Concluding remarks

The sensing platform presented in the work offers a large degree of versatility in sensing and detection operations. This is in large part due to the monolithic integration of the electrical and fluidic systems which have been combined to form a flow-through sensing membrane structure. This structure allows precise analyte handling and establishes a self-aligned backside fluidic channel such that the position of the channel on the backside defines where the sensing membrane is on the frontside. Upcoming chapters will explain in more detail the development of the flow-through structure and the many applications enabled because of it.

## Chapter 5

# Micromachining Process for Macroporous Silicon Flow-Through Sensing Membranes

## 5.1 Background and history

Initial achievements in sensing with MPS have been achieved with a proof of concept device that was capable of detecting hybridization of DNA [13]. The work laid the groundwork necessary to successfully design and fabricate a fully functional system consisting of both electrical and fluidic systems for sensing operations in both chemical and biological domains.

### 5.1.1 First generation device

The first generation (GEN-1) design consisted of a large square MPS region positioned between two parallel electrodes as seen in Figure 5.1.

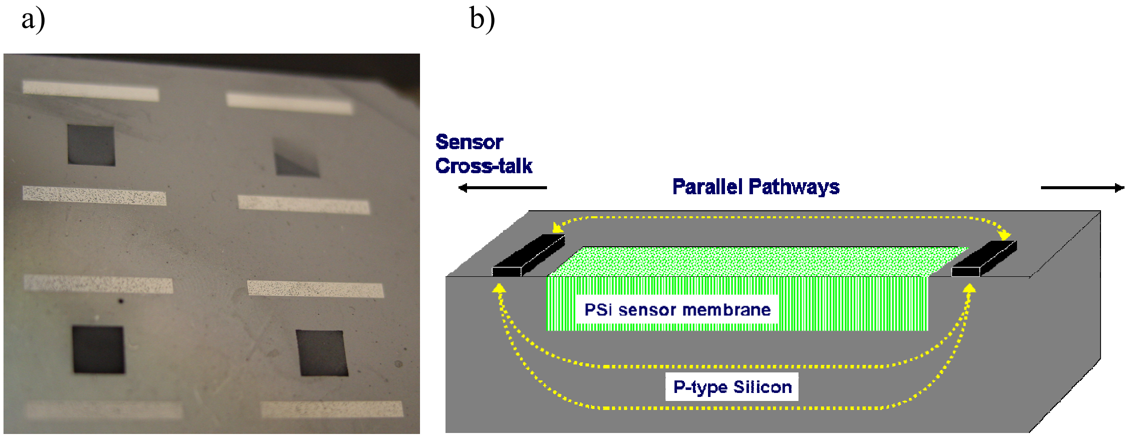

Figure 5.1. a) Top-down image of four, GEN-1 devices. MPS regions are represented by dark square regions and electrodes seen as light colored rectangular strips that are placed on either side for electrical measurements. b) Cross-sectional schematic of parasitic pathways between electrodes [13].

While the device demonstrated the ability to perform chemical and biological sensing, the capabilities in these areas were limited and large development efforts were necessary to advance this sensing platform into a practical sensing tool.

### 5.1.2 Need for improvements

During the design phase of GEN-1 devices, no consideration of integrating a fluidic system for sample delivery was made. The device relied upon an operator's ability to accurately dispense analytes over the MPS region. Such a procedure proved to be a challenge because fluid placed on the PS region had a tendency to uncontrollably spread across the device creating electrical shorts between the electrodes.

This device had an undesirable electrode design, as seen in Figure 5.1 b), because the locations are such that cross-talk through the bulk of the substrate is possible during AC electrical measurements. Furthermore, the electrodes were not in explicit contact with the MPS region. Better electrode isolation and intimate contact to the MPS region can reduce cross-talk and increase the signal-to-noise ratio resulting in a more sensitive device.

The large size of GEN-1 sensors was not favorable for arrayed configurations. A smaller sensor design is necessary to array multiple sensors on a single chip. A scaled sensor reduces the necessary sample size, increases the number of sensing opportunities per chip, and raises confidence levels in detection of chemical and biological materials.

## 5.2 Introduction to porous silicon flow-through structures

Figure 5.2 is a cross-sectional view of a MPS flow-through structure. In this structure, a freestanding MPS membrane is intersected by a KOH etched backside channel. When a fluid is placed into the channel, capillary action draws a small portion into the sensing membrane. Aluminum electrodes, which are isolated from one another and in contact to the PS sensing membrane, are used for AC based electrical measurements.

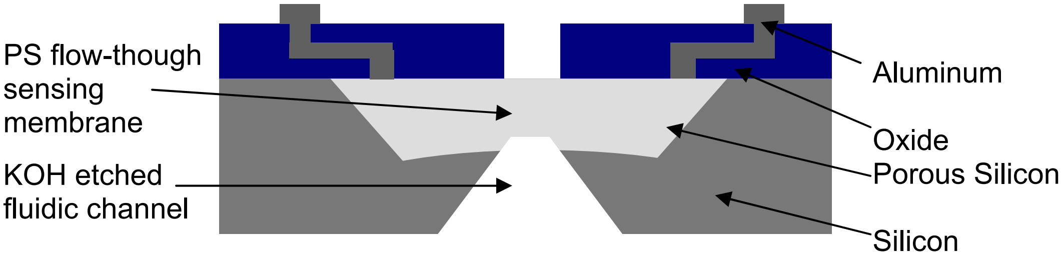

Figure 5.2. Cross-sectional schematic view of the MPS flow-through structure.

### 5.2.1 Structure advantages

Many advantages occur when integrating the MPS sensing membrane directly into a backside fluidic channel. Fluidic systems are often thought of as an additive process where a separate substrate containing the entire fluidic system is bonded to the substrate with the sensing device. This gives rise to complex fabrication schemes, compatibility issues between the different substrates, and increased fabrication cost. Monolithic integration of the sensing membrane and the fluidic channels allows the entire device to be made with one fabrication sequence. To enclose the channels, a capping substrate must be bonded to the back of this structure and this can be done with well developed, standard bonding techniques [56].

Another advantage of this structure can be found in taking electrical measurements. As seen in Figure 5.2, the pathway from one electrode to the next must pass through the sensing membrane. If the KOH-etched fluidic channel did not intersect the MPS region, a parasitic pathway between the electrodes through the bulk of the wafer would be present. This would reduce the sensitivity of the device and further complicate electrical modeling of device performance.

Lastly, the integration of sensing membranes into the fluidic system simplifies sample delivery. The fluidic system can consistently deliver accurate sample volumes into the sensing membrane region. Other delivery techniques, such as using micropipettes to dispense analytes into the sensing regions by hand, can result in difficulties in controlling sample size and problems in accurately dispensing to specific locations.

### 5.2.2 Structure considerations

The flow-through structure is unique in that it is three-dimensional and presents a large degree of topography. Typical IC fabrication schemes are limited to highly planar devices. Bulk micromachining, a technology often used in MEMS fabrication, often deals with structures involving a larger degree of topology; however, these structures are rarely sculpted through the entire thickness of a substrate. For successful fabrication of this device, it is necessary to develop a scheme that meets fabrication challenges rarely encountered. By harnessing well developed IC and MEMS fabrication processes and incorporating creative engineering solutions to resolve unconventional fabrication challenges, flow-through structures can be successfully fabricated.

### 5.2.3 Gateway theory

The monolithic integration strategy in this work makes use of MPS as a gateway to interface the electrical and fluidic domains. In doing this, the MPS material, acting as a sensing membrane, will be used in a flow-through structure to transport an analyte, or fluidic sample under investigation, from fluidic channels on one side of the chip to sensing electrodes on the other. The integral nature of this flow-through structure results in the creation of sensing regions and fluidic interconnects at the same time. This is unique in that it establishes means for fluidic transport and analyte detection monolithically in the same device.

## 5.3 Investigation of macrosquare design

### 5.3.1 Device design

The macrosquare was the first design that was developed to circumvent several design problems of the GEN-1 device. As seen in Figure 5.3 a) and b), the device consists of alternating MPS and Al square-annuli on top of a Si substrate. The two Al square-annuli act as electrodes and the MPS found between these serves as the sensing region. An additional $N^+$ doped MPS square-annulus around the parameter of the device provides isolation from other devices in an arrayed configuration. This design makes use of the flow-through structure by creating a backside cavity with a KOH etch aligned to the PS sensing region.

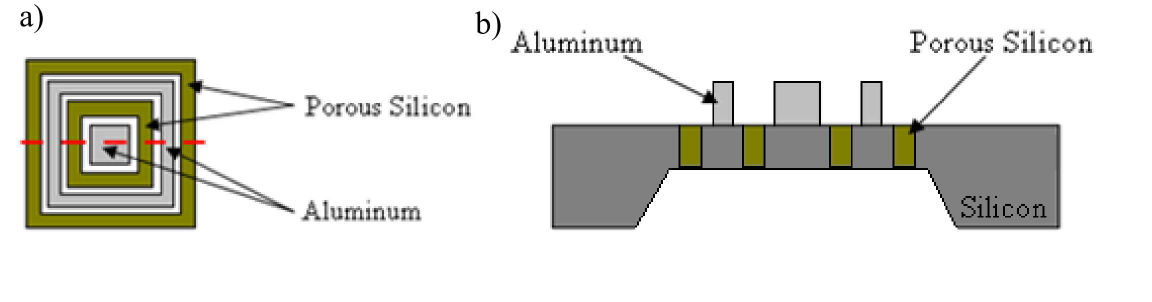

Figure 5.3. a) Top-down schematic of macrosquare design consisting of alternating aluminum and PS square-annuli. b) Cross-sectional schematic of macrosquare design.

### 5.3.2 Device advantages

This design provided many improvements over the GEN-1 design presented in Section 5.1. The largest improvement was device isolation established through a backside KOH etch. The path for the signal between electrodes was explicitly through the sensing membrane; there were no escape paths into the bulk as seen in the GEN-1 device.

### 5.3.3 Device disadvantages

The primary challenge of this device is found in the fabrication process during the backside KOH etch process. During the time of fabrication, there was little understanding of how to interface the MPS sensing region with a KOH etch without causing damage to the MPS material. As seen in Figure 5.4, when a planar KOH etch front meets the curved profile of the PS region, a Si plug blocking the desired flow-through region remains. As KOH comes into contact with MPS, many exposed (111) planes are rapidly etched and the membrane is destroyed before the remaining Si plug is etched away.

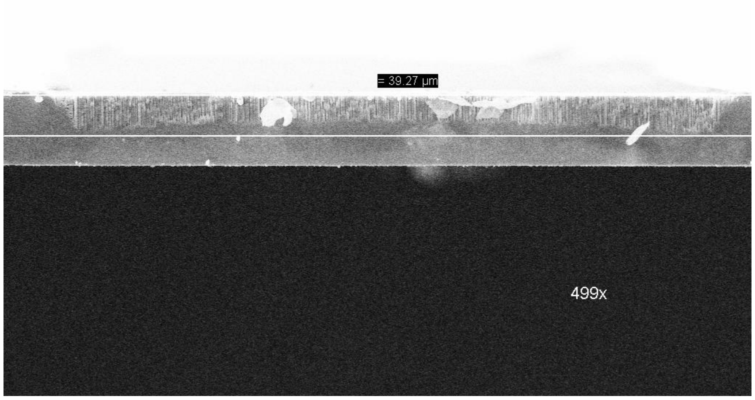

Figure 5.4. Cross-sectional SEM of a planar KOH etch front approaching a MPS region. A white line has been positioned along the bottom of the MPS region to help visualize the curved profile.

Several macrosquare devices were fabricated, none of which had flow-through membranes. The size of the resulting KOH etched cavity would be quite large and this could make the device extremely delicate. This larger scale device is 64 $mm^2$ and requires a large sample volume estimated to be approximately 100 µl for operation. Another concern associated with this design is that the center electrode is completely encased by the outer. A design such as this does not permit the electrodes to have lead-outs in a configuration that eases rapid test probing or packaging. Wire bonding to the center electrode, positioned atop of the Si membrane is necessary for packaging and testing this device.

Due to the absence of flow-through structures, a micropipette was used to dispense samples onto the MPS regions. In doing this, undesirable electrical shorts were created when the dispensed sample traveled beyond the sensing region and made AC shunts between electrodes. Measurements taken with these devices demonstrated a barely discernible signal to noise, and the absolute need for a flow-through membrane.

The experience gained from this device certainly reaffirmed the necessity of a flow-through structure capable of precise sample delivery. Further design metrics to be considered were reduction of sample size and an electrode configuration which eases packaging. Forthcoming designs focused on this while facilitating smaller scaled flow-through structures.

## 5.4 Investigation of self-limiting electrochemical etching techniques

### 5.4.1 Self-limiting concept

A study to help fabricate flow-through structures was conducted where a self-limiting electrochemical etching technique was investigated. It was hypothesized that pore propagation would stop on a deletion region created by an applied voltage from the backside of the wafer during the electrochemical etching process. Figure 5.5 shows a schematic for the substrates used in this experimentation.

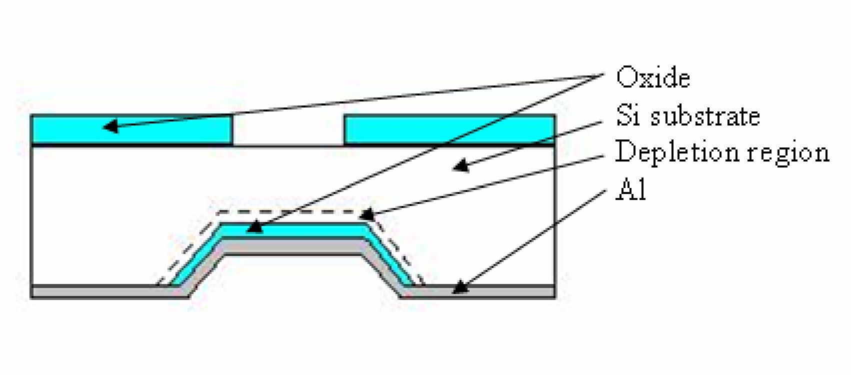

Figure 5.5. Cross-sectional schematic view of a substrate prepared for self-limiting electrochemical etching.

This design consists of a KOH-etched channel that is lined with oxide and Al on the backside of the Si wafer. During the electrochemical etching process, the applied voltage to this MOS structure creates a depletion region where the pores, requiring hole carriers to propagate, will stop. Figure 5.6 a) and b) are SEM images which show pore propagation stopping where a depletion region was created during the electrochemical etching process.

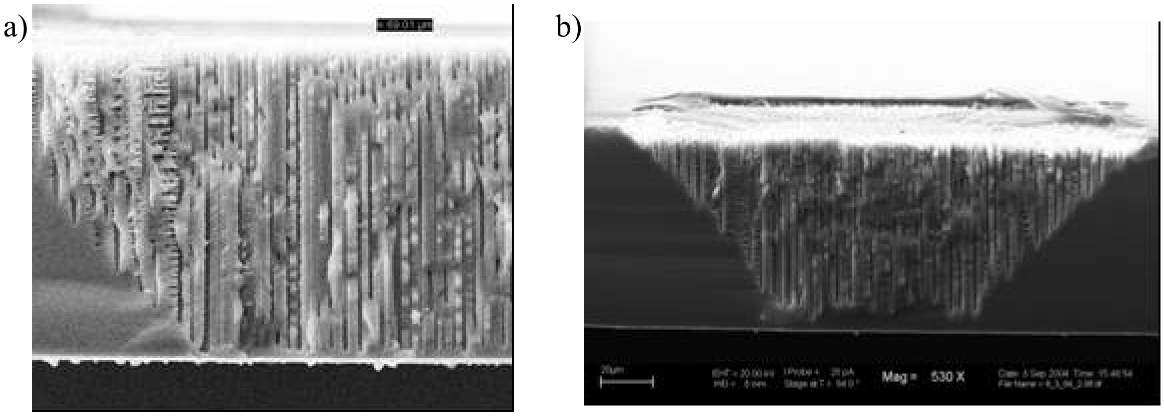

Figure 5.6. a) Cross-sectional SEM image of self-limiting MPS b) MPS formation stopped approximately 1 μm from the backside KOH etched channel.

### 5.4.2 Self-limiting electrochemical etching towards device fabrication

Once the concept of self-limiting electrochemical etching was proved, the technique was incorporated into a sensor fabrication scheme. The design of the device was strip-like measuring 1 by 2000 mm. Figure 5.7 shows a SEM cross-sectional image of the resulting interface between the MPS and KOH etched regions.

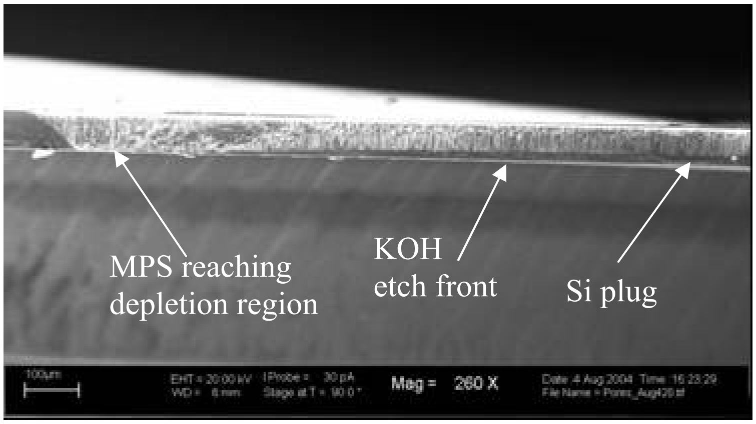

Figure 5.7. SEM image of self-limited MPS reaching the depletion region above a KOH etched groove.

As seen in Figure 5.7 pores located towards the center of the sensing region do not reach the depletion region. This can be attributed to outer pores creating a seal with the depletion region which prevents hole carriers in the bulk from reaching the pores in the center of the membrane. Referring back to the dissolution chemical reaction in Chemical Equation 2.2, it is known that hole carriers are necessary for the reaction to take place and pore propagation to occur. The rate of propagation of sealed off pores under this circumstance is believed to be greatly reduced or even stopped completely.

## 5.5 Realization of flow-through structures

### 5.5.1 Electrochemical and KOH etching

Fabrication techniques, such as intersecting a KOH etched groove into a PS region or propagating pores onto a KOH groove, for the case of the macrosquare design and self-limiting electrochemical etching, respectively, did not facilitate an acceptable flow-through structure. Difficulty in achieving a flow-through structure was in large part due to the curved profile located at the bottom of the MPS region. The curvature left a plug, as seen in Figure 5.7, when any planar etch encroached upon it. It was concluded that the curved profile of the MPS region requires an etch with a similar profile to eliminate the undesired plug and successfully create a flow-through structure.

By reducing the mask opening used during KOH etching, a smaller, more pointed etch front can be achieved as seen in Figure 5.8.

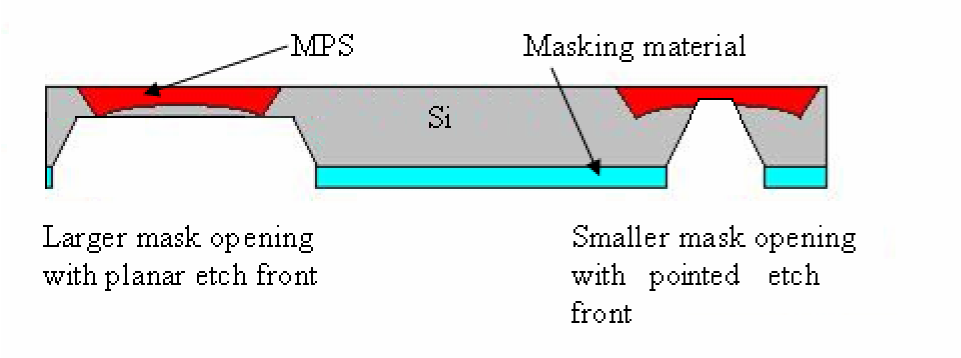

Figure 5.8. Schematic representation of KOH etched grooves. A smaller mask opening results in a more pointed groove which successfully intersects the MPS region.

The use of this etch technique eliminates the Si plug and successfully intersects the two regions for realization of a flow-through structure. The KOH etched groove which is now intersecting the MPS region can be used as a fluidic channel to transport analytes to specific sensing locations. This etching technique results in a self-aligned fluidic delivery system where the resulting fluidic channels inherently define the delivery location of samples into the MPS sensing region.

### 5.5.2 Macroporous silicon passivation

When the backside KOH etched channel intersects the MPS region, rapid etching of the material occurs. To protect the MPS region from this damage, an oxide-nitride liner is used to passivate the many exposed {111} planes. This allows Si etching into the MPS region while keeping the integrity of it. Figure 5.9 a) and b) shows oxide-nitride lining a MPS region that has been exposed to KOH etching.

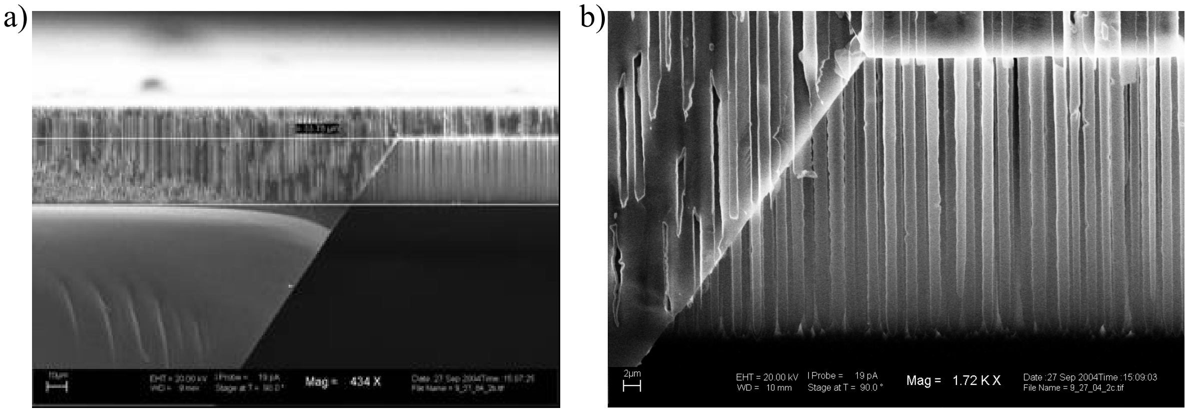

Figure 5.9. a) SEM cross-section of KOH etched groove intersecting the MPS region. b) Oxide-nitride lining the pores, seen as fading grey "needles", maintain the integrity of the PS region and remain intact as the KOH etch front intersects the PS region.

Once the KOH etch has intersected the MPS region, the passivating oxide-nitride liner can be removed and a complete flow-through structure is realized.

## 5.6 Concluding remarks

The importance of a flow-through structure is evident in this and upcoming chapters presented in this work. The self-aligned nature of this monolithic fabrication scheme is unique in that the fluidic channels on the backside of the device are fabricated and their position on the device directly defines the location of sample delivery. Typical fluidic systems are made on an entirely different substrate and must be aligned to the location of delivery.

Initial investigation of macrosquare devices and self-limiting electrochemical etching techniques was important because the study allowed for better understanding of MPS technology and its level of compatibility to various designs and fabrication schemes. The self-limiting electrochemical etching process is of special value because it provides a means for visual measurement of depletion regions in a semiconductor; something never done before.

The realization of the flow-through structure is by far the keystone of this device. Development took nearly nine months and involved several other investigations not mentioned in the body of this work. Once this structure was created, a fabrication scheme which integrated electrodes for a complete sensing device was developed into a robust process that has been consistently reproduced.

## Chapter 6

# Design and Fabrication of the Macroporous Silicon Flow-Through Sensing System

### 6.1 Device design

With experimental development resulting in successful fabrication of flow-through structures, focus was directed towards the design of a complete sensing system. Figure 6.1 shows a top-down schematic and cross-sectional view of a single sensor.

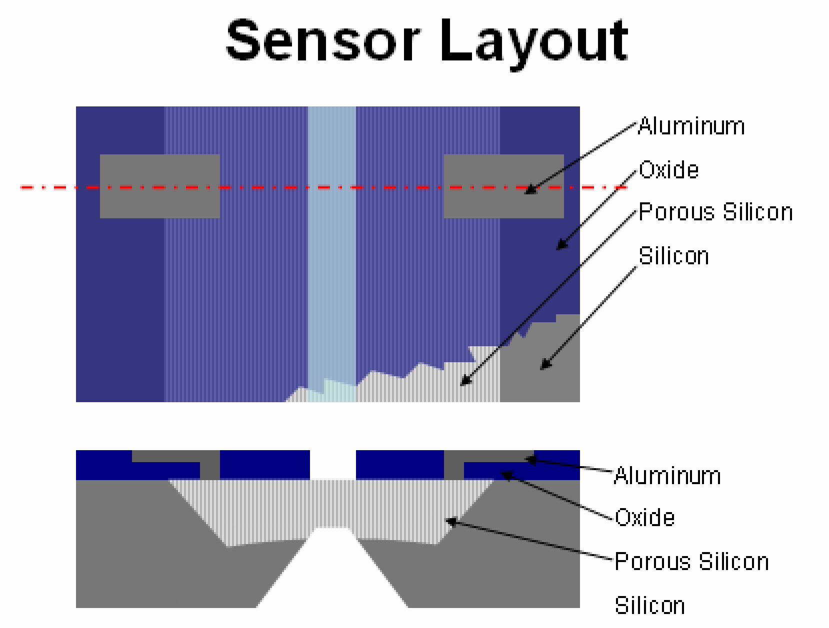

Figure 6.1. Device layout and cross-sectional schematic view of a single sensor.

The physical dimensions of the device are summarized in Table 6.1.

| Device Feature | Physical Dimension |
|---|---|
| Electrode | 1 mm x 3 mm |
| Contact Cut | 200 µm x 1 mm |
| PS Strip | 1 mm x 2 cm |
| Flow-through Region | 100 µm x 2 cm |
| Backside KOH Opening | 650 µm x 2 cm |

Table 6.1. Physical dimensions of device components.

Each chip consists of a 2 cm long, flow-through structure with four electrode pairs linearly arrayed along it. Electrode pairs define sensor locations by enabling electrical measurements of the MPS membrane located between them. The large electrode design is done in an effort to ease electrical testing of the device. Serving as a contact pad, electrical connection to the electrodes can be achieved by connecting wires to them with conductive epoxy, the use of a probe station, or even clamping wires to them.

### 6.1.1 Sensor arrays along fluidic channels

The length of the flow-through structure defined by the MPS and KOH masks is designed to create a backside fluidic channel that delivers a sample to four linearly arrayed devices positioned along it. Figure 6.2 a) and b) are fontside and backside images of four linearly arrayed sensors positioned along the backside fluidic channel.

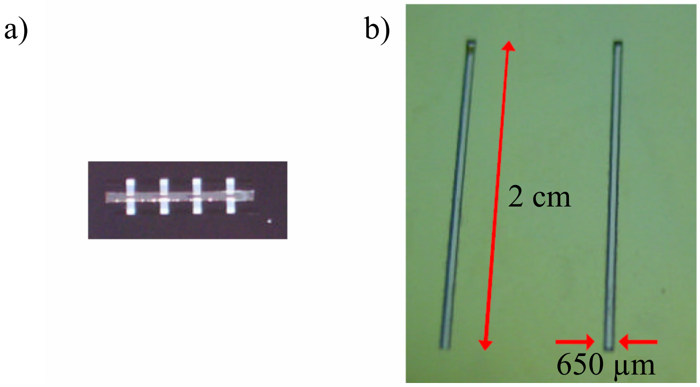

Table 6.2. a) Four linearly arrayed electrode pairs along an elongated flow-through structure. b) Two backside flow-through fluidic channels.

When the backside fluidic channel is filled with liquid, capillary action draws a portion of this into the MPS membrane. The four electrode pairs, evenly spaced along the frontside of the flow-through structure, define the sensing membrane regions. Figure 6.3 depicts a frontside and backside schematic of a substrate arrayed with eight elongated flow-through structures. The close-up view shows that each elongated flow-through structure has four electrode pairs positioned along it.

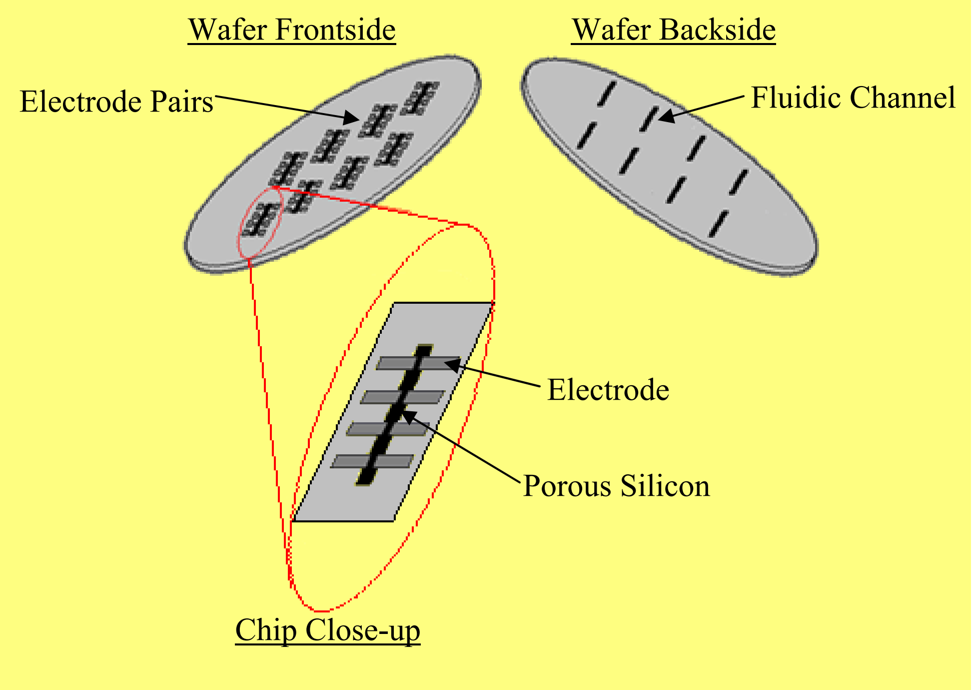

Figure 6.3. Schematic view of substrate with eight chips. Each chip consists of four sensors linearly arrayed on the frontside which is aligned to a fluidic channel on the backside.

### 6.1.2 Discussion of device scaling

If this device, utilizing the flow-through structure, were to be scaled, it is expected that the physical limiting factors would be the process of MPS formation and KOH etching. Undercutting of the mask during the electrochemical etching process, as mentioned in Section 2.3.5, leads to larger than desired MPS regions. It is estimated for a

50 μm deep MPS region, the minimum width possible is about 150 μm. At the expense of sensitivity, shallower pores can be used. This results in less undercutting and much smaller MPS regions.

For a substrate that is 525 μm thick, a backside mask opening of 650 μm is used to bisect the KOH etched groove into the MPS region. The required backside mask opening is a function of substrate thickness and MPS depth. Typically, the deepest MPS region achieved is on the order of 60 μm, thus a large portion of the KOH etch is exhausted on traveling through the bulk of the substrate. One solution to this scaling issue is to use a substrate with a thickness less that 525 μm. In doing this, the required mask opening for KOH etching would be much smaller and scaled devices can be achieved at a cost of signal-to-noise.

## 6.2 Fabrication considerations of macroporous silicon

Development efforts discussed in Chapter 5 have led to a fabrication process capable of producing flow-through structures. This process has been further developed into a fabrication scheme capable of realizing complete sensing systems. Of all the processing steps, the electrochemical and KOH etch, which form the flow-through structure through the bulk of the substrate, are the most critical.

The use of MPS dictates limitations on further processing capabilities. Based on this work, four key considerations are identified when using MPS: (1) thermal oxidation of MPS material, (2) exposure of MPS to chemical etching, (3) photolithography over MPS regions, and (4) vacuum wafer handling of substrates with MPS flow-through structures.

### 6.2.1 Thermal oxidation

Mechanical strain present in thermally oxidized films of c-Si induces stress upon Si substrates. If stress upon the wafer becomes too great, undesirable deformation of highly planar substrates can occur. Thermally grown oxides on the (100) crystalline plane of a Si lattice contribute less stress upon a wafer than that of oxide grown as a pore lining on the {001} and {010} planes. Mechanical stress from thermally grown oxides lining a pore wall is a result of volume expansion which is dimensionally confined in the pore [57]. In contrast to thermal oxidation on a planar surface, the large surface area and three-dimensional nature of MPS allows for increased thermal oxide density which contributes to higher than normal wafer stress per unit volume across c-Si substrates. This has been demonstrated through visible marks on device substrates during the fabrication process resulting from slipped Si crystal planes.

### 6.2.2 Chemical etching

A pore traveling though the bulk of a (100) Si wafer passes through and exposes many (111) c-Si planes. Potassium Hydroxide (KOH), which readily etches to reveal (111) planes, can undesirably etch and destroy MPS material in a very rapid fashion. Thus, a passivation scheme is necessary to achieve sufficient protection of MPS during KOH etching. This work utilizes a passivation scheme based on thermally grown silicon dioxide ($SiO_2$) and/or silicon nitride ($Si_3N_4$). In using these thin films, conformal coverage of the pore walls is achieved. High etch selectivity between Si and $SiO_2$ and $Si_3N_4$ with KOH supports $SiO_2$ and $Si_3N_4$ as prime candidates for MPS passivation. Figures 6.4 a) and b) are images of oxidized MPS free standing membranes.

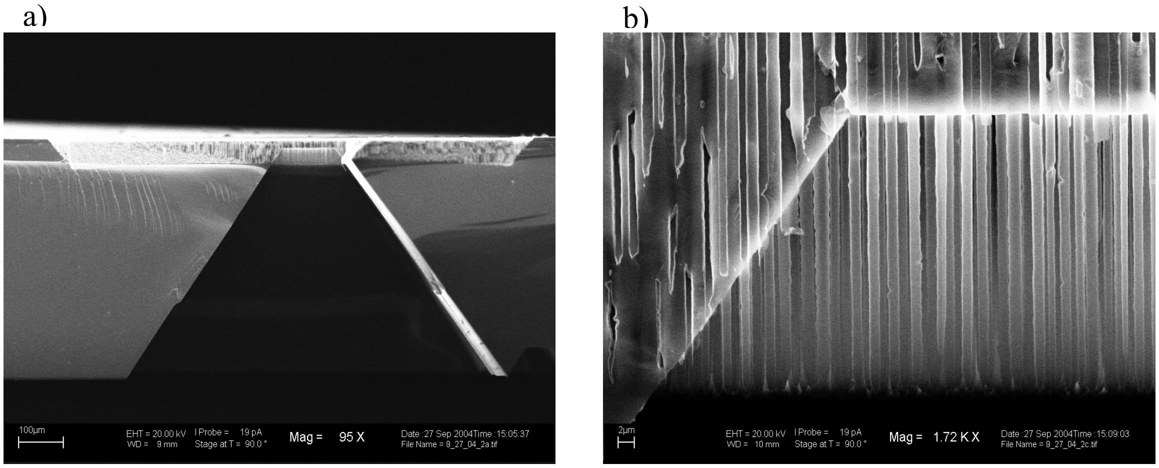

Figure 6.4. a) SEM cross-sectional view of a flow-through structure where a KOH etch grove encroaches upon a MPS region. b) Remnants of $SiO_2$ liners seen as light colored, needle-like structures.

### 6.2.3 Photolithography

Once a Si substrate has been anodized, the resulting surface of the MPS material is roughened by the many holes which propagate downward as seen in Figure 6.5.

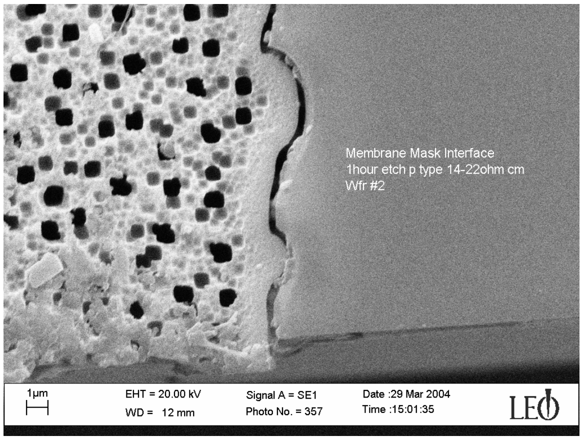

Figure 6.5. Top-down view of MPS with no pre-structured surface patterning. Pore openings represented as dark squares with rounded corners.

Standard liquid photoresist coatings are more difficult to attain and require special attention. Any heating of the substrate, such as a soft bake, can cause a reflow of photoresist into pore openings and result in non-uniform coatings in MPS regions. Such a compromise in coating uniformity leads to insufficient masking which is vital for successful execution of subsequent processes.

### 6.2.4 Substrate handling

A final material consideration of MPS is tool handling via means of vacuum. The flow-through structure is a fluidic interconnect that allows any fluid, gas or liquid, to pass through the substrate. If a vacuum hand of a process tool grasps the substrate arrayed with such interconnects, a compromise in pressure differential between the wafer and robot arm can exist. Complete loss of vacuum to a substrate is likely and this can result in a substrate falling off of a robot arm and sustaining damage.

## 6.3 Process integration of electrodes

Integrating electrodes onto the MPS region was the largest challenge in developing the flow-through structure into a complete sensing device. In order to have electrical contact to the MPS sensing membrane, contact cuts are made through the oxide into the MPS region. The photolithography process for this is non-conventional because it is performed on the rough surface of MPS. Part B of the appendix explains process details for this photolithographic procedure.

### 6.3.1 Basic integration scheme

This basic integration scheme is most commonly used for device fabrication. It provides a means for simplistic fabrication of fully functional devices with greatly reduced fabrication time. The method consists of a thermally grown oxide, on the order of 500 Å, as a lining in the MPS sensing membrane. Contact cuts are made into the oxide, and aluminum is sputtered and pattered over this surface. Figure 6.6 shows a cross-sectional schematic of this isolation scheme.

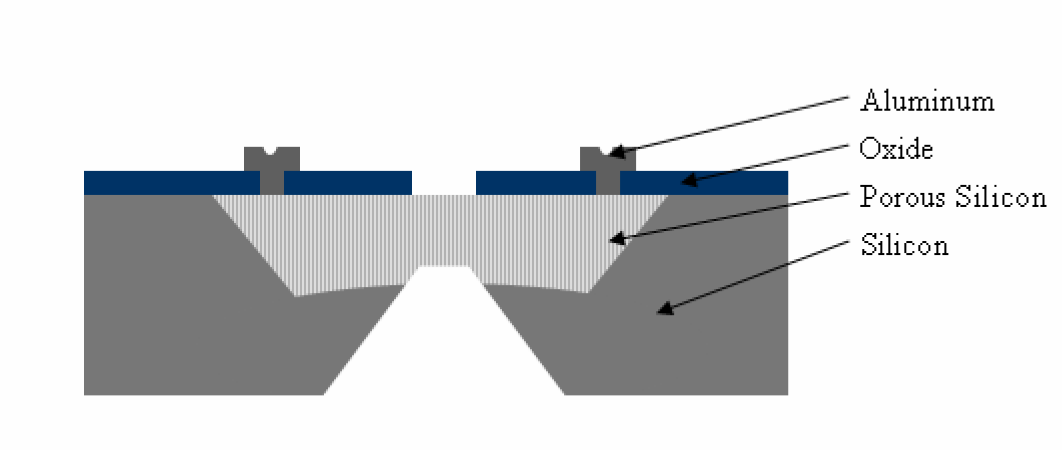

Figure 6.6. Cross-sectional schematic of a flow-through structure integrated with the basic electrode isolation scheme.

This design reduces parasitic pathways during electrical measurement by isolating the electrode from one another with a layer of oxide. Contact between the MPS region and the electrodes promote measurements, to be taken across the sensing membrane. One consideration of this electrode isolation scheme is the potential for a liquid sample to overflow the sensing membrane, collect on the surface in between the electrodes, and establish a short circuit path during electrical measurements. Although this has never been observed, the potential is there and a better, more complicated isolation scheme was developed.

### 6.3.2 Advanced integration scheme

The advanced isolation scheme follows the process of the basic scheme with the addition of 1um LPCVD oxide over the electrodes, and two more photolithography steps to define the via and flow-through regions. Figure 6.7 shows a schematic cross-sectional view of this more advanced electrode scheme.

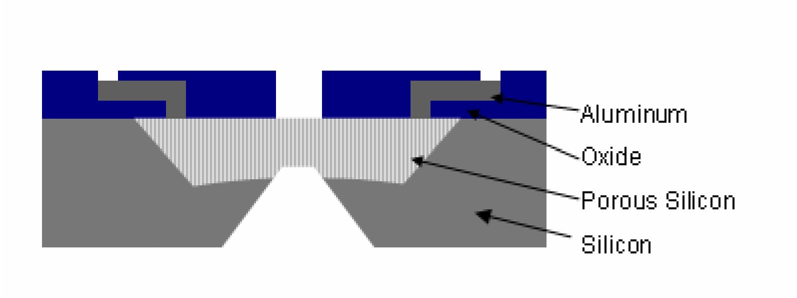

Figure 6.7. Cross-sectional schematic of flow-through structure integrated with the advanced electrode isolation scheme.

The addition of two photolithography steps greatly increases the amount of time needed to fabricate this device. Although the advanced scheme does provide better protection against a liquid sample from shorting out the electrodes, it was not commonly employed. Liquid induced shorts between electrodes have not been a problem and this process was merely done as an exploratory exercise.

### 6.3.3 Investigation of a tetraethylorthosilicate oxide capping layer

It was thought that plasma enhanced chemical vapor deposited (PECVD) oxide using tetraethylorthosilicate (TEOS) could provide rapid deposition of oxide films over MPS regions. This in turn could be used as a replacement for the 1 μm LPCVD oxide in the advanced isolation scheme and a reduction in fabrication time would be experienced. Several substrates were used in a study to investigate the use of TEOS films for advanced isolation of electrodes.

Thickness measurements taken in the field region of a substrate after the deposition suggested a uniform oxide-like film across the surface. When attempting to etch the TEOS film in HF there was no sign of film removal. To investigate this, several samples were prepared and underwent SEM imaging. Figure 6.8 is an image depicting ball-like clusters of the TEOS generated material, which occurs only over the MPS region.

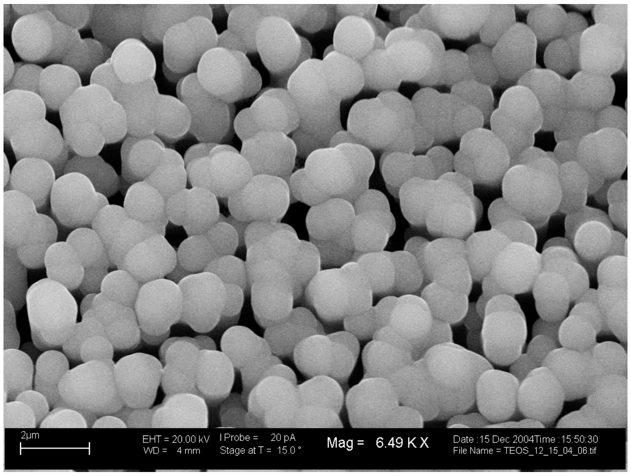

Figure 6.8. Top-down SEM image of PECVD TEOS ball-like structures. This material is not oxide-like and did not etch in HF.

Although the field regions suggest a uniform oxide-like film, further investigation proved the material is not uniform or oxide-like. It is believed that electromagnetic fields which are locally perturbed by the unique topography of the MPS regions resulted in the undesirable deposition of this material.

## 6.4 Fabrication overview

Device fabrication is focused on integrating the MPS material into a process based on standard IC and MEMS fabrication technologies. As seen in part C of the appendix, the entire fabrication scheme consists of four levels of photolithography and 49 fabrication steps. Evaluation of processes is conducted with optical microscopes, optical spectroscopy, ellipsometery, profilometery, four-point probe measurements, scanning electron microscopy, and electrical testing.

Emulsion masks with the Karl Suss MA150 contact mask aligner are utilized for the required photolithographic fabrication steps. Emulsion masks, as seen in Figure 6.9, are flexible polymer sheets and can be used to resolve critical dimensions (CDs) on the order of tens of microns. For the scope of this work, device CDs fall into this range and it is therefore desired to use this technology. The masks are designed with Adobe Illustrator and a Dolev imagesetter is used to develop the emulsion masks.

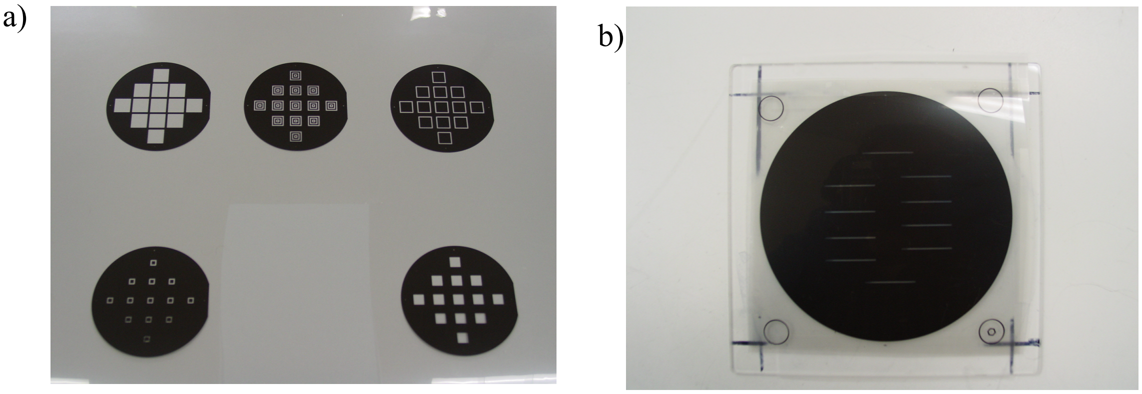

Figure 6.9. a) Emulsion print consisting of several masks which are subsequently cut and mounted to quartz plates. b) An emulsion mask mounted to a 5” quartz plate.

Cost of emulsion masks are two dollars for approximately 30 masks with an estimated fabrication time of one day. The use of this technology allows for rapid design experimentation and iteration with low project expense. Emulsion masks are mounted to a 5 inch quartz plate. These plates are identical to those which are used in making standard chrome masks and can readily load into any mask aligner or stepper. This technique is especially advantageous when backside alignment is necessary. The clear nature of the masking plates, and the ability to sandwich a substrate between them, provides flexibility in performing front-to-backside alignment.

To date, hundreds of sensors have been successfully fabricated using the process developed in this work. Three lots have been processed from January to May of 2005 with a chip yield estimated at 90%. Each chip consists of four sensors along a fluidic channel. A yielding chip is defined as having at least one sensor along the channel able to perform standard sensing operations. Of the four sensors along the channel, the outermost sites experience better yields than the middle positions. This is due to the curved profile of the MPS that spans the length the fluidic channel. During the KOH etch the outer devices are located over a region of the MPS that is intersected first, as seen in Figure 6.10.

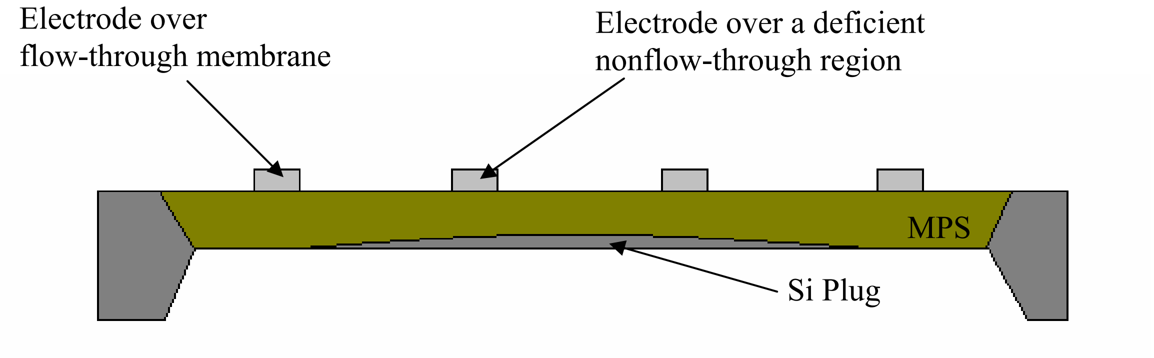

Figure 6.10. Cross-sectional schematic of four linearly arrayed sensors positioned along a elongated flow-through structure. A backside fluidic channel formed by KOH etching has yielded two working flow-through sensors. The inner two devices are deficient because the KOH etch has not completely intersected the MPS region to form flow-through membranes.

As etching continues into and towards the MPS region, the inner devices with slightly shorter pores are subsequently intersected. In some cases the substrates are removed from the KOH etching process before the middle sensors have a channel intersecting the MPS region. These deficient sensors as seen in Figure 6.11 do not have a flow-through membrane and are unable to draw samples from the fluidic reservoir.

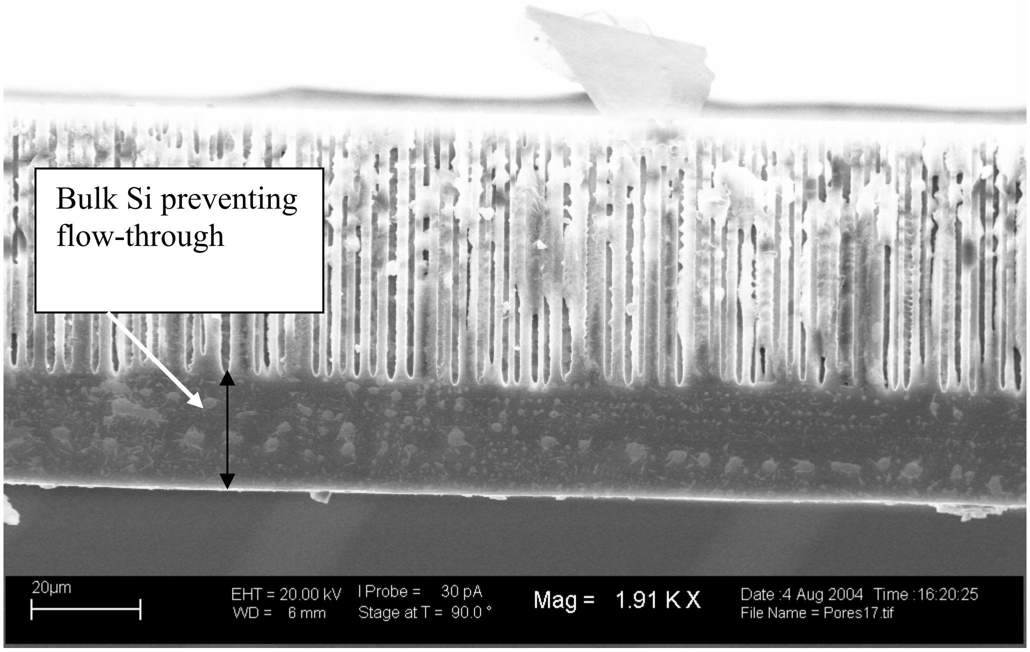

Figure 6.11. SEM image of a KOH etched channel that is not intersecting the MPS region. Approximately 20 µm of bulk Si separate the fluidic channel from the MPS region.

## 6.5 Concluding remarks

A successful design and fabrication scheme has integrated MPS flow-through structures with electrodes to realize a functional sensing system. The design consists of four electrode pairs which are linearly arrayed on the frontside of an elongated flow-through structure. Electrode pairs define where the sensors are by establishing electrical contact to the free standing MPS membrane which draws fluid from the backside KOH etched channel.

A study was conducted to investigate various electrode isolation schemes. The investigation included different designs and materials which were implemented into the fabrication of the device. It was concluded that a basic isolation scheme consisting of contact cuts into an oxide film provided an acceptable level of isolation between electrodes.

This device has the potential for more complex sensing arrays capable of performing multiple sensing tasks. A more sophisticated system could have an array of individual sensors interfaced with a fluidic system to deliver samples to each sensing membrane in the array. Chapter 8 will discuss fluidic systems capable of this and various efforts made in this area.

## Chapter 7

# Characterization as a Chemical and Biological Sensor

## 7.1 Electrical test setup

In order to better understand and experimentally quantify the capabilities of the sensor, a test-bed specific to microfluidic devices was created. Materials used for this test setup include tubing, syringes, pipettes, a desiccator, and control software. Initial characterization of the sensing device was achieved by investigating its response to ambient conditions such as light, temperature, and relative humidity. Influence of ambient conditions on the device is important to understand because error in sensing targeted analytes may occur if the condition is prevalent and unaccounted for. Overall functionality of the device was demonstrated by characterizing the device's ability to repeat, reproduce, and discriminate between analytes. Lastly, application of the sensor to various areas of science and technology was examined by performing sensing operations in monitoring air and water quality monitoring, and detection of binding events between proteins.

### 7.1.1 Instruments and software

A computer is networked with a HP 4275A multifrequency LCR meter and LabVIEW software is used to collect real-time sensing data as measurements of the sensor occur. Figure 7.1 shows the electrical test-bed used for capacitive measurements of this device.

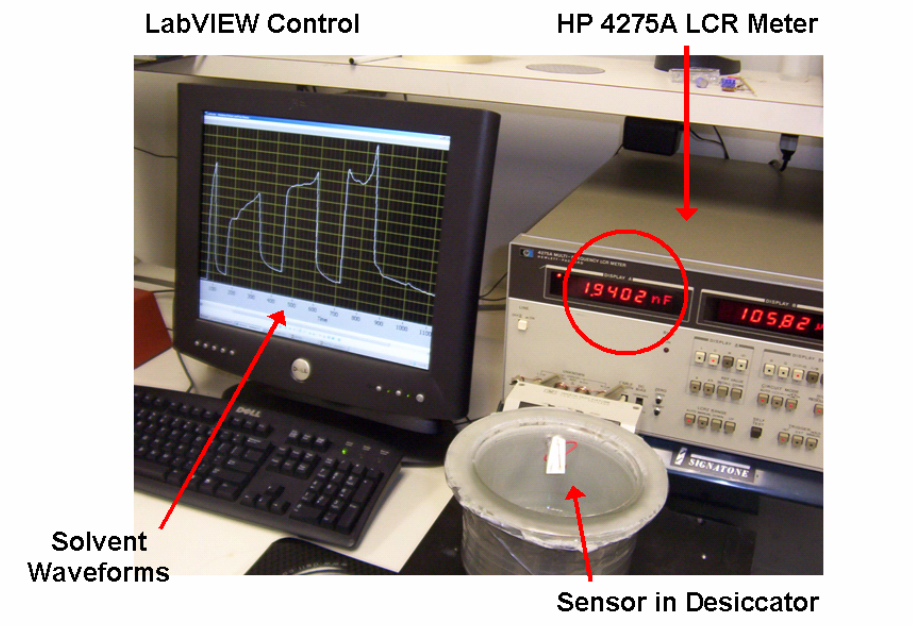

Figure 7.1. Electrical test setup used for characterizing sensor operation. A computer, seen on the left, is interfaced and used to control the HP 4275A LCR meter, as seen on the right.

Upon powering the LCR meter, various self-checks and tests on the machine are run by the user. Once passed, a final calibration of the meter is done by running an open circuit zeroing program. LabVIEW software is used to save preset information and assure that all parameters are adjusted to predetermined conditions before sensor testing begins. To verify that the meter is in working order and all tests and calibration programs were successful, a standard 22 uF capacitor is measured. If this measurement falls within the designated tolerance of the capacitor, the meter is ready for electrical testing of sensing devices.

The functionality of the HP 4275A was further verified when devices were measured on a different LCR meter at another location. The capacitive measurements yielded almost identical values. All measurements taken in this work are completed in a parallel capacitive mode with an AC signal of 10 kHz, and an oscillation voltage amplitude of 60 mV.

A program in LabVIEW was written which enables the user to adjust various analysis parameters of the HP 4275A such as AC frequency and oscillation voltage.

Figure 7.2 shows the graphical user interface (GUI) created for taking real-time capacitance measurements of sensors.

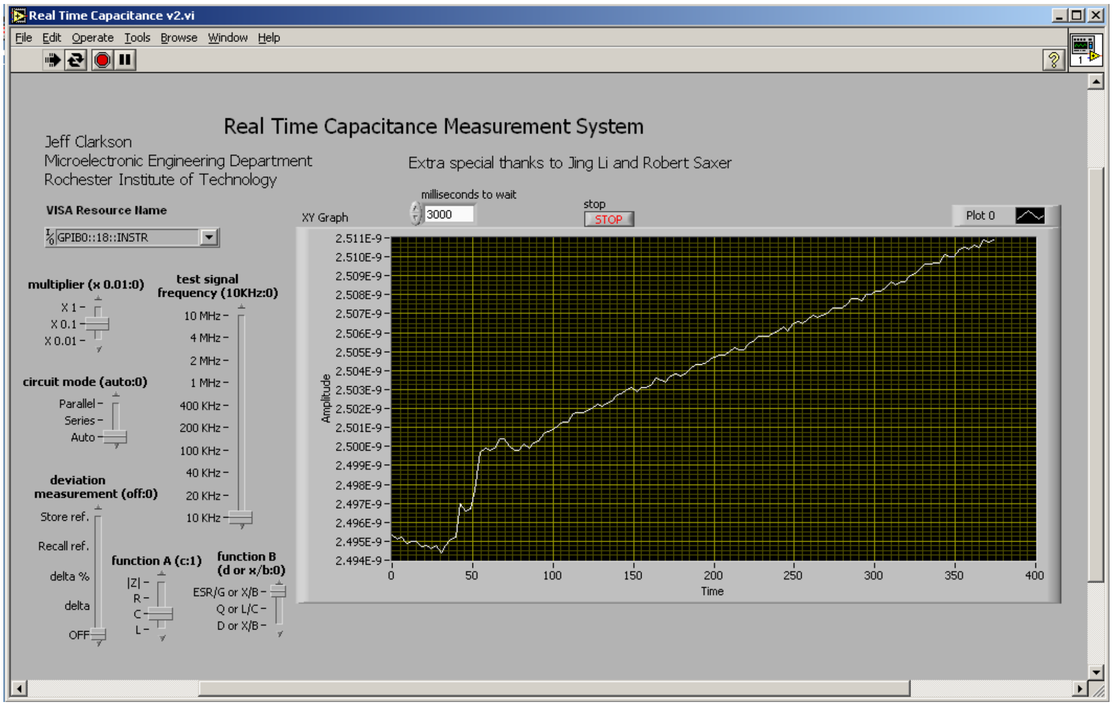

VISA Resource Name: GPIB0::18::INSTR

milliseconds to wait: 3000

Figure 7.2 Computer interface created with LabVIEW software which allows adjustment of measurement parameters and collection of real-time measured capacitance with a HP 4275A multifrequency LCR meter.

Measurements are collected approximately every 3 sec and are displayed in a graph which could be saved as an image for later use. Raw data pairs are also saved as a text file and can be imported into a spreadsheet program such as Microsoft Excel for further analysis.

### 7.1.2 Desiccator

A chamber is necessary to establish unique ambient conditions that are otherwise not possible. Most commonly, the chamber is used to contain vapor phase tests that pose flammable or health related dangers. The chamber, as seen in Figure 7.3, has a volume of 1525 ml and consists of a glass base and airtight lid.

Figure 7.3. A glass desiccator with the lid removed which is used to house sensing devices during vapor phase testing. Clamps are used to contact wires to the device electrodes as seen inside the desiccator.

Three holes were drilled into the side of the chamber for establishing electrical contact to the device inside and to introduce or exhaust any desired gases to/from the chamber. Strips of duct tape completely cover the desiccator in a layered fashion to eliminate any light from entering the chamber.

## 7.2 Detection of ambient conditions

Due to the inherent nature of semiconducting materials, this Si based sensor is sensitive to ambient conditions such as light, temperature, and humidity. It is important to understand the effect these factors may have during device operation. The level of sensitivity this device exhibits to these variable conditions is low. This is important because if the sensitivity was high, the magnitude of electrical response from the detection of chemical and biological materials would be dominated by that of undesirable noise contributed from ambient conditions. All chemical and biological measurements were considered the dominating capacitive response of the sensor unless otherwise stated. If room temperature, humidity, or lighting changed drastically, these contributions to the measured capacitance taken from the sensor during analyte detection would need to be considered.

### 7.2.1 Light

Energy in photons impinging upon the Si MPS sensing membrane generate electron-hole pairs. These excess carriers contribute to the overall conductivity of the semiconducting material which in turn modulates the capacitance measured across the membrane. Figure 7.4 shows the measured capacitance across a sensing membrane as lights in the laboratory are turned on and off.

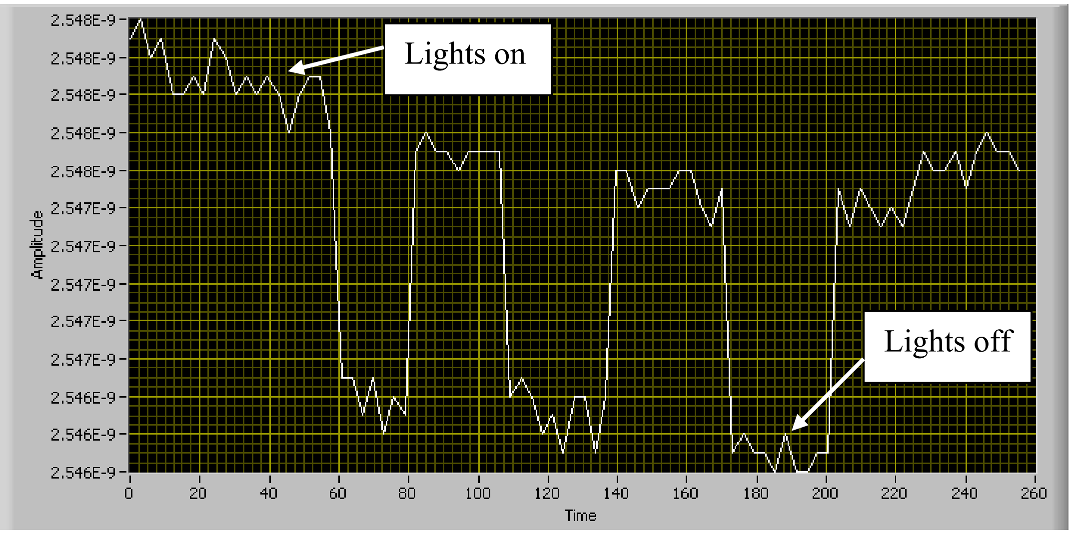

Figure 7.4. A change in capacitance resulting from room lights turning on and off. The capacitance decreases approximately 2 pF once the lights are turned off.

As seen from the graph, room lights can be attributed to a capacitive modulation of approximately 2 pF. The magnitude of capacitive response to light is insignificant during liquid phase detection of chemicals where the signals typically vary on the order of nF. However, during vapor phase detection on an order of < 1 ppm it is important to eliminate any light-induced capacitive change as this could be a contributing factor during the measurement which takes place on the scale of several pF. To eliminate the effects of room light on the sensor, all vapor phase tests are conducted in a desiccator which is shielded from light.

### 7.2.2 Temperature

During the winter months, this device was used to detect solvent vapors over a long period of time. It was found that during constant vapor concentrations, where the capacitive signal is expected to be constant, the measured capacitance modulated unexpectedly. To investigate the influence room temperature had on this condition a standard test capacitor was placed in the laboratory, and capacitive measurements were taken overnight. Figure 7.5 shows data collected on two different nights.

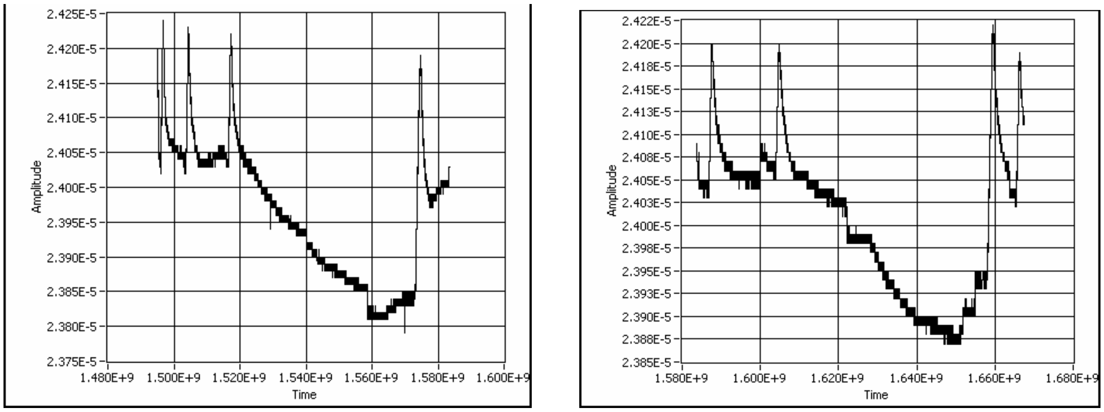

Figure 7.5. Capacitive measurements taken during two different nighttime periods on a test capacitor. Building heating and cooling can be seen with increases and decreases in measured capacitance.

The data show almost identical changes in capacitance with respect to time. The largest increase in capacitance measured with the device always occurred at 7:30AM.

Investigation of the buildings heating system revealed that at this time the building's heaters were programmed to turn on and heat the building for incoming faculty and students. It was concluded that initial spikes in the measured capacitance were the heaters turning on in an effort to maintain a daytime temperature of approximately 68° F. As nighttime approached, the building temperature was set to a lower temperature level, as seen as the largest drop in measured capacitance.

The range of daytime temperatures in the laboratory is small and the measure capacitive change from this is insignificant to the overall operation of the device. If, however, low level measurements of vapor phase solvents are taken overnight, it is important to consider any large change in temperature that may occur.

### 7.2.3 Relative humidity

The first electrical response recorded with this device was from human breath. Much like one would exhale to create fog onto a window, this type of breathing was directed towards the sensor. Moisture condensed onto the sensing membrane and a capacitive modulation resulted as seen in Figure 7.6.

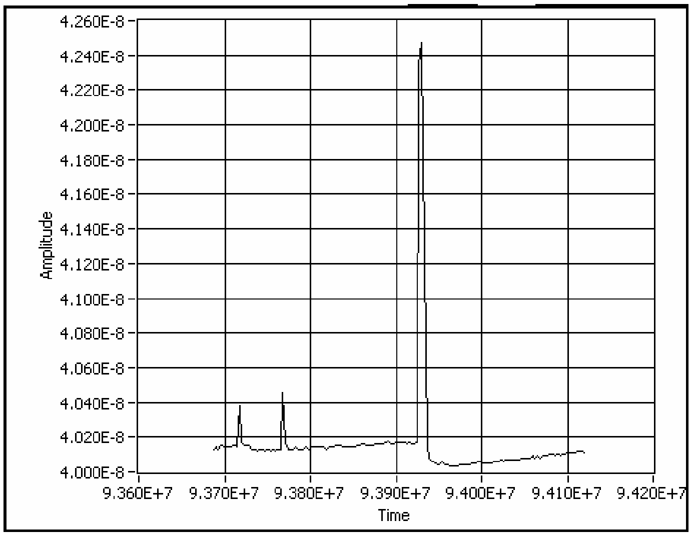

Figure 7.6. Capacitive measurements of a sensing device receiving two small and then one large human breath containing moisture which was visually seen condensing on the sensor during the time of measurement.

The first two peaks resulted from light breaths and then a final harder breath with more moisture caused the largest capacitive response. Breathing on the sensor generates a change in humidity that is unlike any typical laboratory condition. The relative humidity of the ambient during device testing is assumed stable and error from this is considered insignificant.

## 7.3 Chemical sensing

Fabricated sensors can be used to detect many chemical materials in their liquid and vapor phase. Various solvents such as acetone, ethanol, isopropyl alcohol (IPA), methanol, and toluene were selected for testing in this work. These chemicals were chosen because they are readily available, pose minor safety concerns, and rapidly evaporate. Sensing devices were used first to perform identification of these various solvents in their liquid phase and then, second, to detect specific concentration levels in vapor phase.

### 7.3.1 Liquid phase solvent detection

Wire connections were established to the electrodes of the sensing device with Chemtronics, Circuitworks CW 2400 conductive epoxy. Once cured, the sensor was connected to the HP 4275 LCR meter with the backside fluidic channel facing up. Collection of real-time capacitance across the sensing membrane began and a pipette was used to dispense approximately 33 μl of solvent into the backside channel. The solvent immediately filled the channel and an instantaneous increase in capacitance occurred. Data collection continued until the measured capacitance returned to an initial baseline value which signified that the solvent had completely evaporated out of the sensing membrane.

Successive iterations of exposure to liquid phase solvents were conducted to investigate the behavior of a device which was repeatedly exposed to a solvent over a period of time. Acetone and IPA were exposed 100 times to separate sensors over the course of 9 days. Figure 7.7 shows 10 repeated exposures to acetone taken on the 9th day.

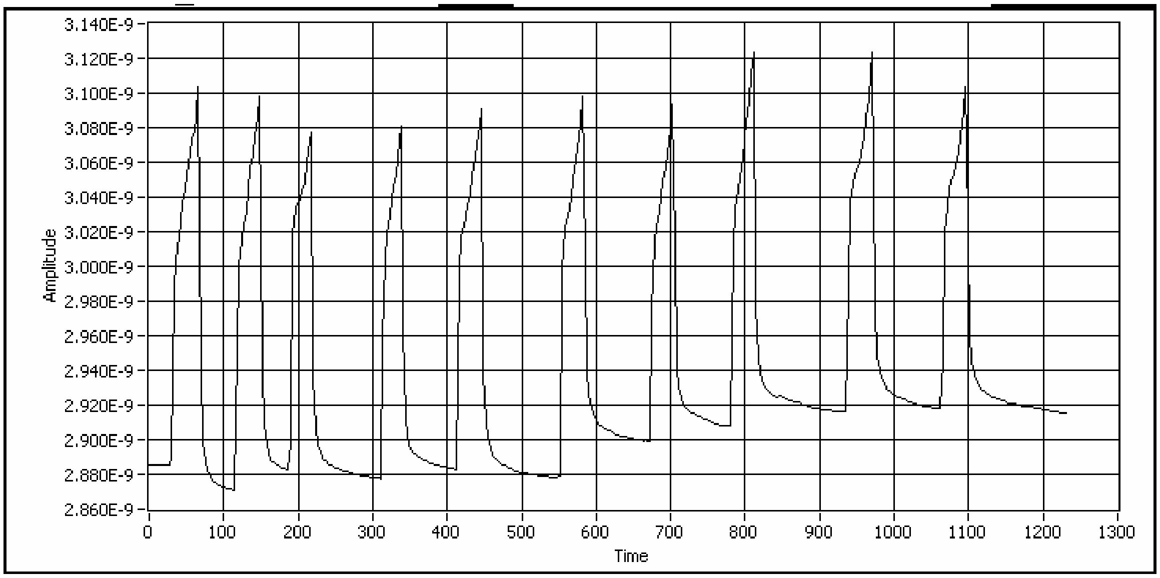

Figure 7.7. Capacitive measurements taken with a sensor exposed to samples of acetone. Each peak represents one delivery for a total of ten deliveries.

The graph contains 10 spikes in capacitance, each representing the introduction and complete evaporization of an acetone sample. The average change in capacitance during exposure to acetone is 0.207 nF with a standard deviation of 0.016 nF. The variation in signal strength and duration is directly related to variation in drop size from the pipette. Figure 7.8 demonstrates this by showing the capacitive response from a large and small sample size.

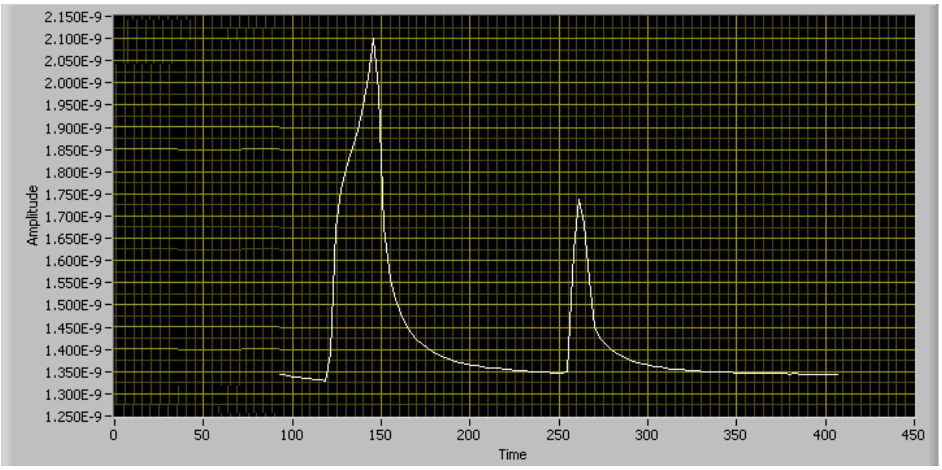

Figure 7.8. Different measured capacitive signals for different sample sizes of acetone. The large and small peaks result from 10 and 4 µl sample volumes.

As the sample volume increases, change in capacitance and signal duration increase. At the time of testing, effort was made to drop similar sample volumes into the same position along backside channels. To eliminate inconsistencies in analyte delivery a micropipette could be used. Utilization of this tool would allow adjustable control over the sample size and ensure identical samples are being delivered to the device every time.

Figure 7.7 also poses an interesting phenomenon. Once the sample has been sensed by the device, the final baseline capacitance which the sensor returns to is slightly different from that of the last. For the case of acetone, the baseline capacitance typically increases over successive exposure to samples.

The most dramatic shifts in baseline capacitance are seen with IPA. Figure 7.9 shows typical real-time capacitance measurements taken during 10 successive IPA deliveries.

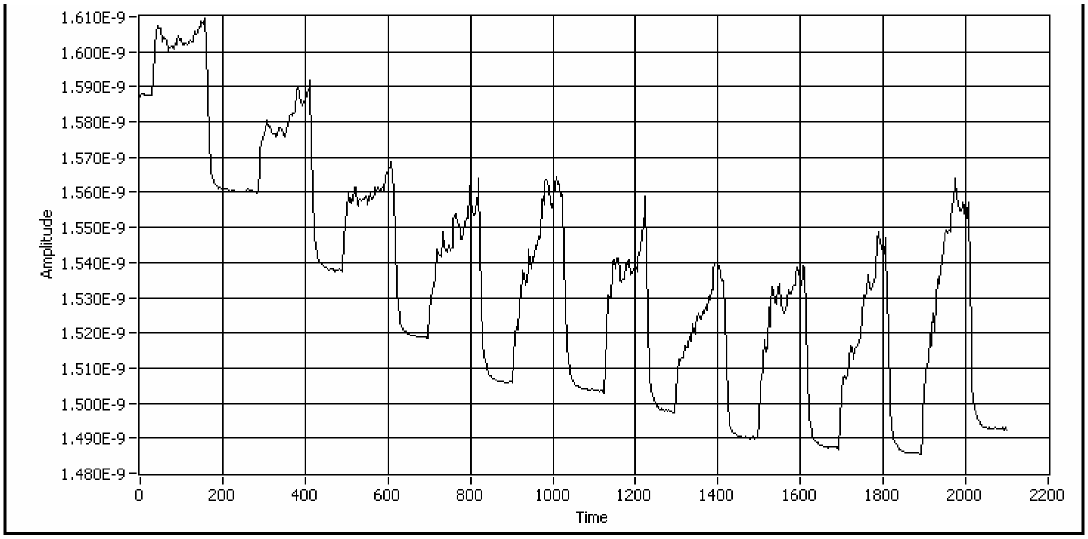

Figure 7.9. Successive deliveries of IPA to a sensor. As samples are delivered to the device a change in baseline capacitance occurs and finally levels off to a consistent value.

In this case the baseline capacitance decreases and flattens out to a fairly repeatable value of approximately 1.49 nF. The variation in baseline capacitance for chemical sensors has been routinely observed and is not well understood [58]. The average change in capacitance for the 10 sample introductions is 0.057 nF with a standard deviation of 0.005 nF. When comparing these tests, the signal from IPA results in a smaller change in capacitance and is more consistent than that of acetone. Table 7.1 shows average and standard deviation values for similar 10 delivery tests of acetone, ethanol, IPA, and methanol.

| Solvent | Average Capacitive Change (nF) | Standard Deviation (nF) |
|---|---|---|
| Acetone | 0.207 | 0.016 |
| Ethanol | 0.194 | 0.009 |
| IPA | 0.057 | 0.005 |
| Methanol | 0.216 | 0.017 |

Table 7.1. Average measured change in capacitance and standard deviation taken over ten deliveries for various solvents.

Although one sensor is capable of detecting all the solvents above in Table 7.1 each solvent was detected with a separate device. It is important to note this because MPS formation across a Si substrate is not uniform and this leads to minor variations in the size of the sensing membrane which ultimately can affect the average capacitive change.

The next study investigated the sensors ability to discriminate between different solvents. Figure 7.10 shows acetone, ethanol, IPA, methanol, and toluene detected by the same sensor.

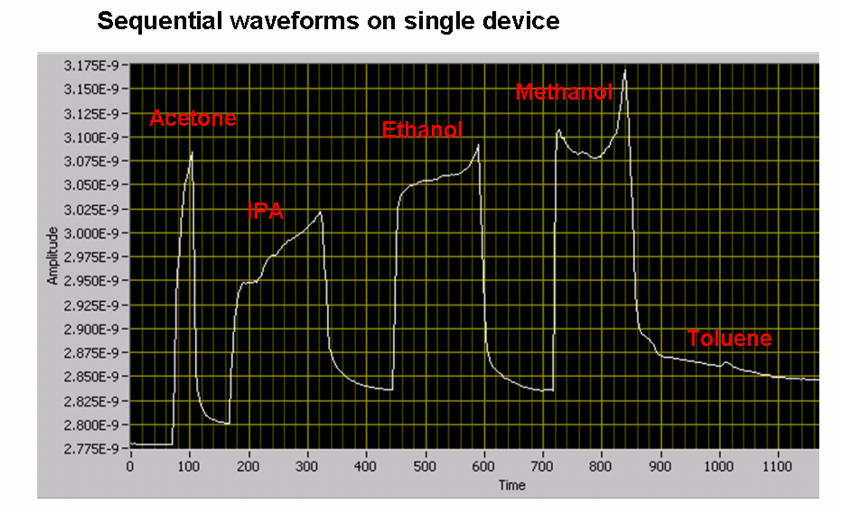

Figure 7.10. Capacitive measurements taken with a sensor exposed to acetone, IPA, ethanol, methanol, and toluene. Each solvent produces a unique capacitive signal which can be used for identification and discrimination.

This test was conducted by placing a 0.33 µl sample into the backside channel and allowing it to completely evaporate before the next sample was delivered. In order from left to right, the four obvious peaks are acetone, IPA, ethanol, and methanol with a final less obvious hump indicating toluene. This test demonstrates that a single device is capable of discerning these five solvents. It is important to note that toluene was tested last because it permanently desensitizes sensors and rendered them useless in most cases.

It is believed that this degradation is caused by permanent modification of the oxide liner within the MPS where interactions between the fluid and semiconductor, as described in Chapter 3, are greatly hindered. This is indication that capacitive measurements are not detecting explicitly the presence of a liquid in the membrane, rather the modulation of the space charge from a given liquid interfaced with the semiconductor.

The change in capacitance for acetone, ethanol, IPA, and methanol are 0.300, 0.250, 0.225, and 0.305 nF respectively. These capacitance values are not identical with that of Table 7.1. As mentioned before, this is a result of differences in sensing membrane size. It is important however to note that the largest peak experienced in each sensor was created by methanol. Additionally, the rank of peak size correlates between sensors with the order of size from largest to smallest being methanol, acetone, ethanol, and IPA.

By investigating the physical properties of the various solvents, information pertaining to the characteristic capacitive response in the sensor can be found. Table 7.2 displays important physical properties of each solvent.

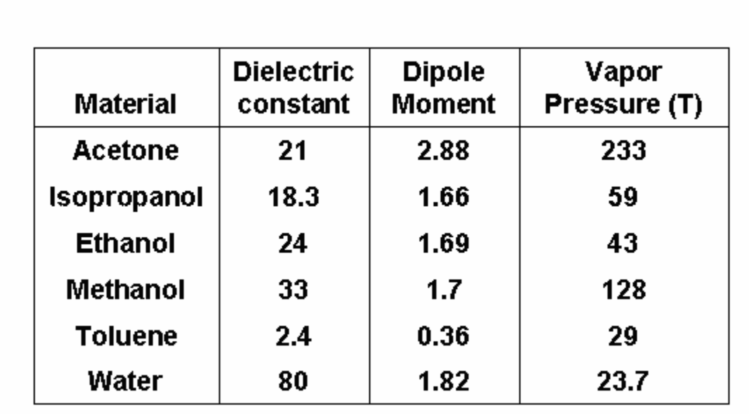

| Material | Dielectric constant | Dipole Moment | Vapor Pressure (T) |
|---|---|---|---|
| Acetone | 21 | 2.88 | 233 |
| Isopropanol | 18.3 | 1.66 | 59 |
| Ethanol | 24 | 1.69 | 43 |
| Methanol | 33 | 1.7 | 128 |
| Toluene | 2.4 | 0.36 | 29 |
| Water | 80 | 1.82 | 23.7 |

Table 7.2 Physical properties of various solvents used during device characterization.

The vapor pressure of each solvent provides unique information pertaining to the duration of capacitive signals exhibited by the solvents. The duration of each signal is easily analyzed by overlaying the normalized signals as seen in Figure 7.11 and comparing these to the vapor pressure of each solvent in Table 7.2.

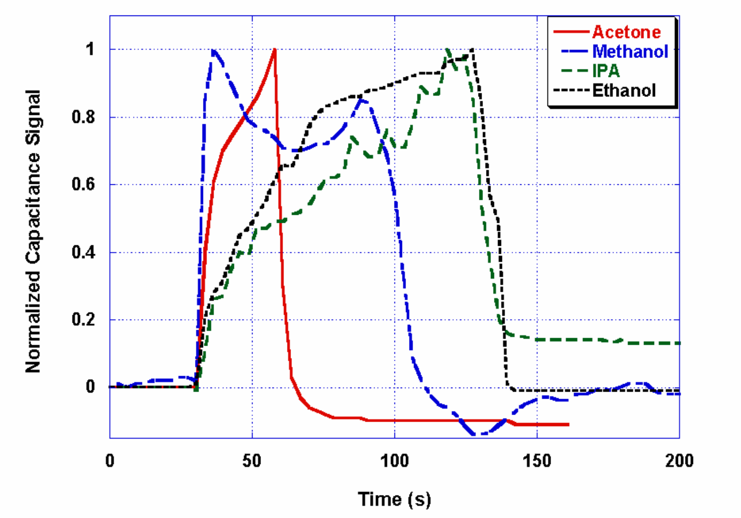

Figure 7.11 Normalized capacitive signals for various solvents overlaid on top of one another.

Acetone has the highest vapor pressure of 233 torr and as expected, exhibits the shortest signal duration of approximately 30 seconds. Correlation of vapor pressure is seen with signal duration and an indirect linear relationship exists between the two. Figure 7.12 shows a graph relating duration of signal and vapor pressure.

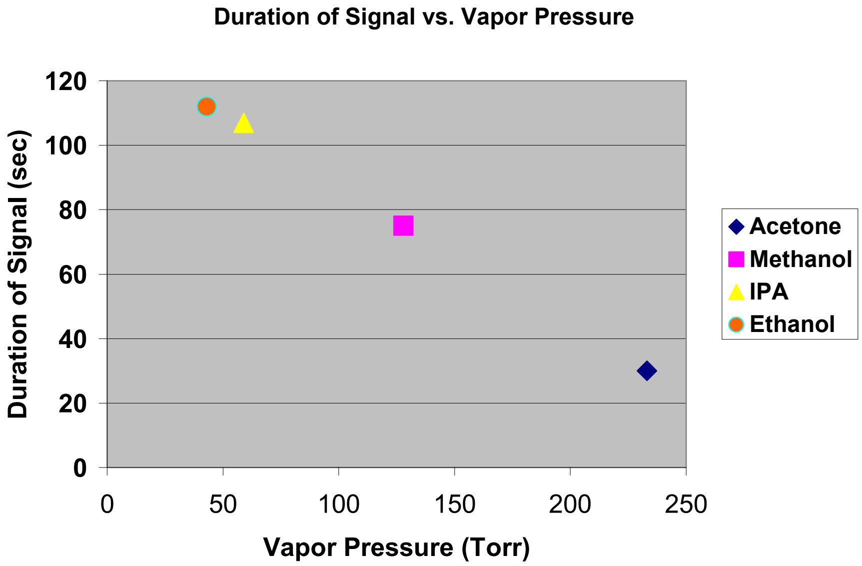

Figure 7.12. A graph depicting the indirect linear relationship between vapor pressure and duration of signal in a sensor for acetone, methanol, IPA, and ethanol.

Based on these four solvents; the duration of signal declines linearly with vapor pressure. Further investigation of this can determine how effective the device is at determining the exact vapor pressure of various chemicals.

Chemical properties such as dielectric constant and dipole moment appear to have no correlation to signal strength for solvents such as acetone, ethanol, IPA, methanol, and toluene. This further supports that the measured capacitive response resulting from solvents in the sensing membrane is a result of modulation of the space charge region in the semiconductor and not from the addition of a material with a different permittivity.

Looking at the signals obtained from the five test solvents on Figure 7.10 and 7.11, it is possible to discern distinct differences between them. This is an important feature of the sensor because discrimination between various solvents can be achieved. Toluene generates a very small signal much unlike any other present in the tests. Acetone is unique because of its short signal duration. Methanol stands out because it has two characteristic peaks. Both ethanol and IPA are similar; however, the top portion of the peak of IPA is irregular while ethanol is smooth and ramped towards a peak value.

If the unique signature of a chemical is known ahead of time, a computer program could be used to relate mathematical similarities between a test sample and a stored databank of these signatures could take place.  Quantitative analysis could be used to identify and discriminate between various chemicals and their unique electrical response.

To achieve reliable discrimination between signatures they must be reproducible on a day-to-day basis.  Figure 7.13 a) and b) show normalized acetone and IPA signatures taken over a period of 8 days.

a)

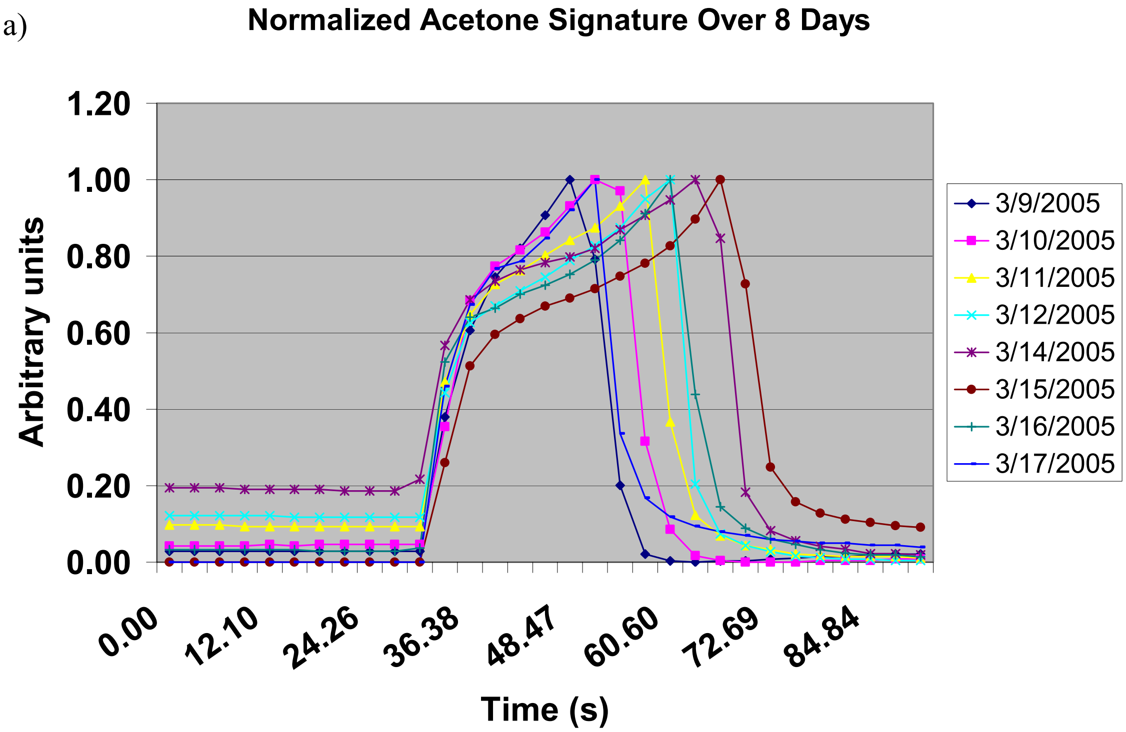

b)

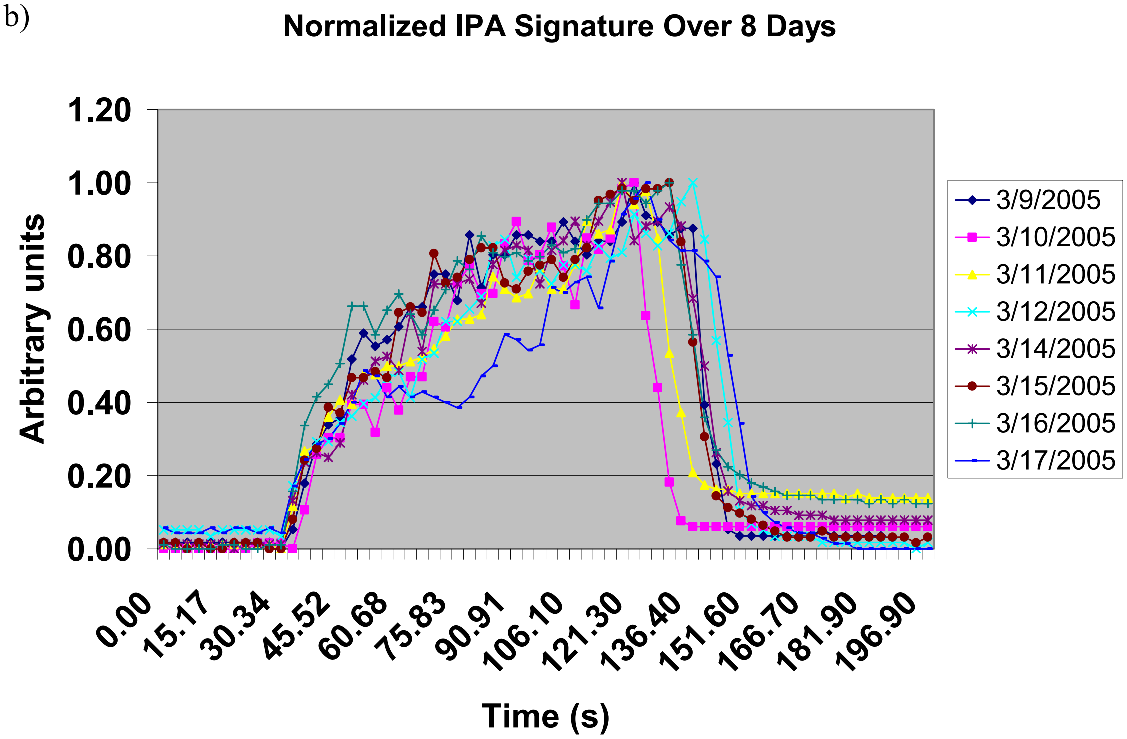

Figure 7.13. a) Reproduced exposure of a sensor to acetone over the course of eight days. b) Reproduced exposure of a sensor to IPA over the course of eight days.

The normalized signatures of acetone and IPA change slightly on a day-to-day basis. Minor variations in ambient conditions as discussed in Section 7.2 and variations in sample size as seen in Figure 7.8 could be the result of this. Overall, the signatures do exhibit a similar response from a day-to-day basis and this strongly suggests that computational analysis can be used to analyze characteristic signals generated by various chemicals for discrimination and identification purposes.

### 7.3.2 Vapor phase solvent detection

The sensor was used to measure various vapor phase concentrations of acetone and methanol. The experiments were housed in a 1525 ml desiccator which was used to isolate a localized ambient that could be controlled to achieve various vapor phase concentrations. A known volume of liquid phase solvent was injected into the bottom of the desiccator. Over a period of time, the solvent completely evaporated into the space confined by the desiccator. The concentration of vapor in parts per million is determined with the following equation:

$$\frac{\text{Weight of sample (mg)}}{\text{Chamber volume } (\text{m}^{3})} \times \frac{\begin{array}{c}\text{Volume of one mole of air at standard}\\ \text{temperature and pressure (L/mole)}\end{array}}{\begin{array}{c}\text{Molecular weight of sample}\\ \text{(g/mole)}\end{array}} = \text{Concentration in PPM}$$

Assuming the solvent completely converts to vapor phase, this calculation is an accurate way to determine part per million concentration levels of solvents with different molecular weight. Table 7.3 shows the estimated vapor concentration for given volumes of solvent injected into the desiccator.

| Sample volume (ml) | PPM of acetone | PPM of ethanol | PPM of IPA | PPM of methanol |
|---|---|---|---|---|
| 0.002 | 0.39 | 0.51 | 0.39 | 0.73 |
| 0.3 | 59.74 | 75.77 | 57.81 | 109.21 |
| 0.7 | 139.40 | 176.797 | 134.89 | 254.82 |
| 1.1 | 219.05 | 277.82 | 211.97 | 400.433 |
| 1.3 | 258.88 | 328.34 | 250.51 | 473.24 |
| 1.5 | 298.71 | 378.85 | 289.05 | 546.05 |

Table 7.3. Calculated part per million concentrations for various sample volumes injected into a 1525 ml desiccator.

Figure 7.14 a) and b) show a family of curves for various concentrations of acetone and methanol.

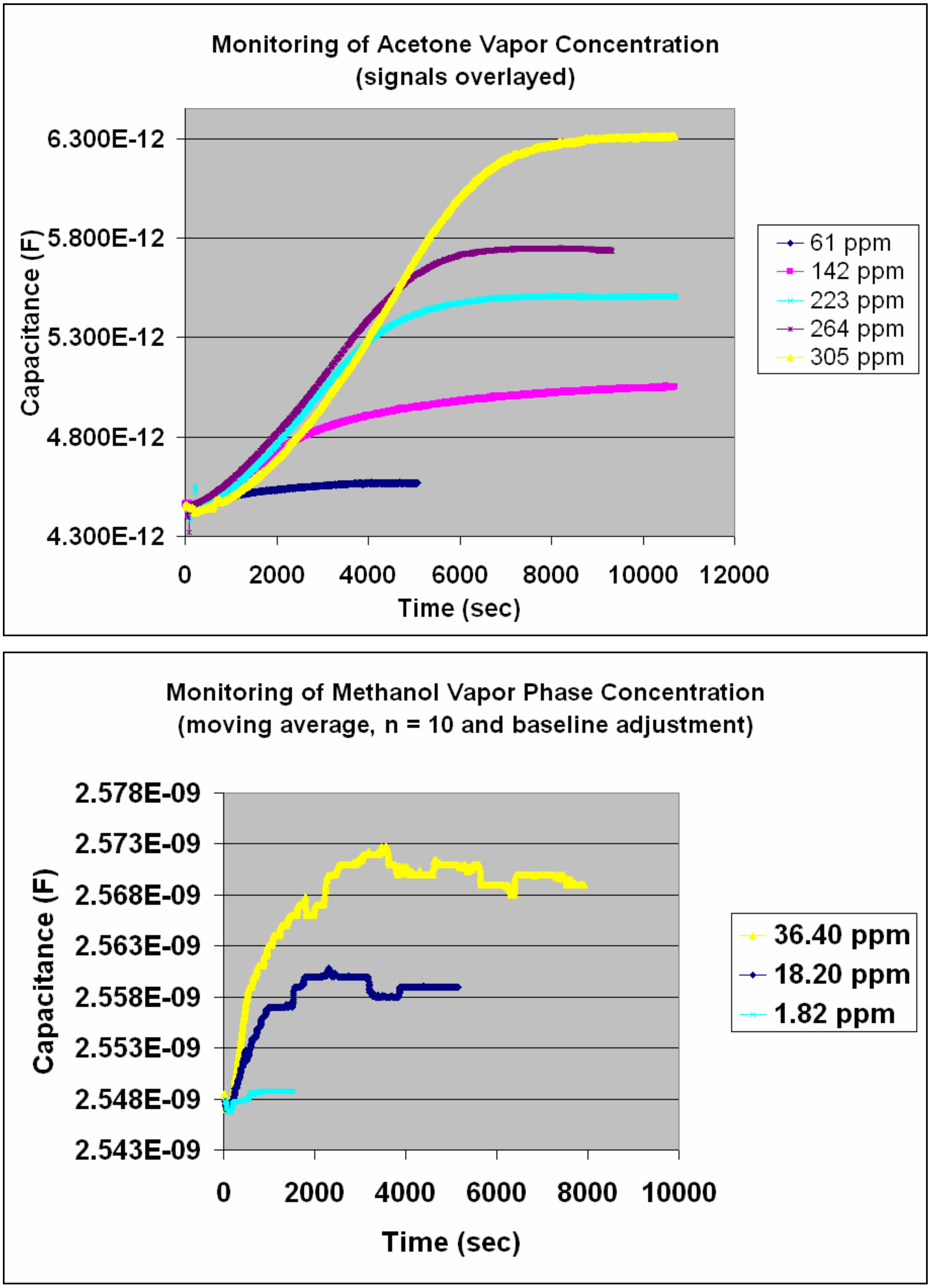

Figure 7.14. a) Monitoring of vapor phase acetone ranging in concentration from 305 – 61 ppm. b) Detection of methanol vapor at concentrations ranging from 36.4 – 1.82 ppm.

At 0 seconds the liquid phase solvent is introduced into the desiccator. An increase in capacitance is recorded as the solvent evaporates and fills the chamber. The calculated vapor concentration is achieved once all of the liquid phase solvent is converted to vapor phase which is indicated by a leveling off of measured capacitance. As seen in Figure 7.14, each concentration results in the signal leveling off to a different final capacitive value. Higher concentrations result in a larger change in capacitance because there are more airborne solvent droplets interacting with the semiconductor.

The lowest recorded vapor phase concentration level that has been detected is seen in Figure 7.15.

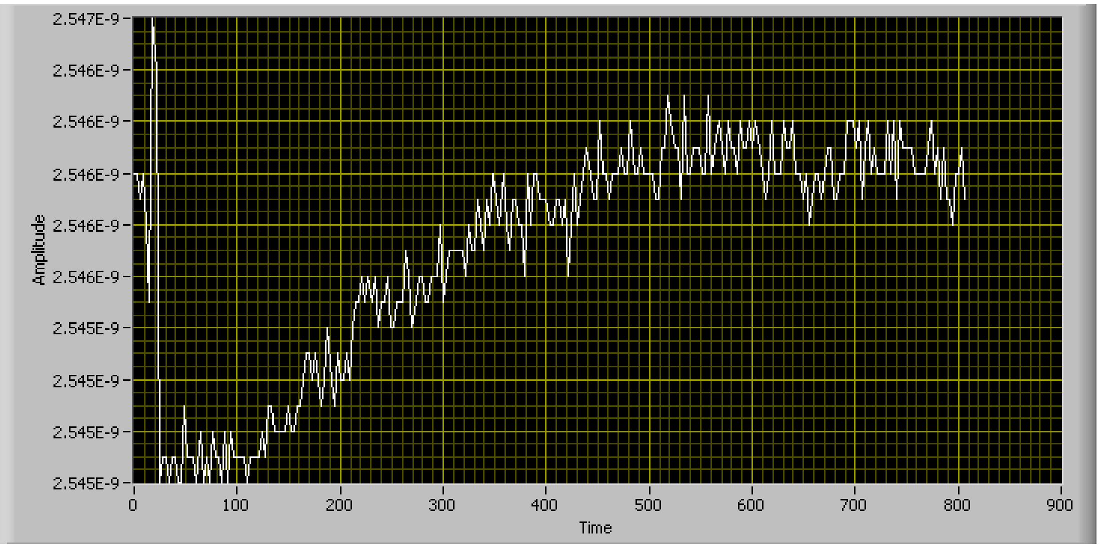

Figure 7.15. Capacitive response of sensor to 0.728 ppm of vapor phase methanol.

This capacitive response from this sensor is a result of dispensing 2 µl of methanol into the desiccator at T = 20 sec. Once converted to vapor phase the concentration is < 1 ppm. The large spike at T < 20 sec is from lifting the lid of the desiccator to dispense solvent into the chamber. The sensor was exposed to room light during this time which resulted in noise during the first part of the measurement. At concentration levels < 1 ppm it is important to consider signal noise resulting from variable ambient conditions such as temperature, light, and relative humidity.

### 7.4 Biological detection of protein binding

A change in measured capacitance occurred when sensors were used to monitor binding events between biotin and streptavidin protein. Chapter 4.3 and section A of the appendix provide details on the binding process of biotin protein to the walls inside the MPS. Capacitive baseline measurements were taken followed by two successive deliveries of 20 mM potassium phosphate buffer, pH = 6.5, as seen in Figure 7.16.

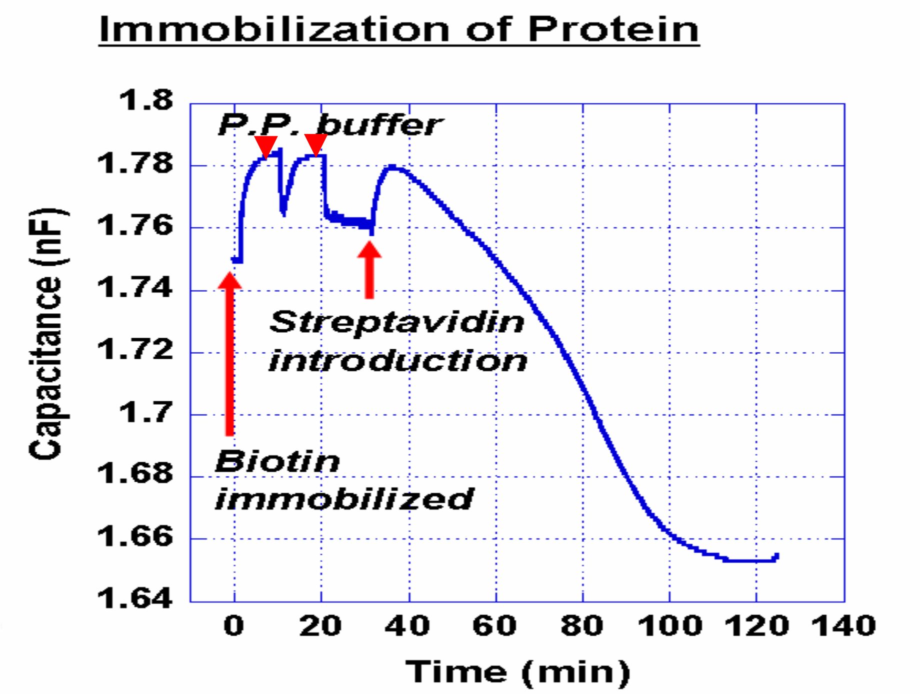

Figure 7.16. Real-time capacitive measurements of two deliveries of potassium phosphate buffer and then a final delivery of streptavidin protein. A large decrease in capacitance over a period of time occurs as a result of streptavidin delivery.

The initial two peaks resulting from potassium phosphate buffer are nearly identical. A third and very different peak is seen when streptavidin protein is introduced into the membrane. For nearly 90 minutes a decrease in capacitance occurs. Such a signal response is rare; however additional tests have also demonstrated a large decrease in measured capacitance over an extended period of time. A decrease in capacitance lasting for this duration strongly suggests that binding events between the biotin and streptavidin proteins are occurring.

## 7.5 Concluding remarks

This sensing platform has undergone electrical testing to explore and characterize its potential to perform operations in chemical and biological detection. Sensitivity to ambient conditions such as temperature, light and relative humidity has been quantified. The sensor exhibits a unique capacitive response during exposure to different liquid phase solvents which establishes it as a very capable tool for detecting and discriminating between solvents. If the signal response to various chemicals is known ahead of time, the sensor can be used to identify unknown chemicals. An interesting aspect of this sensor is that it can be used to characterize the physical properties of different chemicals. An example of this is demonstrated by an indirect, linear relationship between signal duration and vapor pressure. Furthermore, the device is capable of monitoring the quality of an air supply. This has been demonstrated by the detection of a 2 μl sample of methanol evaporating into a calculated vapor concentration of < 1 ppm. Investigation of the sensor's reliability has shown that detection of liquid and vapor phase solvents are repeatable over many successive exposures and reproducible over a period of many days. The only indication that the sensor will fail to perform is seen when exposed to toluene. This is important from a theory standpoint and strongly supports that the sensing mechanism is based on field-effect modulation of a space charge region in the semiconductor and not the direct measurement of permittivity of the analyte. Lastly, the sensor has been shown to be capable of biological event detection. A large decrease in capacitance is seen many minutes after streptavidin is placed into a sensing membrane functionalized with biotin. This signal response, which has not been seen in any other electrical characterization effort, is attributed to binding events between the biotin and streptavidin protein. The following chapter will demonstrate how the functionality of the sensor can be further enhanced by packaging it into a more complex fluidic package which renders it useful in water monitoring.

## Chapter 8

# Integration of a Fluidic System

### 8.1 Rationale

With today's efforts directed towards developing lab-on-a-chip technology and our device's potential to fulfill sensing demands within this area, it is critical that our device can incorporate fluidic systems. Integrating a fluidic system to the flow-through structure increases the capability and functionality of the device as a whole. It realizes complex array sensing opportunities by providing precise delivery of an analyte to specific sensing regions.

### 8.2 Fluidics for device packaging

Device packaging has always been a challenge in MEMS technology, and this device is not an exception [59]. Efforts were focused on a packaging solution robust enough to handle multiple stipulations associated with complex packaging needs specific to sensors operation. Other similar devices do not make such considerations and often require large bench-test setups to perform sensing operations. In this design, as seen in Figure 8.1, electronic and fluidic systems are placed on separate sides of a chip to ease packaging concerns.

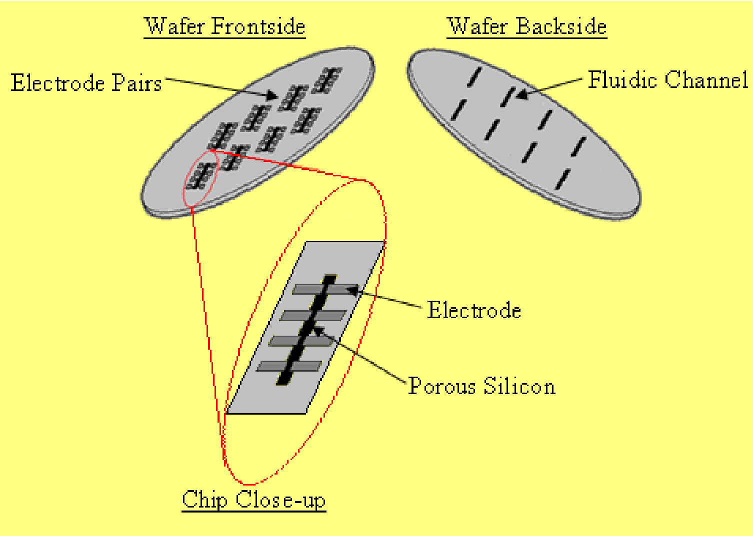

Figure 8.1. Substrate front and back side views. Electrodes are positioned on the front side of the device while fluidics are placed on the backside of the device.

The inherent design of the sensor places the electrical and fluidic components on separate side of the device. In this case, adding a fluidic package is not complicated by the electrodes because the backside fluidic channels and frontside electrodes are independent of one another. Any complications in electrode design caused by fluidics are relieved because all of the fluidic components are located away from the electrical system on the opposite side of the device.

## 8.3 Fluidics for array capabilities

Fluidic packaging is necessary for precise analyte handling which often requires dispensing a sample volume across an array of sensors. For DNA identification it is desirable to bring a sample into contact with multiple pDNA strands. An array of sensors could be pre-programmed with various pDNA and a fluidic system could be used to dispense a sample globally across the array. Electrical measurements taken from each sensor in the array can detect hybridization occurring at specific sites and the DNA under question can be identified. Figure 8.2 shows a fluidic system capable of performing DNA identification.

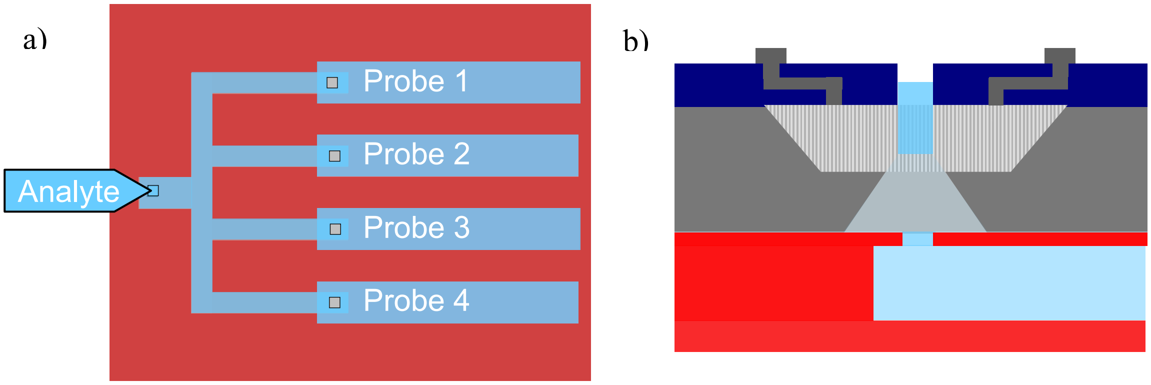

Figure 8.2 a) Planar array of four individual sensors preprogrammed to sense different target materials. b) Cross-sectional view of an individual sensor filled with an analyte.

Application of this device to the field of biology is difficult and many special considerations are necessary in doing so. Metrics for a fluidic packaging used with this device include biological and chemical compatibility, low levels of cytotoxicity, suitable electrical input/output interfacing, and ease of analyte input/output.

## 8.4 Towards a first generation fluidic package

Initial efforts were focused on creating a fluidic system composed of glass cover slides and Si wafers. The glass slides were drilled with diamond tipped dental drill bits to form fluidic vias and layered in a fixed fashion with patterned SU-8 epoxy to form fluidic channels. This approach allows the use of conventional IC and MEMS microfabrication techniques and enables the creation of fluidic systems on a micron based scale. Although this packaging scheme was not ultimately utilized for the finished device, research herein provides useful information pertaining to such an approach.

### 8.4.1 Investigation of cover-slip drilling

Glass slides or cover-slips measuring 2”x 3”x 1mm were used in a layered fashion to create fluidic channels. In order for fluid to enter or leave a channel, a via or hole through the slide is necessary. To do this a dental grade, diamond tipped drill bit was used to bore 1 mm holes entirely through the glass slide. Figure 8.3 shows the retrofitted drill stand and various drill bits that were used for drilling.

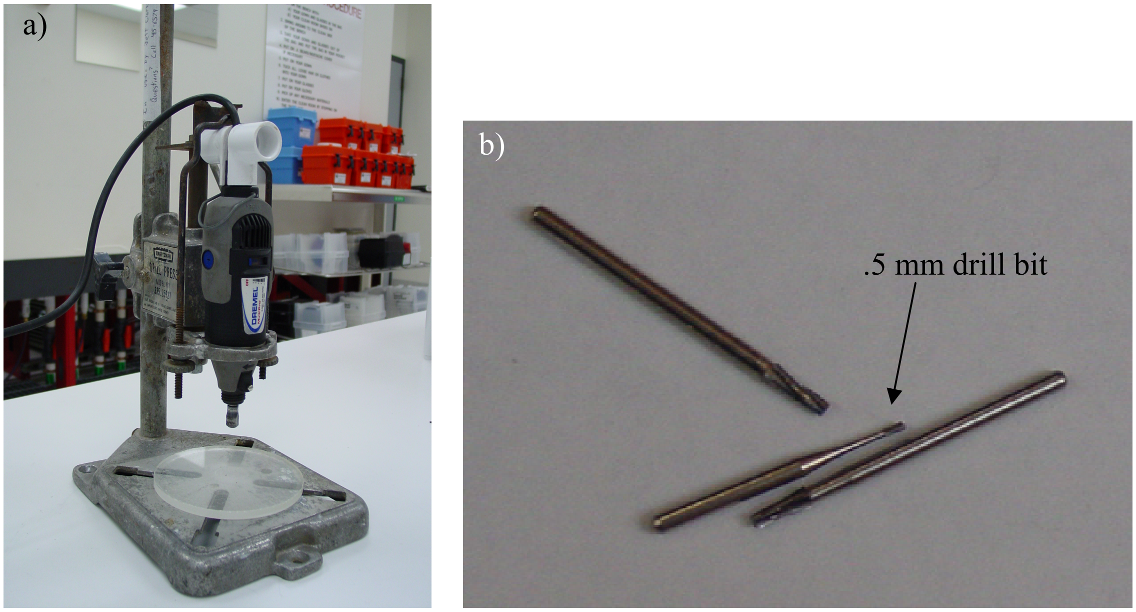

Figure 8.3 a) A dremel tool mounted in a portable drill press. b) Various drill bits used to drill.

The drill stand was created with a portable drill press that was fitted to house a dremel tool capable of spinning at 35,000 rpm. A level was used to ensure that the drill would contact the substrates in a perpendicular fashion during the drilling process. Figure 8.4 shows a detailed schematic of the retrofit drill outfit.

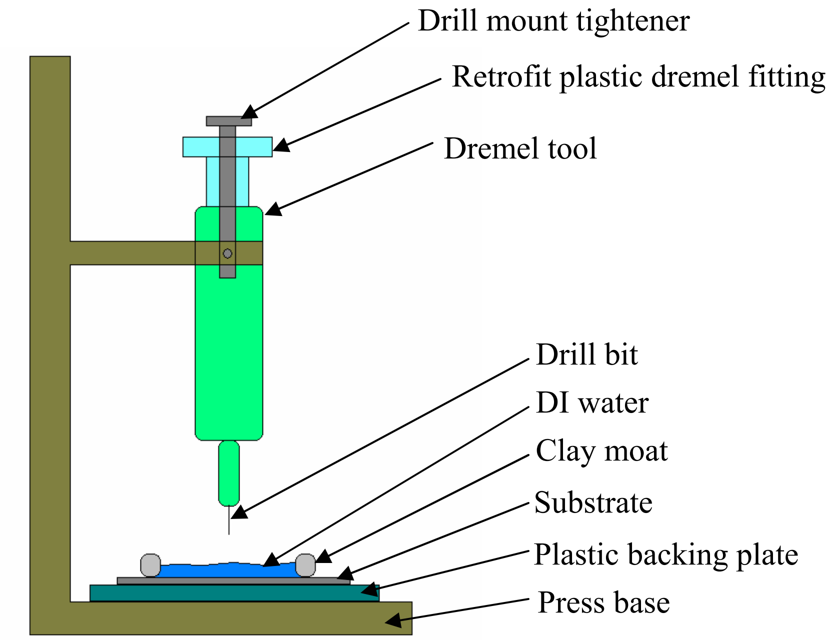

Figure 8.4 Schematic representation of a side view of the retrofitted drill press used to bore holes in glass and Si substrates.

Slides were placed on the base of the press and secured in place with small 3" clamps. Any surface making contact with the glass slide was coated with a layer of electrical tape to reduce the risk of damage. After the glass slide is secure, a ring of modeling clay is used to form a moat around the area to be drilled. Cooling during the drilling process is done by pouring deionized water into the moat. Finally, the dremel tool rotating at 35,000 rpm is brought down slowly by hand in the direction of the liquid cooled glass slide. Contact force between the drill bit and glass slide should be minimized and the drill bit should not exceed a rate of 1 mm per minute when traveling through the glass slides. Figure 8.5 shows a cover slide with multiple vias drilled in it for an arrayed fluidic system.

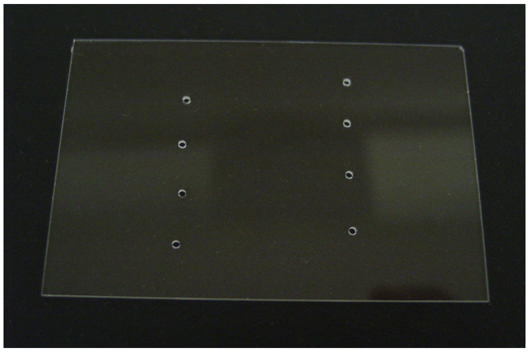

Figure 8.5 A glass cover slide with eight drilled holes for a fluidic array.

Drilling holes in glass is not a particularly clean undertaking. Substrates that have been drilled need to be washed with soap and water to remove residue remaining from the modeling clay. If the cover-slide is being used as a fluidic layer and will under go bonding with SU-8, it is also suggested to RCA clean or Piranha etch the substrate prior to this. The smallest possible via size is dependent on the drill bit size, and the smallest diamond tipped bit found was 0.5 mm.

### 8.4.2 Investigation of SU-8 patterned channels

Prior research has shown that microscale fluidics channels can be patterned and bonded to cover-slides with SU-8 photoresist [60-61]. An investigation of this resulted in successful patterning of fluidic channels measuring 1 mm wide by 300 μm tall on glass slides. MicroChem 2100 SU-8 epoxy based negative photoresist was selected because it is biocompatible and highly stable when exposed to solvents, acids, and bases [62]. In addition to this, conventional IC and MEMS fabrication techniques can be used to with this material.

Glass substrates were RCA cleaned and then mounted onto a 6 inch Si substrate. The mounted slide was placed into a resist spinner where the SU-8 was dynamically dispensed and ramped to a final spin speed of 1000 rpm. This spin speed is targeted to yield a film thickness of 300 μm. A detailed account of the optimized procedure can be found in part D of the appendix.

Due to the film thickness, long thermal ramping steps on the order of several hours are necessary to minimize film stress while driving out solvents. Initial results of patterned SU-8 films yielded poor adhesion to the glass slide and major delamination of the film occurred. To improve upon this, techniques such as using a piranha etch to clean the glass slides, increasing spin speed to thin the film, and slowing ramp speeds to reduce stress were used. The optimized process yielded a better quality film with minimal film delamination. Figure 8.6 shows results from the original and optimized procedures.

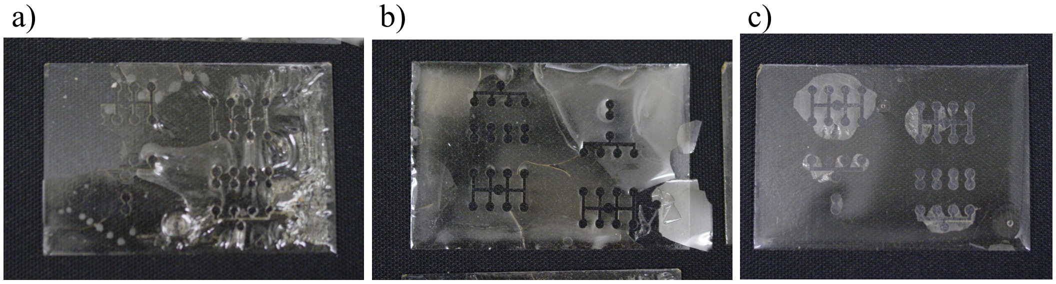

Figure 8.6 a) Non-optimized SU-8 process yielding a wrinkled and delaminated film. b) Non-optimized SU-8 process yielding a cracked and delaminated film. c) Optimized SU-8 process with minor film delamination.

It was believed that the high quality surface on 4-inch Si substrates would promote better adhesion of SU-8 films. The optimized SU-8 coating process was used on 4-inch Si substrates which were patterned with an identical channel design. The overall result was better than that seen on glass slides. However, a small area of delamination did occur. Figure 8.7 shows a 4-inch Si substrate patterned with the optimized SU-8 process.

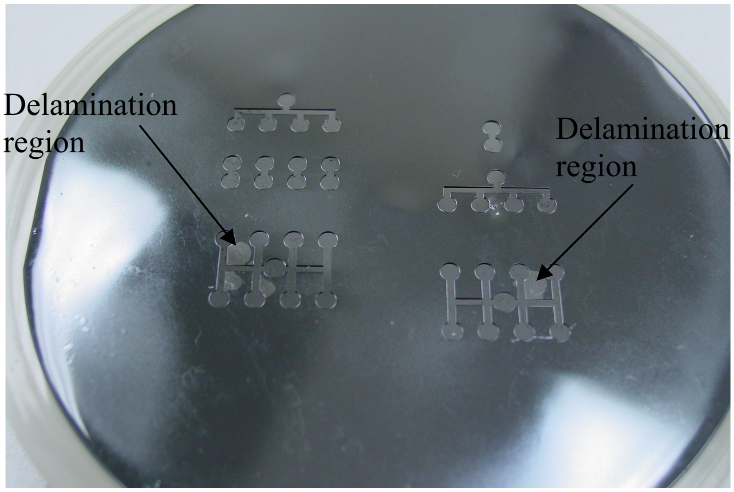

Figure 8.7 A 4-inch Si wafer patterned with an optimized SU-8 process. Minimal delamination can be seen as lighter colored regions.

Experimentation showed that additional thermal treatments of the substrates patterned with SU-8 prompted more delamination. For this reason patterned substrates were never bonded and capped fluidic channels were never achieved. Although further development of this process is possible, preliminary indications suggested an alternate solution could be attained by redirecting efforts towards a laser etching process capable of providing rapid fabrication of similar fluidic systems at the required dimensions.

## 8.5 Second generation fluidic package

The ultimate fluidic packaging solution was found in a laser etching process. This technique provides macro scale features with very rapid fabrication times. This process utilizes a Universal Laser Systems, Inc. M-300 Laser Platform, as seen in Figure 8.8 which is essentially a laser mounted plotter.

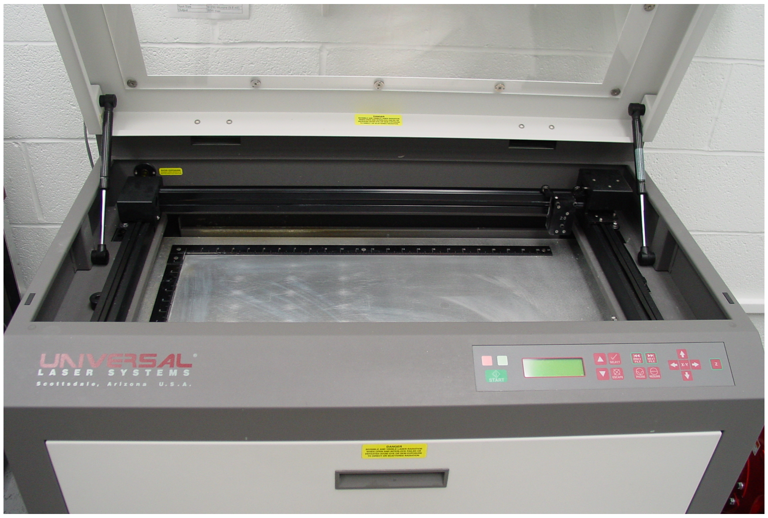

Figure 8.8. Image of a Universal Laser Systems, Inc M-300 Laser Platform courtesy of Nate Wescott. The protective door is open revealing the platform where Dura-Lar and ARCare 8890 plastic sheets are lased.

The maximum power output of the $CO_2$ laser is 50 W at a wavelength between 630 - 680 nm. Designs are created with Corel Draw software and sent to the plotter as a print job. Plastic sheets of Grafix 20 mil Dura-Lar laminated with Adhesives Research Inc, 2.5 mil ARCare 8890 are placed onto a metal platen in the etcher. Once the design file is sent to be printed, the laser scans across the adhesive laminated sheets according to the desired design.

The fluidic package is comprised of multiple plastic layers that each have specific features which contribute to the entire fluidic system as a whole. The layers which are laminated with ARCare 8890 double sided adhesive tape are aligned and sandwiched together to create fluidic channels and form the final fluidic package. Figure 8.9 shows a fluidic package consisting of three layers used for a single port system.

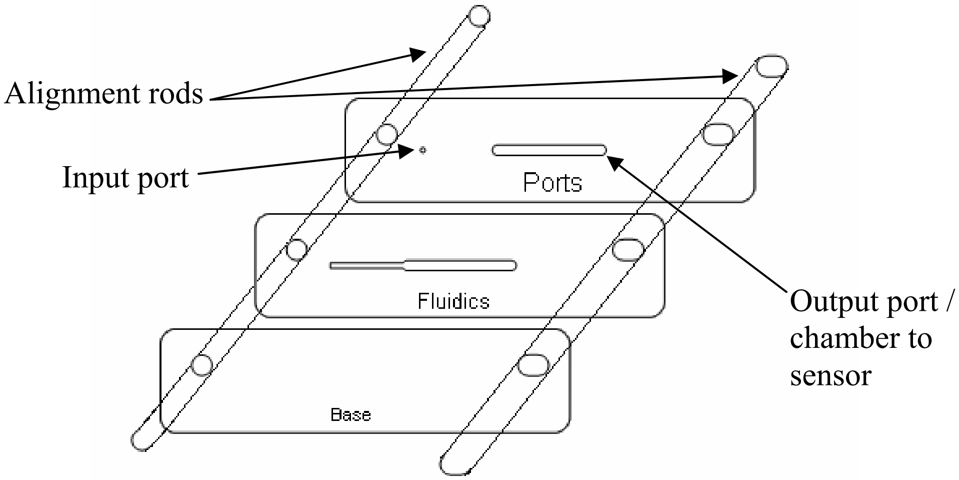

Figure 8.9. The base, fluidics, and ports layer are aligned with rods and sandwiched together with double sided adhesive to form the final fluidic package.

Rods are placed through the alignment holes of each layer to ensure proper alignment when the layers are adhered to one another. Each layer is specifically designed to be an individual part of the entire fluidic system. The base layer serves as a capping layer to form the bottom of the fluidic channel. The fluidic layer defines the length, width and depth of the fluidic channels. Lastly, the port layer establishes where fluid enters and exits the package. Figure 8.10 shows three different designs and their corresponding layers.

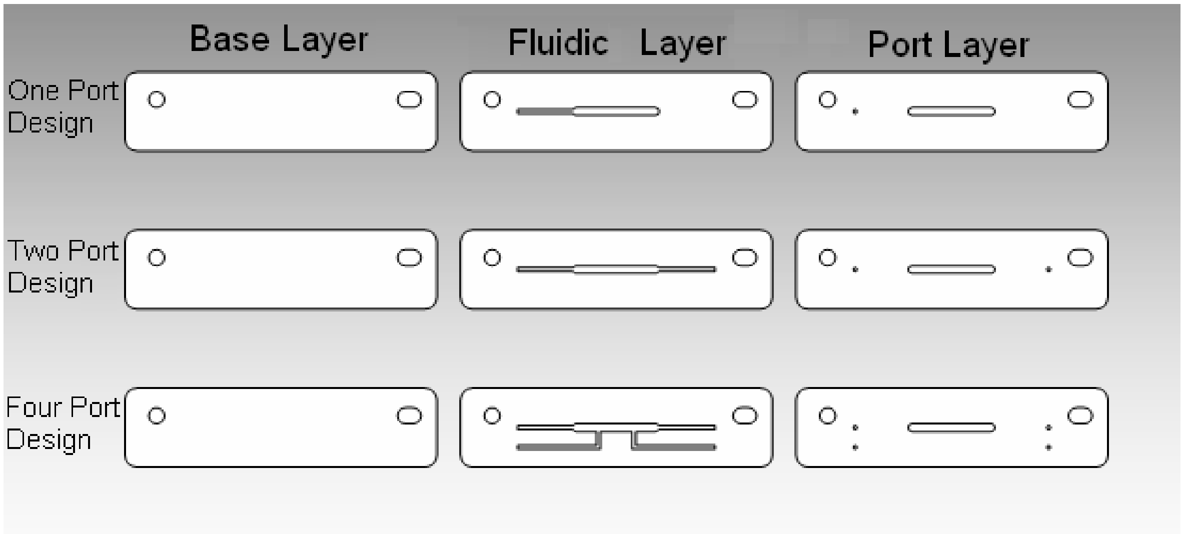

Figure 8.10 Schematic view of base, fluidic, and port layers for one port, two port, and four port designs.

Once the three layers are combined to form the fluidic package an adhesive patch is positioned over the region where the sensing device will be placed. The chip is then aligned to the patch on the package and pressed into place. Figure 8.11 shows a top-down view of devices placed on the three different package designs.

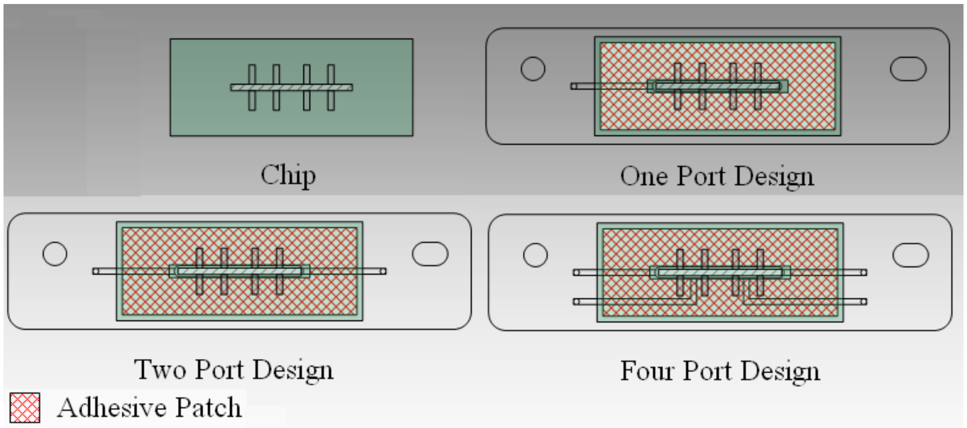

Figure 8.11 Schematic view of chips mounted in fluidic packages with an adhesive patch.

All three designs were fabricated on a 79 by 20 mm card. The ports, which measure 1 mm in diameter, connect to the fluidic channels which measure 1 mm wide and 635 µm high. Chambers which interface with the backside channels of the flow-through structure on the sensing device measure 22 by 2 by .635 mm and hold 22 µl of fluid. Once the chip is placed on the package the final chamber volume is 30 µl. A sample size of 75 µl is required because additional fluid is necessary to fill the fluidic channels that deliver fluid from the input port to the sensor. Figure 8.12 a) and b) shows the three different package designs and a two port package with a chip placed in it.

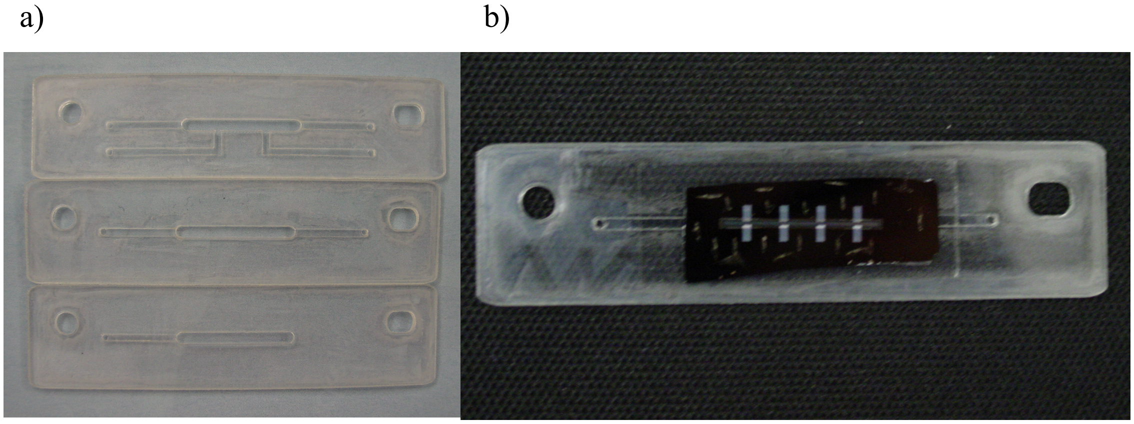

Figure 8.12 a) Three fabricated fluidic packages. b) A two port fluidic package with a chip placed in it.

As seen in Figure 8.12 a), the top-most fluidic system contains four input ports. If each of the four linearly arrayed electrode pairs had its own backside fluidic channel, as seen in Figure 8.13, an array of sensors which are individually addressable is possible.

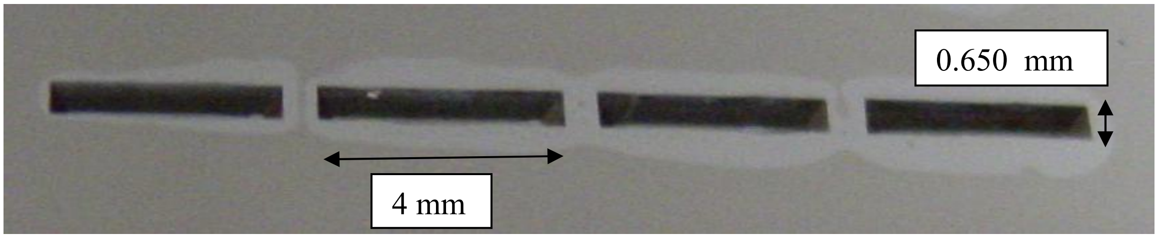

Figure 8.13. Four individual backside fluidic channels measuring 4 x 0.650 mm in size. Individual channels allow for arrayed sensing opportunities.

With a final packaged sensing system at hand, more applications can be found. This system is an ideal candidate to perform biological event detection as discussed in Sections 4.3 and 7.4 because the necessary samples can simply be circulated through the fluidic system. Additional applications for this sensing platform include water and air monitoring, blood and urine sampling, and even has the potentially for chemical analysis.

## 8.6 Packaged system for water monitoring

This sensing device, when packaged and placed in series with a water supply, is an ideal technology to monitor water supplies. Devices were placed in two-port packages and then used to detect the presence of IPA in a DI water source. A micropipette was used to deliver a total sample volume of 70 µl in 10 µl increments. As the water enters the input port of the package it travels across the sensing membrane towards the output port where it is eventually evacuated. As water was injected into the package real-time capacitive measurements were taken as seen in Figure 8.14.

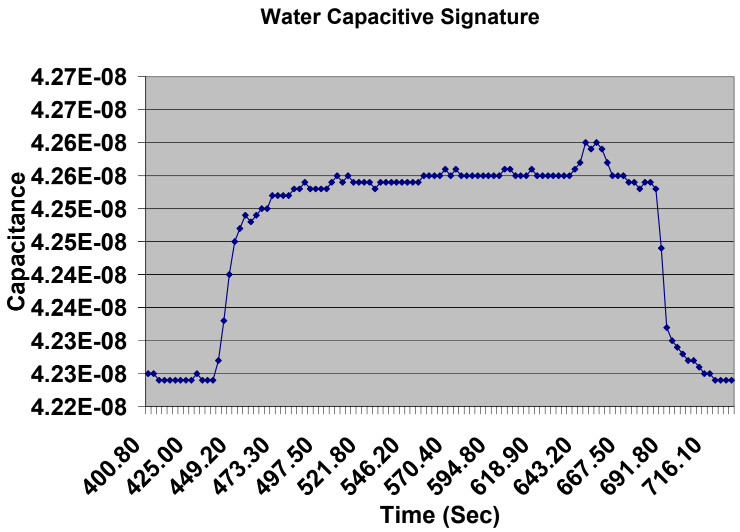

Figure 8.14. Real-time capacitive measurements taken during water delivery to the packaged sensor.

As DI water was injected at approximately 445 sec, a rise in capacitance occurs. The DI water is allowed to remain in the fluidic system until approximately 650 sec, at which time the liquid is evacuated from the package by flowing nitrogen gas through the fluidic system and collecting it with a micropipette. In this test, removal of the water takes approximately 15 seconds, after which a decrease and return to baseline capacitance is seen.

Figure 8.15 a) and b) shows four successive injections and evacuations of DI water and contaminated DI water containing 50% IPA.

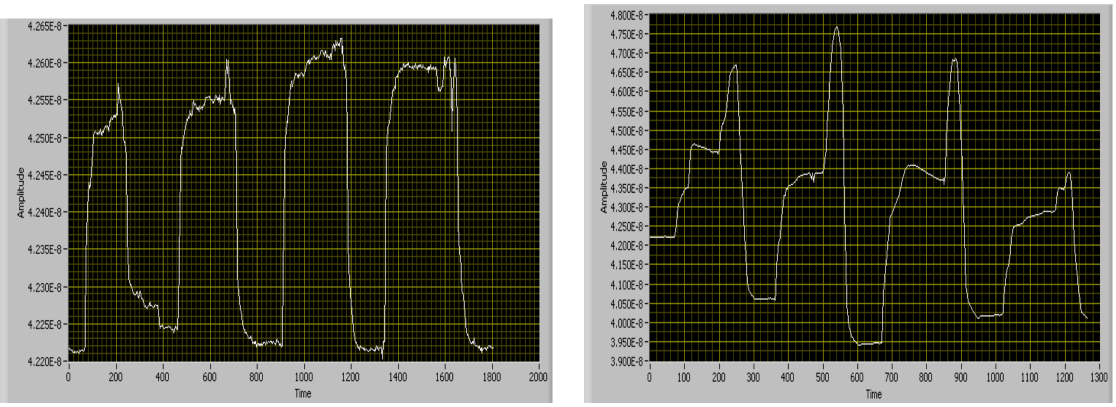

Figure 8.15 a) Four successive deliveries of DI water as represented by four peaks in measured capacitance. A change in approximately 0.25 nF occurs. b) Four successive deliveries of contaminated DI water with 50% IPA indicated as four peaks in capacitance. The first step of the peak, a change in capacitance of approximately 2.25 nF is the measured capacitance from the contaminated water and the following spike is a result of nitrogen gas which is used to evacuate the sample from the fluidic system.

It is important to note than in Figure 7.17 b) the step-like peaks of contaminated DI water are unlike the DI water peaks. The first increase in capacitance is from the injection of contaminated water and this should be taken as the measured capacitance associated to it. As the liquid is displaced with nitrogen gas, a large spike in capacitance is observed. It is believed that this spike in capacitance is caused by nitrogen pushing more fluid into the sensing membrane for a brief period of time while it travels through the fluidic system.

Additional fluid in the sensing membrane would result in more modulation of the space charge region in the semiconductor and an increase in capacitance. Once the sample is completely evacuated from the fluidic package, measured capacitance decreases sharply to a baseline value.

Final experiments were preformed to monitor IPA contamination levels of a water supply as it was introduced and evacuated from the packaged sensor. The results obtained during this water quality monitoring are repeatable and can be seen in Figure 8.16.

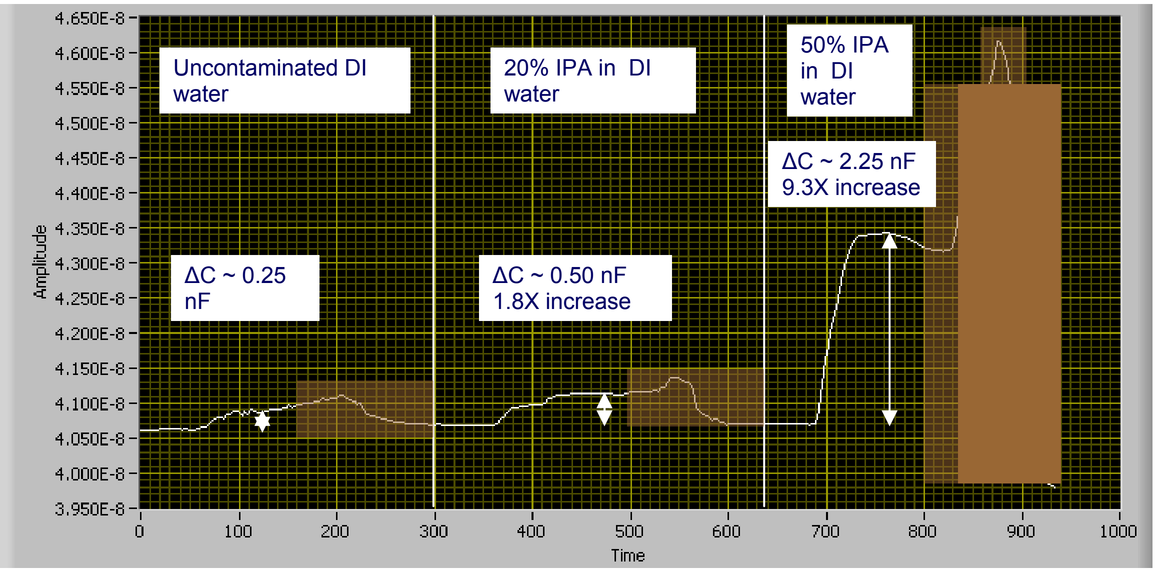

Figure 8.16. Three capacitive signatures measured with an individual sensor from left to right are pure DI water, 20% contaminated DI water with IPA, and 50% contaminated DI water with IPA. Shaded regions are measured capacitive response resulting from nitrogen gas which is used to evacuate samples.

From left to right, three successive peaks resulting from DI water, contaminated DI water with 20% IPA, and contaminated DI water with 50% IPA can be seen. As expected, the most contaminated water supply with 50% IPA resulted in the largest capacitive change. Analysis of the data shows that the 20% and 50% contaminated samples yielded a change in capacitance 1.8 and 9.3 times greater than pure DI water. The sensor's ability to measure a baseline capacitance value resulting from pure water and detecting deviations from this clearly demonstrate the capabilities of this device in monitoring the quality of a water supply.

## 8.7 Concluding remarks

Initially, standard IC and MEMS process technologies were used to pattern fluidic channels in epoxy based SU-8 films. This approach has the potential to integrate micro scaled fluidic systems to the sensing device. Timely thermal ramps on the order of many hours and delamination of SU-8 from glass and Si surfaces complicated this process and other fluidic packaging options were explored.

Laser etching, a rapid process capable of fabricating macroscale fluidic packages, was used as the ultimate packaging solution. Individual layers are designed as components to an entire fluidic system, aligned, and then sandwiched together with double sided adhesive tape to form the complete fluidic package. This technology, including design and fabrication yielded 24 fluidic packages in approximately the time it takes to pattern the surface of one glass slide with SU-8. If micro scale fluidics were necessary, perhaps a laser with a smaller spot size could be used.

The integration of a fluidic package for the creation of a complete sensing system increases the overall capability of the sensor and establishes it a viable means for monitoring water supplies. Packaged sensors demonstrated repeatable changes in capacitance for contaminated and uncontaminated supplies. Measured responses of 1.8 and 9.3 times that of an uncontaminated water source were observed for 20% and 50% IPA contaminated water supplies respectively.

## Chapter 9

# Final Conclusions

### 9.1 Project description and relevant results

This work describes the development of a MPS flow-through field effect sensing system capable of performing sensory operations for chemical and biological detection. The large surface area of MPS and the sensitivity of its surface to fluids with charged molecules make it an ideal material for sensor development. Realization of a flow-through structure makes this sensing platform unique in that monolithic integration of self-aligned backside fluidic channel and frontside MPS sensing membrane is achieved. Through organization of frontside electrodes and backside fluidics, the sensing device can be packaged without complication.

The majority of the sensors were fabricated with 49 process steps and four photolithography levels. Standard IC and MEMS process technologies were used throughout the majority of the process. Under some conditions, non-standard or non-conventional fabrication steps were developed and used. The passivation of MPS is a good example of this where oxide and nitride thin films were used to protect the MPS from KOH etching. By combining this fabrication technique with proper design of the backside KOH etching mask, flow-through structures were achieved.

Electrodes were integrated into the MPS flow-through structure to realize a final device. A basic isolation scheme was developed and used on the majority of the fabricated sensors to protect electrodes from analyte-induced shorts. A more complex isolation which greatly increased fabrication time and complexity was also created. This scheme was rarely used because the basic and less complex scheme provided acceptable levels of isolation between electrodes with greatly reduced fabrication time.

With fabricated sensors at hand, electrical tests were used to characterize the sensor. A GUI was created with LabVIEW software to control and collect real-time capacitive measurements with a HP 4275A LCR multifrequency meter. The sensor's response to ambient conditions was quantified to understand ambient induced error, if any, during targeted measurements of analytes.

The sensor exhibited a unique capacitive response to acetone, ethanol, IPA, methanol, and toluene solvents. An approximate change in capacitance for acetone, ethanol, IPA, and methanol is approximately 0.207, 0.194, 0.057, 0.216 nF, respectively. If the capacitive response for a chemical is known ahead of time, the measured capacitive response from an unknown analyte can be correlated to a database and discrimination between chemicals can be achieved. This has been demonstrated through visually different capacitive signatures exhibited by aforementioned solvents.

A relationship was found between signal duration and vapor pressure for various solvents. The duration of measured signals with a sensor was based on how long it lasted in the MPS sensing membrane before evaporating. A linear relationship between vapor pressure and signal duration exists and can be used for the characterization of an unknown vapor pressure for a given solvent.

Detection of solvent vapor was successfully achieved with the sensor. At this time, the sensor is recognized as a means to quantify concentrations of a known solvent and is not characterized to discriminate between solvents in their vapor phase. The lowest concentration measured was < 1 ppm of methanol vapor. This was achieved by placing 2 µl of liquid methanol in a 1525 ml desiccator with a sensor. As the solvent sample evaporated, an increase in measured capacitance occurred until the solvent was completely in vapor phase at which time the measured capacitance leveled off to a consistent value. This has been done for vapor phase detection of acetone ranging from 65 to 301 ppm.

Both liquid and vapor phase detection is repeatable over successive exposures and reproducible over many days. It is important to note that liquid phase toluene exposure renders the sensors useless. This is important from a theory standpoint and agrees with the proposed sensing mechanism which is based on field effect modulation of a space charge region in the semiconductor and not the direct measurement of permittivity of the analyte. It is believed that toluene causes permanent modification of the MPS oxide lining such that when it is interfaced with a liquid, modulation of the space charge region in the semiconductor is greatly hindered.

The sensor was used to detect binding events between biotin and streptavidin protein. MPS membranes were functionalized with aminosilane and a biotin linker. Once streptavidin protein, suspended in a liquid buffer solution, is introduced into the sensing membrane, a decrease in capacitance occurs over a long period of time. A measured response that exhibits a decrease in capacitance lasting a period of approximately 60 minutes has never been observed during any liquid phase measurements.

A fluidic package was designed and fabricated which would allow further application of the sensing system to more complex operations. One example of this is arrayed configurations for DNA identification. For the case of our packaged system, application to monitoring the quality of a water supply was investigated. The packed system was capable of quantifying a 20 and 50% contaminated DI water supply with IPA.

The development of this sensing system has only begun to realize its potential. A robust fabrication scheme will enable future sensor optimization. Examples of this include increasing sensor sensitivity by reducing MPS oxide thickness, modifying the backside KOH mask for arrayed sensing networks, and conducting capacitive measurements at different AC frequencies for increased signal-to-noise. A vast amount of sensor characterization remains. Chemical sensing of acids and bases, discrimination between vapor phase solvents, and detection of biological materials and events are all areas that need further investigation. Evidently, the true nature of this work involves an interdisciplinary understanding of fluidics, semiconductors, chemistry, biology, material science, etc. With a developed sensing platform at hand, it can now be placed in the hands of experts in such fields and emerge as a tool to further understand the world around us.

# Bibliography

[1] NASA's Observatorium Group. "Remote Sensing in History." Galileo 1906. 1998. BDM Federal, Inc. <http://observe.arc.nasa.gov/nasa/exhibits/history/history_2.html>.

[2] All Sensors. "Sensor History." The Fairchild Semiconductor Days. 2005. <http://www.allsensors.com/history/SensorHistory.pdf>.

[3] D. M. Wilson, S. Hoyt, J. Janata, K. Booksh, L. Obando. "Chemical Sensors for Portable, Handheld Field Instruments." IEEE Sensors Journal, Vol. 1, No. 4 (2001): 256-274.

[4] H. Ouyang, L. DeLouise, M. Christophersen, B. L. Miller, P. M. Fauchet. "Biosensing with One-Dimensional Photonic Bandgap Structures." Proceedings of the SPIE, Volume 5511 (2004): 71-80.

[5] A. Janshoff, K. S. Dancil, C. Steinem, D. P. Greiner, V. S. Lin, C. Gurtner, K. Motesharei, M. Sailor, M. R. Ghadiri. "Macroporous p-Type Silicon Fabry-Perot Layers. Fabrication, Characterization, and Application in Biosensing." J. Am. Chem. Soc., Vol. 120, No 46 (1998): 12108-12116.

[6] L. De Stefano, L. Moretti, A. Lamberti, O. Longo, M. Rocchia, A. Rossi, P. Arcari, I. Rendina. "Optical Sensors for Vapors, Liquids, and Biological Molecules Based on Porous Silicon Technology." IEEE Trans. On Nanotechnology, Vol. 3 No. 1 (2004): 49-54.

[7] T. Vo-Dinh, G. Griffin, D. L. Stokes, A. Wintenburg. "Multi-functional Biochip for Medical Diagnostics and Pathogen Detection." Sensors and Actuators, B 90 (2003): 104-110.

[8] J. P. Clarkson, V. Rajalingam, K. D. Hirschman, P. M. Fauchet. "A Macroporous Silicon Field Effect Sensing System for Liquid Phase Solvent Detection." IEEE Sensors Proceedings. (2005): in press.

[9] B. Lillis, C Jungk, D. Iacapino, A. Whelton, E. Hurley, M. Sheehan, A. Splinter, A. Quinn, G. Redmond, W. Lane, A. Methewson, H. Berney. "Microporous Silicon and Biosensor Development: Structural Analysis, Electrical Characterizations and Biocapacity Evaluation." Biosensors and Bioelectronics, (2004): 1-11.

[10] K. D. Hirschman, M. Archer, D. Persaud, V. Rajalingam, J. Clarkson, J. Mann, D. Phillips, W. Sun, P. Fauchet. "Integrated Sensor Arrays with a

Configurable Network Interface for Chemical and Biological Detection." SPIE Optics East Exhibition Proceedings, Vol. 5591 (2004): 205-212 .

[11] J. N. Sniadecki. Field-Effect Flow Control in Microfluidics. Michigan: UMI, 2003.

[12] M. J. Sparnaay. "The Electric Double Layer." The International Encyclopedia of Physical Chemistry and Chemical Physics. D. H. Everett. Vol. 4 Topic 14. New York: Pergamon Press Ltd., 1972.

[13] M. Archer, M. Christophersen, P. M. Fauchet, D. Persaud, K. D. Hirschman, "Electrical Porous Silicon Microarray for DNA Hybridization Detection." MRS Proceedings, Vol. 782 A7.2 (2004).

[14] K. S. W. Sing *et al.* Pure Appl. Phys., Vol. 57 No. 4 (1985): 603.

[15] K. D. Hirschman, L. Tsybseskov, S. P. Duttagupta, P. M. Fauchet. "Silicon-Based Visible Light-Emitting Devices Integrated into Microelectronic Circuits." Nature, (1996): 338-341.

[16] L. Canham. Properties of Porous Silicon. Emis data reviews series No. 18 London: INSPEC, 1997. 18.

[17] A. HaliMaoui. Appl. Phy. Lett., Vol. 63 (1993): 1264.

[18] A. HaliMaoui. Surf. Sci Lett., (Netherlands) Vol. 306 (1994): L550-L554.

[19] R.L. Meek. Journal of Electrochemical Society, Vol. 118 (1971): 437-442.

[20] Y. Arita. Journal of Crystal Growth, Vol. 45 (1978): 383-392.

[21] X.G. Zhang, S.D. Collins, R.L. Smith. Journal of Electrochemical Society, Vol. 136 (1989): 1561-1565.

[22] X.G. Zhang. Journal of Electrochemical Society, Vol. 138 (1991): 3750-3756.

[23] C. Levy-Clement, A. Lagoubi, R. Tenne, M. Neumann Spallart. Electrochemical Acta., Vol. 37 (1992): 877-888.

[24] V. Lehman, U. Gosele. Applied Physics Letters., Vol. 58 (1991): 856.

[25] J. N. Chazalviel, J. C. Vial, J. Derrien. Porous Silicon Science and Technology. The silicon/electrolyte interface. Spinger-Verlag. Les Editions de Physique, (1995): 17-32.

[26] H. Foll, M. Christophersen, J. Carstensen, G. Hasse. “Formation and application of porous silicon.” Material Science Engineering, Vol. R 39 (2002): 93-141.

[27] R. L. Smith, S. D. Collins. “Porous silicon formation mechanisms.” Journal of Applied Physics, Vol. R1-R22 (1992): 71.

[28] J. N. Chazalviel, R. B. Wehrspohn, F. Ozanam. “Electrochemical preparation of porous semiconductors: from phenomenology to understanding.” Material Science Engineering, Vol. B69-70 (2000): 1-10.

[29] J. C. Claussen, J. Carstensen, M. Christophersen, S. Langa, H. Foll. “Self organized pore formation and open loop control in semiconductor etching.” Chaos, Vol. 13 (2003): 217-224.

[30] D. R. Turner. J. Electrochem. Soc., Vol. 105 (1958): 402.

[31] R. Memming, G. Schwandt. Surf. Sci., (Netherlands) Vol. 4 (1966): 109.

[32] L. Canham. Properties of Porous Silicon. Emis data reviews series No. 18 London: INSPEC, 1997. 89-96.

[33] L. Canham. Properties of Porous Silicon. Emis data reviews series No. 18 London: INSPEC, 1997. 15.

[34] M. Archer. “Investigation of the Electrical Sensing Properties of Porous Silicon for Biosensor Development.” University of Rochester Doctoral Thesis, (2004): 78-80.

[35] M. Christophersen, J. Carstensen, A. Feuerhake, H. Foll. “Crystal Orientation and Electrolyte Dependence for Macropore Nucleation and Stable Growth on p-Type Si.” Materials Science and Engineering, Vol. B69-70 (2000): 194-198.

[36] M. Christophersen, J. Carstensen, K. Voigt, H. Foll. “Organic and Aqueous Electrolytes used for Etching Macro- and Mesoporous Silicon.” Phys. Stat. Sol., Vol. a 197 No. 1 (2003): 34-38.

[37] C. Jager, B. Finkenberger, W. Jager, M. Christophersen, J. Carstensen, H. Foll. “Transmission Electron Microscopy Investigations of the Formation of Macropores in n- and p-Si(001)/(111).” Materials Science and Engineering, Vol. B69-70 (2000): 199-204.

[38] L. Canham. Properties of Porous Silicon. Emis data reviews series No. 18 London: INSPEC, 1997. 89-95.

[39] H. F. Okorn-Schmidt. "Characterization of Silicon Surface Preparation Processes for Advanced Gate Dielectrics." IBM J. Res. Develop., Vol. 43 No. 3 (1999):351-365.

[40] C. Cadet, D. Deresmes, D. Vuillaume, D. Stievenard. "Influence of Surface Defects on the Electrical Behavior of Aluminum-Porous Silicon Junctions." Applied Physics Letters, Vol. 57 (1990): 1046-1048.

[41] V. Lehmann, F. Hofmann, F. Moller, U. Gruning. "Resistivity of Porous Silicon:a Surface Effect." Thin Solid Films, Vol. 255 (1995): 20-22.

[42] L. A. Balagurov, D. G. Yarkin, E. A. Petrova. "Electronic Transport in Porous Silicon of Low Porocity Made on a p+ Substrate." Material Science Engineering, Vol. B69-70 (2000): 127-131.

[43] I. Schechter, M. Ben-Chorin , A. Kux. "Gas Sensing Properties of Porous Silicon." Analytical Chemistry, Vol. 67 (1995): 3727-3732.

[44] Rehm, G. L. McLendon, P. M. Fauchet. "Conduction and Valance Band Edges of Porous Silicon Determination by Electron Transfer." Journal of American Chemical Society, Vol. 118 (1996): 4490-4491.

[45] R. C. Andersen, R. S. Muller, C. W. Tobias. Journal of Electrochemistry Society, Vol. 138 (1991): 3406-3411.

[46] Pierce Biotechnology. "Material Safety Data Sheet." 3-Aminopropyltriethoxysilane. (2005): 1-7.

[47] Pierce Biotechnology. "Instructions." 3-Aminopropyltriethoxysilane. (2005): 1.

[48] Pierce Biotechnology. "Material Safety Data Sheet." EZ-Link Sulfo-NHS-LC-LC-Biotin. (2005): 1-6.

[49] Pierce Biotechnology. "Instructions." EZ-Link Sulfo-NHS-LC-LC-Biotin. (2005): 1-5.

[50] Pierce Biotechnology. "Material Safety Data Sheet." ImmunoPure Streptavidin. (2005): 1-5.

[51] Pierce Biotechnology. "Instructions." ImmunoPure Streptavidin. (2005): 1-2.

[52] Pierce Biotechnology. "Technical Resource." Attach a Protein onto Glass, Silica, or Quartz Surface using a Cleavable Cross-Linker. (2005): 1-3.

[53] V. Polishchuk, E. Souteyrand, J. R. Martin, V. I. Strikha, V. A. Skryshevesky. "A Study of Hydrogen Detection with Palladium Modified Porous Silicon." Analytica Chimica Acta., Vol. 375 (1998): 205-210.

[54] C. Tsamis, L. Tsoura, A. G. Nassiopoulou, A. Travlos, C. E. Salmas, K. S. Hatzilyberis, G. P. Androutsopoulos. "Hydrogen Catalytic Oxidation Reaction on Pd-Doped Porous Silicon." IEEE Sensors Journal, Vol. 2 No. 2 (2002): 89-95.

[55] J. A. Dickson, R. M. Goodman. "Integrated Chemical Sensors Based on Carbon Black and Polymer Films Using a Standard CMOS Process and Post Processing". IEEE proceedings ISCAS-2000 Geneva, Switzerland (2000): 341-344.

[56] F. Niklaus, P. Enoksson, E. Kalvesten, G. Stemme. "Low-Temperature Full Wafer Adhesive Bonding." J. Micromech. Microeng., Vol. 11 (2001): 100-107.

[57] J. D. Plummer, M. D. Deal, P. B. Griffin. Silicon VLSI Technology. (2000): 333-337.

[58] F. Zee, J. Judy. "MEMS Chemical Gas Sensor." IEEE University/Government/Industry Microelectronics Symposium, (1999): 150-152.

[59] C.B. O'Neal, A.P. Malshe, S.B. Singh, W.D. Brown, W.P. Eaton. "Challenges in the packaging of MEMS." Advanced Packaging Materials: Processes, Properties and Interfaces, (1999): 41-47.

[60] C. Lin, G. Lee, B. Chang, G. Chang. "A New Fabrication Process for Ultra-thick Microfluidic Microstructures Utilizing SU-8." J. Micromech. Microeng., Vol. 12 (2002): 590-597.

[61] S. Li, C. B. Freidhoff, R. M. Young, R. Ghodssi. "Fabrication of Micronozzles using Low-Temperature Wafer-Level Bonding with SU-8." J. Micromech. Microeng., Vol. 13 (2003): 732-738.

[62] MicroChem. NANO SU-8 2000: Negative Tone Photoresist Formations 2035-2100. (2005): 1-4.

# Appendix A

## Biotin – Stepavidin Protein Binding

Step 1: Aminosilane solution

2% aminosilane in acetone

Combine 1 part aminosilane in 50 parts acetone and shake.

Dispense 10 µl of aminosilane solution in channel and allow sensor to sit in covered pie plate with moist cloths for 10 min.

Rinse with aceone.

Bake sensor @ 100C for 10 minutes in oven (we used hairdryer)

This procedure attaches an amine group (NH3) to the oxide surface in the sensor. One could think of this as a priming step for the biotin or probe material.

Step 2: Biotin

Bring biotin to room temperature before opening.

Combine 1 mg of biotin in 1 ml of phosphate buffered saline (PBS).

Dilute this into 0.5 mg / ml, and 0.25 mg / ml solutions by adding more PBS.

There are now 1 mg/ml, 0.5 mg/ml, and 0.25 mg/ml concentrations.

Dispense desired solution into channel and allow sensor to sit in covered pie plate with moist cloths for 30 min.

Rinse sensors with potassium phosphate (PP) buffer by squirting channels several times.

Step 3: Streptavidin

Combine 2 mg of streptavidin in 1 ml of PP buffer.

Dispense solution into channel and allow sensor to sit in covered pie plate with moist cloths for 30 min.

# Appendix B

## Photolithography on Macroporous Silicon

- Mount substrate to 6” Si substrate with tape spacers in between. (This assumes flow-through structures are present on device substrate.)

- Static dispense of HMDS ramp to 2000 rpm for 45 sec.

- Static dispense of Clariant AZ 9260 liquid photoresist ramp to 2000 rpm for 45 sec.

- Bake at 110° C for 45 sec.

- Static dispense of Clariant AZ 9260 liquid photoresist ramp to 2000 rpm for 45 sec.

- Bake at 110° C for 45 sec.

- UV exposure dose of 2600 mJ/cm$^2$, 4 min 20 sec @ 10 mW/cm$^2$.

- Develop in Shipley MF-351 (sodium hydroxide) 1:4 by volume in DI water. Apply agitation by hand for approximately 4 min 20 sec.

# Appendix C

## Sensor Fabrication - Basic Isolation

1. CMP backside
2. RCA Clean
3. Grow 5000A wet oxide
4. Coat front side with photoresist
5. Wet etch backside oxide with HF
6. Strip resist
7. RCA clean
8. Spin on backside dopant
9. Oven cure
10. Drive in
11. Blanket wet etch oxide with HF
12. Grow 500A dry oxide
13. LPCVD 1500A nitride
14. Photo 1: Anodization
15. Etch nitride on front side with LAM
16. Clean backside with acetone
17. Blanket etch nitride on backside with LAM
18. Etch pad oxide off wafer with BOE
19. Strip resist
20. RCA clean
21. HF Dip
22. Sputter Al on back side
23. Sinter
24. Anodize
25. Strip Al in Al wet etch
26. Grow 1000A dry oxide
27. LPCVD 1500A nitride SMFL stoich.
28. Photo 2: KOH coat backside
29. Etch backside nitride with LAM
30. Paint resist on pores
31. Etch backside oxide in HF
32. Strip resist on front side and backside
33. KOH etch
34. Decontamination
35. Nitride deglaze in BOE
36. Nitride strip in hot phos.
37. Etch pad oxide off wafer with BOE
38. Oxidize pores with 1000A dry oxide
39. Photo 3: Contact Cut thick coat ************* maybe do step 40 first
40. Paint resist in channels ******** maybe do step 39 after this
41. Etch oxide with BOE
42. Strip resist
43. RCA clean
44. HF Dip
45. Sputter Al 2um
46. Photo 4: Metal Definition
47. Etch Al with Al wet etch
48. Strip resist
49. Sinter

# Appendix D

# Fluidic Integration and Fabrication

1. Clean glass slides
    a. Acetone, IPA, DI H2O
2. Photo 1: Fluidic channels on backside of fluidic slide
    a. Dehydration bake 200C for 5 min
        i. Flip slide at 2.5min
    b. Coat SU-8
        i. Static dispense
            1. Drizzle on and spreading like butter
        ii. Ramp to 500 rpm at 100 rpm/sec hold for 5-10 sec
        iii. Ramp to 1000 rpm at 300 rpm/sec and hold for 35 sec (260 um)
        iv. Wipe off edge bead with chemwipe
    c. Pre-bake and Softbake
        i. Place slide on stilted wafer
        ii. 5 min. ramp from 20 C to 65 C and hold for 7 min
        iii. 5 min. ramp from 65 C to 95 C and hold for 60 min
        iv. 33 min. ramp from 95 C to 55 C and hold for 5 min
        v. 60 min. ramp from 55 C to 30 C
        vi. Let sit for 5 min.
    d. Expose
        i. Use i-line filter for 700 mJ/cm2 exposure dose (5 min 50 sec at 2mW irradiance)
    e. Post exposure bake
        i. 5 minute ramp from 20 C to 65 C and hold for 1 min
        ii. 5 min. ramp from 65 C to 95 C and hold for 15 min
        iii. 33 min. ramp from 95 C to 55 C and hold for 5
        iv. 60 min. ramp from 55 C to 30 C
    f. Develop
        i. SU-8 solvent developer PM acetate
        ii. Submerge in developer and provide strong agitation for ~20 min
    g. Hard bake
        i. 200C for 10 min use stepped/ramped heating
        ii. Avoid rapid cooling
3. Drill holes into glass fluidic slide
4. Clean frontside
5. Coat SU-8 on frontside of fluidic slide
    a. Dehydration bake 200C for 5 min
    b. Coat SU-8
        i. Static dispense
        ii. Ramp to 500 rpm at 100 rpm/sec hold for 5-10 sec
        iii. Ramp to 2000 rpm at 300 rpm/sec and hold for 30 sec (140 um)
    c. Pre-bake and Softbake
        i. Ramp from 20 C to 65 C and hold for 5 min

        - ii. Ramp from 65 C to 95 C and hold for 35 min
        - iii. Ramp from 95 C to 55 C and hold for 5 min

6. Bond to device substrate
    - a. Bring substrates together while hot
    - b. Bake at 55 C for 5 min with applied pressure
    - c. Avoid rapid cooling
    - d. Flood expose
        - i. Use i-line filter for 700 mJ/cm2 exposure dose (5 min 50 sec at 2mW irradiance)
    - *e. Post exposure bake (???? Skip this step for now)*
        - *i. Ramp from 20 C to 65 C and hold for 1 min*
        - *ii. Ramp from 65 C to 95 C and hold for 20 min*
        - *iii. Avoid rapid cooling*
    - *f. Hard Bake???? (Skip for now)*
7. Drill holes into glass capping slide
8. Coat SU-8 on glass capping slide
    - a. Dehydration bake 200C for 5 min
    - b. Coat SU-8
        - i. Static dispense
        - ii. Ramp to 500 rpm at 100 rpm/sec hold for 5-10 sec
        - iii. Ramp to 2000 rpm at 300 rpm/sec and hold for 30 sec
    - c. Pre-bake and Softbake
        - i. Ramp from 20 C to 65 C and hold for 5 min
        - ii. Ramp from 65 C to 95 C and hold for 35 min
        - iii. Ramp from 95 C to 55 C and hold for 5 min
9. Bond to device substrates
    - a. Bring substrates together
    - b. Bake at 55 C for 5 min with applied pressure
    - c. Avoid rapid cooling
    - d. Flood expose
        - i. Use i-line filter for 700 mJ/cm2 exposure dose (5 min 50 sec at 2mW irradiance)
    - e. Post exposure bake and hard bake
        - i. Ramp from 20 C to 65 C and hold for 1 min
        - ii. Ramp from 65 C to 95 C and hold for 20 min
        - iii. Avoid rapid cooling
    - f. Hard Bake????
        - i. Ramp from 95 C to 200C and hold for 10 min.
        - ii. Avoid rapid cooling